

HIGH RESOLUTION WIND RETRIEVAL FOR SEAWINDS ON
QUIKSCAT

by

Jeremy B. Luke

A thesis submitted to the faculty of

Brigham Young University

in partial fulfillment of the requirements for the degree of

Master of Science

Department of Electrical and Computer Engineering

Brigham Young University

August 2003

Copyright © 2003 Jeremy B. Luke

All Rights Reserved

BRIGHAM YOUNG UNIVERSITY

GRADUATE COMMITTEE APPROVAL

of a thesis submitted by

Jeremy B. Luke

This thesis has been read by each member of the following graduate committee and by majority vote has been found to be satisfactory.

Date

Dr. David G. Long, Chair

Date

Dr. Travis E. Oliphant

Date

Dr. Karl F. Warnick

BRIGHAM YOUNG UNIVERSITY

As chair of the candidate's graduate committee, I have read the thesis of Jeremy B. Luke in its final form and have found that (1) its format, citations, and bibliographical style are consistent and acceptable and fulfill university and department style requirements; (2) its illustrative materials including figures, tables, and charts are in place; and (3) the final manuscript is satisfactory to the graduate committee and is ready for submission to the university library.

Date

Dr. David G. Long
Chair, Graduate Committee

Accepted for the Department

Dr. A. Lee Swindlehurst
Graduate Coordinator

Accepted for the College

Dr. Douglas M. Chabries
Dean, College of Engineering and Technology

ABSTRACT

HIGH RESOLUTION WIND RETRIEVAL FOR SEAWINDS ON QUIKSCAT

Jeremy B. Luke

Department of Electrical and Computer Engineering

Master of Science

An algorithm has been developed that enables improved the resolution wind estimates from SeaWinds data. This thesis presents the development of three key portions of the high resolution wind retrieval algorithm: Compositing individual σ^0 measurements and K_p , Retrieved wind bias correction, and ambiguity selection for high resolution winds. The high resolution winds produced by this algorithm are expected to become a useful resource for scientists and engineers studying the ocean winds. The high resolution wind retrieval algorithm allows wind to be retrieved much closer to land than is available from the low resolution winds estimated from the same scatterometer by the Jet Propulsion Laboratory. The high resolution winds allow features such as the eye of hurricanes to be seen with much greater detail than was previously possible.

ACKNOWLEDGMENTS

I would like to thank my thesis advisor, Dr. David Long, for his help and inspiration in the development and writing of this thesis. He has been more than just a thesis advisor, he has been an example and a friend. His advice for not only school and work but also for life, will last a Long-time.

I would also like to thank my wife Hillary. The patience and support she has shown me during this time in our lives has helped me more than she will ever know. She has sacrificed her free time to stay home and take care of our two sons so that I could finish this thesis. I would also like to thank her along with our sons, Hunter and Joseph, for bringing balance to my life. Going home to them is always the best part of the day. I dedicate this work to them.

Contents

Acknowledgments	xi
List of Tables	xvii
List of Figures	xxiv
1 Introduction	1
1.1 Background	1
1.2 Wind Retrieval	2
1.3 Summary of Contributions	3
2 Scatterometry Background	5
2.1 Scatterometry	5
2.2 Seawinds Scatterometer	11
2.2.1 SeaWinds Data Files	15
2.3 High Resolution Wind Retrieval	16
3 Compositing Slice K_p Coefficients	21
3.1 Introduction	21
3.2 K_p	21
3.3 K_p for Slices	22
3.4 Compositing Slice K_p	23
3.4.1 Compositing σ^0	24
3.4.2 Compositing K_p	24
3.4.3 Compositing K_p equation coefficients	26
3.5 Comparison With Empirically Calculated K_p	28

3.6	Conclusion	29
4	Increased Accuracy in Retrieved High Resolution Winds Through Bias Correction	33
4.1	Introduction	33
4.2	Low Resolution Bias	34
4.2.1	Wind bias binned by true wind speed and direction	36
4.2.2	Wind bias binned by retrieved wind speed and direction	41
4.3	High Resolution Bias	46
4.4	Wind Bias Table	50
4.5	Conclusion	52
5	High Resolution Ambiguity Removal	55
5.1	Introduction	55
5.2	Initialization of the Ambiguity Selection Algorithm	55
5.3	Ambiguity Selection Method Used in Low Resolution Winds	56
5.4	Median filter ambiguity selection for high resolution winds	59
5.4.1	Median Filter	59
5.4.2	Application of median filter to ambiguity selection	60
5.5	Results of median filter	61
5.6	Comparison of Low Resolution and High Resolution Wind Distribution	66
5.7	Conclusion	72
6	Conclusion	75
6.1	Summary of Contributions	75
6.1.1	Kp Compositing Methods	76
6.1.2	Bias Removal Tables	76
6.1.3	Ambiguity Selection	76
6.1.4	Future Research	77
A	Code Performance Comparisons	79
A.1	Introduction	79

A.2	L1B Data Product	79
A.3	L2A Data Product	80
A.4	Wind Retrieval Program	81
A.5	Results	82
	A.5.1 L1B data	83
	A.5.2 L2A data	88
A.6	Conclusion	93
B	σ_0 Over Land	95
B.1	Introduction	95
B.2	Combining Slices, (Compositing)	95
B.3	Regional Statistics	97
B.4	Comparing Eggs and Slices	97
B.5	Kp Prediction	98
B.6	Empirical Kp calculation	99
B.7	Conclusion	100
	Bibliography	104

List of Tables

A.1	Wind Speed, Direction and MLE for rev 12950 row 314 wvc 18. L1B wind estimates calculated using α' , β' , and γ' unmodified.	83
A.2	The L2A α' , β' , and γ' are extracted directly from the L2A data file. The L1B α' , β' , and γ' are calculated using data from the L1B file and equations (4), (5), and (6). The data is extracted from rev 12950 row 314 WVC 18. χ is the azimuth angle of the pulse. θ is the incidence angle of the pulse.	85
A.3	Wind Speed, Direction and MLE for rev 12950 row 314 wvc 18. L1B wind estimates calculated using α , β , and γ	86
A.4	Wind Speed, Direction and MLE for rev 12950 row 314 wvc 18. Wind estimates calculated using L1B data to calculate α' , β' , and γ' . K_{pr} is read in from a table.	87
A.5	Wind Speed, Direction and MLE for rev 12950 row 314 wvc 18. Wind estimates calculated using L1B data to calculate α , β , and γ . K_{pr} is read in from a table.	88
A.6	Wind Speed, Direction and MLE for rev 12950 row 314 wvc 18. Wind estimates calculated using α' , β' , and γ' directly, extracted from the L2A file	89
A.7	Wind Speed, Direction and MLE for rev 12950 row 314 wvc 18. Wind estimates calculated using α , β , and γ	90
A.8	Wind Speed, Direction and MLE for rev 12950 row 314 wvc 18. Wind estimates calculated using α' , β' , and γ' as in equations (9), (10), and (11). K_{pr} is read in from a table.	91
A.9	Wind Speed, Direction and MLE for rev 12950 row 314 wvc 18. Wind estimates calculated using α , β , and γ which were calculated by first applying equations (9), (10), and (11) and then equations (8), (5), and (6). K_{pr} is read in from a table.	92
A.10	Mean error	93
B.1	Particular measured values for one random pulse	97

List of Figures

2.1	Geophysical Model Function relating a range of speeds to σ^0 . The relative azimuth angle used is 0° . The model function used is the “Wentz” model function. The 46° incidence angle uses horizontal polarization and the 54° uses vertical polarization	7
2.2	Geophysical model function relating relative azimuth angle to σ^0 . Wind speeds of 5 m/s, 10 m/s, and 20 m/s with an incidence angle of 46° were used to generate this plot from the “Wentz” model function. . .	8
2.3	Geophysical model function relating relative azimuth angle to σ^0 . Wind speeds of 5 m/s, 10 m/s, and 20 m/s with an incidence angle of 54° were used to generate this plot from the “Wentz” model function. . .	9
2.4	Geophysical model function relating values of σ^0 to possible wind speed and direction solutions. The solid line in plots (a) through (d) represents possible solutions from one σ^0 measurement taken at 350° azimuth and 54° incidence (V-pol). The dashed line in plots (b) through (d) represents solutions from one σ^0 measurement taken at 190° azimuth and 54° incidence (V-pol). The dotted line in plots (c) and (d) represents solutions for one σ^0 measurement taken at 345° azimuth and 46° incidence (H-pol). The dash-dot line in plot (d) represents solutions for one σ^0 measurement taken at 195° azimuth and 46° incidence (H-pol).	10
2.5	Contour plot of the σ^0 measurement response for (a) eggs and (b) slices. The contour interval is 3dB. Shown in (b) are twelve slices however data received from JPL contains information on the inner eight slices. Image courtesy of Dr. David Long	12
2.6	QuikSCAT satellite	13

2.7	The average number of σ^0 measurements in each wind vector cell. (a) Forward looking outer beam, (b) forward looking inner beam, (c) aft looking inner beam, and (d) aft looking outer beam.	14
2.8	Illustration showing overlap in slice measurements due to the pulse repetition frequency of the SeaWinds instrument and size slice footprint. Image courtesy of Dr. David Long	17
2.9	Illustration showing overlap in slice measurements due to the pulse repetition frequency and antenna spin rate. Image courtesy of Dr. David Long	17
3.1	Egg A coefficient and composited slice A coefficient.	27
3.2	(a) Regions of homogeneous backscatter used in study. (b) SIR images showing backscatter. (quev-a-Ama01-257-260.sir)	29
3.3	K_p values for both regions in Figure 3.2. The empirical K_p is found using Eq. 3.1. The Mean Egg K_p value is the mean value of the egg measurement predicted K_p calculated using the method outlined in section 3.2. Method 1 refers to the mean value of K_p calculated from the slice K_p using Eq. 3.25. Method 2 refers to the mean value of K_p calculated from the slice K_p using method outline in section 3.4.3. The number of measurements for each region and beam are: Region 1 inner beam 25,024, outer beam 23,166, Region 2 inner beam 12,320, and outer beam 12,765	30
3.4	Summary of K_p compositing methods	31
4.1	Mean wind speed error binned by true wind speed and direction, Figures (a) and (b) are plots of the mean speed error in each bin. Figures (c) and (d) are plots of the mean speed error after bias correction. . .	37
4.2	RMS wind speed error binned by true wind speed and direction. Figures (a) and (b) are plots of the RMS speed error in each bin. Figures (c) and (d) are plots of the RMS speed error after bias correction. . .	38
4.3	Mean wind direction error binned by true wind speed and direction. Figures (a) and (b) are plots of the mean wind direction error in each bin. Figures (c) and (d) are plots of the mean wind direction error in each bin after bias correction.	39

4.4	RMS wind direction error binned by true wind speed and direction. Figures (a) and (b) are plots of the RMS wind direction error in each bin. Figures (c) and (d) are plots of the RMS wind direction error in each bin after bias correction.	40
4.5	Mean wind speed error binned by simulated wind speed and direction, Figures (a) and (b) are plots of the mean speed error in each bin. Figures (c) and (d) are plots of the mean speed error after bias correction.	42
4.6	RMS wind speed error binned by simulated wind speed and direction. Figures (a) and (b) are plots of the RMS speed error in each bin. Figures (c) and (d) are plots of the RMS speed error after bias correction.	43
4.7	Mean wind direction error binned by simulated wind speed and direction. Figures (a) and (b) are plots of the mean wind direction error in each bin. Figures (c) and (d) are plots of the mean wind direction error in each bin after bias correction.	44
4.8	RMS wind direction error binned by simulated wind speed and direction. Figures (a) and (b) are plots of the RMS wind direction error in each bin. Figures (c) and (d) are plots of the RMS wind direction error in each bin after bias correction.	45
4.9	Mean and RMS errors in wind speed and direction verses high resolution wind vector cell. Data was obtained using true wind speeds shown and true wind direction of 273°	47
4.10	(a) Mean wind speed error binned by wind speed and wind direction. (b) Mean wind speed error after bias adjustment binned by wind speed and direction. (c) Mean wind direction error binned by wind speed and direction. (d) Mean wind direction error after bias adjustment binned by wind speed and direction. Wind speed bins are 0.5 m/s wide. Wind direction bins are 2° wide.	49
4.11	(a) Standard error of the mean for each bin in the wind speed bias table (WVC 200). (b) Standard error of the mean for each bin in the wind direction bias table (WVC 200).	50

4.12	Sampled data fitted with cubic spline.	52
5.1	Illustration showing the sizes of windows used in testing median filter for use in ambiguity selection	60
5.2	Low resolution (a) wind speed and (b) direction in study area.(c) Down-sampled low resolution wind field to show wind flow with ar- rows, background color represents the wind speed.	63
5.3	High resolution (a) wind speed and (b) wind direction in study area. Wind ambiguity selection is performed by choosing the ambiguity clos- est to the low resolution wind vector in Figure 5.2	64
5.4	High resolution (a) wind speed and (b) wind direction after ambiguity selection with 3x3 median filter is performed	64
5.5	High resolution (a) wind speed and (b) wind direction after ambiguity selection with 5x5 median filter is performed	65
5.6	High resolution (a) wind speed and (b) wind direction after ambiguity selection with 7x7 median filter is performed	65
5.7	High resolution (a) wind speed and (b) wind direction after ambiguity selection with 11x11 median filter is performed.	66
5.8	(a) Illustration of small region selected to show results of median fil- ter. (b) Low resolution winds in selected region. The region selected includes half of the left low resolution wind cell and half of the right low resolution wind cell, both wind cells are therefore included in the plot. (c) High resolution wind before median filtering is done. The am- biguities selected here are the closest in direction to the low resolution wind vectors shown in (b).	67
5.9	Results of 4 sizes of median filter in high resolution ambiguity removal algorithm. (a) 3x3 (b) 5x5 (c) 7x7 (d) 11x11	68
5.10	Illustration Showing region selected.	69

5.11	Illustration showing high resolution selected ambiguity in region. (a) Selected ambiguities shown with background color representing the wind speed. (b) Selected ambiguities shown with background color representing wind direction.	69
5.12	Illustration of the four ambiguities at each pixel in the selected region. The background color in each image corresponds to the wind direction. (a) The first ambiguities for each pixel. (b) The second ambiguities for each pixel. (c) The third ambiguities for each pixel. (d) The fourth ambiguities for each pixel.	70
5.13	Distribution of (a) wind speeds and (b) wind directions in region illustrated in Fig. 5.6.	71
5.14	Low resolution wind vs high resolution wind in wind field.	71
A.1	Wind estimates calculated using L1B data to calculate α' , β' , and γ' in the Science wind retrieval code, for rev 12950 row 314 wvc 18. See Table A.1	83
A.2	Wind estimates reported in the L2B data file for rev 12950 row 314 WVC 18. See Table A.1	83
A.3	Wind estimate error averaged over row 311 through 321 of rev 12950 for all wind vector cells. The wind estimates were calculated using α' , β' , and γ' from L1B data.	84
A.4	Wind estimate error averaged over row 311 through 321 for all wind vector cells. The wind estimates were calculated using α , β , and γ from L1B data.	86
A.5	Wind estimate error averaged over row 311 through 321 for all wind vector cells. The wind estimates were calculated using α' , β' , and γ' from L1B data with K_{pr} read in from table.	87
A.6	Wind estimate error averaged over row 311 through 321 for all wind vector cells. The wind estimates were calculated using α , β , and γ from L1B data with K_{pr} read in from table.	88
A.7	Wind estimate error averaged over row 311 through 321 for all wind vector cells. The wind estimates were calculated using α' , β' , and γ' from the L2A file	89

A.8	Wind estimate error averaged over row 311 through 321 for all wind vector cells. The wind estimates were calculated using α , β , and γ calculated using equations (4), (5), and (6) with data from the L2A file	90
A.9	Wind estimate error averaged over row 311 through 321 for all wind vector cells. The wind estimates were calculated using α' , β' , and γ' from the L2A file. K_{pr} is read in from table and included as in equations (9), (10), and (11).	91
A.10	Wind estimate error averaged over row 311 through 321 for all wind vector cells. The wind estimates were calculated using α , β , and γ calculated using equations (4), (5), and (6) with data from the L2A file. K_{pr} is read in from table and included as in equations (9), (10), and (11).	93
B.1	Study region locations mapped over QSCAT image qusv-a-NAf00-037-040.sir. Each region is defined by latitude and longitude coordinates.	96
B.2	Number of pulses that hit each region. Left bar is inner beam, right bar is outer beam	98
B.3	Mean σ_0 value in each region	99
B.4	Difference in mean σ_0 between linear averaged and weighted average composite slices. Top graph is difference in linear space. Bottom is difference in dB	100
B.5	Mean Kp value for eggs	101
B.6	Mean Kp for slices	101

Chapter 1

Introduction

1.1 Background

The study of the Earth's climate is an important field of science. Many people's everyday lives around the world are influenced by the current and predicted weather. Before the age of satellites this knowledge was limited to the current weather conditions on land and at isolated weather stations. Accurately predicting the weather can save millions of dollars by allowing people to prepare for large storms and droughts. A large factor in the Earth's weather and climate is the near-surface winds over the ocean. A knowledge of how the air and sea interact and how this influences ocean circulation is invaluable in predicting changes in the weather. Scatterometers give scientists a method to measure this near-surface wind over the ocean. Scatterometers are able to measure the ocean winds in all weather conditions and in both daylight and at night. The latest scatterometer is capable of covering 90% of the Earth's surface in one day.

Scatterometry is the method of measuring the reflection of space-borne radar from the earth surface. The concept of using radar to measure the winds over the ocean came from noise known as sea clutter noticed by radar-system operators during World War II.

The first scatterometer was part of the Skylab missions in 1973 and 1974. Then in 1978 a scatterometer (SASS) was flown on the Seasat-A satellite. Data from this mission proved that wind velocity measurements could accurately be made from space. Scatterometers have also flown from 1992 to 2001 on the European Space

Agency’s Remote Sensing Satellites (ERS-1 and ERS-2). The NASA Scatterometer (NSCAT) was launched in 1996 and returned an unprecedented quality of data until a power failure in June of 1997 ended the mission. The QuikSCAT satellite carrying the SeaWinds instrument was launched as a “quick recovery” mission on June 19, 1999 [1].

1.2 Wind Retrieval

Scatterometers transmit pulses of microwave energy to the ocean surface and measure the power in the returned echo. From this measurement an estimate of the normalized radar cross section (σ^0) of the sea surface can be obtained. Near-surface wind over the ocean affects the roughness of the ocean surface, which changes the radar cross section of the ocean, which in turn affects the magnitude of the backscattered power [2].

To estimate the wind velocity over the ocean from σ^0 one must know the relationship between σ^0 and the near-surface wind velocity. Due to the inability of scientists to derive a theory-based model function relating these two parameters an empirical model function, known as the Geophysical Model Function (GMF), has been developed to relate the radar cross section to the near-surface wind. The GMF can be written as [2]

$$\sigma^0 = f(|U|, \chi, \dots; \theta, f, pol) \tag{1.1}$$

where $|U|$ is the wind speed, χ is the azimuth angle between the wind direction and the incident radiation (see Fig. 2.6), \dots represent variables other than wind which have an affect on σ^0 such as long waves, stratification, and temperature, θ is the incident angle of the radiation (see Fig. 2.6), f is the frequency, and pol is the polarization of the incident radiation.

To estimate the wind speed and direction of the wind which produced a given σ^0 involves inverting the Geophysical Model Function. The process of retrieving winds from σ^0 is described in more detail in the next chapter.

Through resolution enhancement algorithms developed for σ^0 it is now possible to increase the resolution of the wind fields estimated from scatterometer σ^0 . This thesis develops several key methods used in a new high resolution wind retrieval algorithm, from pre-processing of parameters used in the wind retrieval algorithm, to bias adjustments done during the processing of the winds, to a final post-processing step to select the correct ambiguity.

1.3 Summary of Contributions

This thesis makes three contributions to the process of high resolution wind retrieval using the Seawinds instrument on the QuikSCAT satellite. These contributions are summarized in the next three paragraphs.

High resolution wind retrieval uses higher resolution radar backscatter, σ^0 , measurements to retrieve the wind over the ocean. These higher resolution σ^0 measurements are range and Doppler resolved measurements known as “slices”. The lower resolution σ^0 measurements are known as “eggs”. The high resolution wind retrieval algorithm averages all of the slice measurements from a given beam that are contained in a given wind retrieval cell. This thesis analyzes methods to average or composite the σ^0 measurements. Along with this, methods for compositing the normalized standard deviation, K_p , and its parameters are derived.

Simulations have shown that a bias is introduced into the retrieved high resolution winds. This bias is a function of the measurement geometry, i.e. azimuth and incidence angles of the σ^0 measurements. A 3-dimensional table is compiled containing this bias. This table is used in the processing of the high resolution winds to adjust the retrieved winds by the correct bias. This thesis illustrates the development and the simulation results of the bias removal.

The final contribution of this thesis is the development of an ambiguity removal algorithm for the high resolution winds. The inversion of the Geophysical Model Function, previously discussed, produces several possible solutions. The wind retrieval algorithm limits the number of possible solutions to the best four. It is then left to post-processing to choose the best possible and most likely solution from these

possible solutions. The possible solutions are known as ambiguities. Due to the increased noise in the high resolution winds some ambiguity removal algorithms do not work. The most efficient method to choose the best ambiguity is to choose the one closest to the chosen ambiguity in the low resolution winds as an initialization and then perform post processing such as median filtering to clean up bad initial choices. Various methods for this post processing are examined in the final section of this thesis.

Chapter 2

Scatterometry Background

2.1 Scatterometry

The use of scatterometers to measure ocean winds has several advantages when compared to conventional techniques. Scatterometers can achieve near global coverage of the Earth's oceans every day. Conventional methods such as weather stations on ships and buoys are sparse and often inaccurate. Wind measurements taken from ships are often inaccurate due to badly placed anemometers, untrained observers, and errors introduced by the motion of the ship. They are also biased because ships avoid bad weather locations. Measurements from buoys are more accurate but are sparse and generally close to land.

Scatterometers do not measure the wind velocity over the ocean directly. Rather they use a highly indirect approach to estimate the wind velocity from the amount of power that is reflected back when the ocean is illuminated with a pulse of microwave energy. From this power measurement the normalized radar cross section can be estimated. The normalized radar cross section is known as σ^0 . It is a function of the amount of energy reflected by the scatterer and the gain of the scatterer in the direction of the receiver. The velocity of the wind over the ocean affects the roughness of the ocean surface. This roughness affects the σ^0 of the ocean surface. To obtain a wind velocity estimate the relationship between σ^0 and the wind (GMF) must be known.

To estimate the normalized radar cross section σ^0 from the reflected power measurement the radar equation is used [3]. The amount of backscattered power

received at the antenna from the reflection off the surface is a function of the radar cross section of the surface, i.e.

$$P_s = \frac{P_t G^2 \lambda^2 A_{rs}}{(4\pi)^3 R^4} \sigma^0 \quad (2.1)$$

where P_t is the transmitted power, G is the gain of the antenna, λ is the wave length of the transmitted power, R is the slant range from the antenna to the scatterer, and A_{rs} is the effective area of the scatterer. The total power measured at the receive antenna is the power from the backscattered signal P_s plus the noise power P_n . The noise power results from instrument noise and natural emissions of power from the atmosphere at the frequency being measured by the scatterometer. To estimate σ^0 this noise power must be subtracted from the total power, P_{s+n} , to give P_s . The normalized radar cross section, σ^0 , can then be used to estimate the wind velocity over the corresponding section of ocean.

As mentioned in the introduction, the relationship between the near-surface wind and the normalized radar cross section σ^0 is an empirically-derived model known as the geophysical model function (GMF). This empirical model function was developed using several million calibrated σ^0 measurements from the Seasat scatterometer along with several thousand high quality *in situ* measurements by Wentz and co-workers [4],[5].

The Seawinds scatterometer has two approximately constant incidence angles as explained in Section 2.2. One at 46° and one at 54° . From Figure 2.1 it can be seen that σ^0 increases approximately linearly with the log of the wind speed for a given azimuth angle. It is therefore straight forward to estimate the wind speed from σ^0 . Wind speed can be estimated with only a single measurement of σ^0 .

Estimating wind direction is not as straight forward. Figures 2.2 and 2.3 show that the relationship between σ^0 and the relative wind direction χ is nearly $\cos(2\chi)$ where σ^0 is at a maximum when $\chi = 0$, corresponding to upwind, and $\chi = 180$, corresponding to downwind. The maximum at 180° is slightly lower than the maximum at 0° . This asymmetry in upwind and down wind directions is beneficial. If not for this asymmetry it would be impossible to decipher between upwind and down

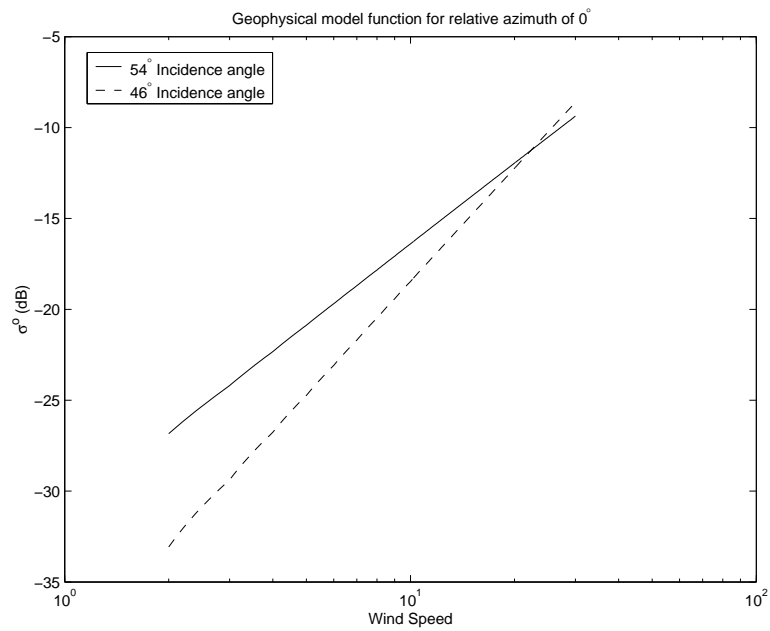


Figure 2.1: Geophysical Model Function relating a range of speeds to σ^0 . The relative azimuth angle used is 0° . The model function used is the “Wentz” model function. The 46° incidence angle uses horizontal polarization and the 54° uses vertical polarization

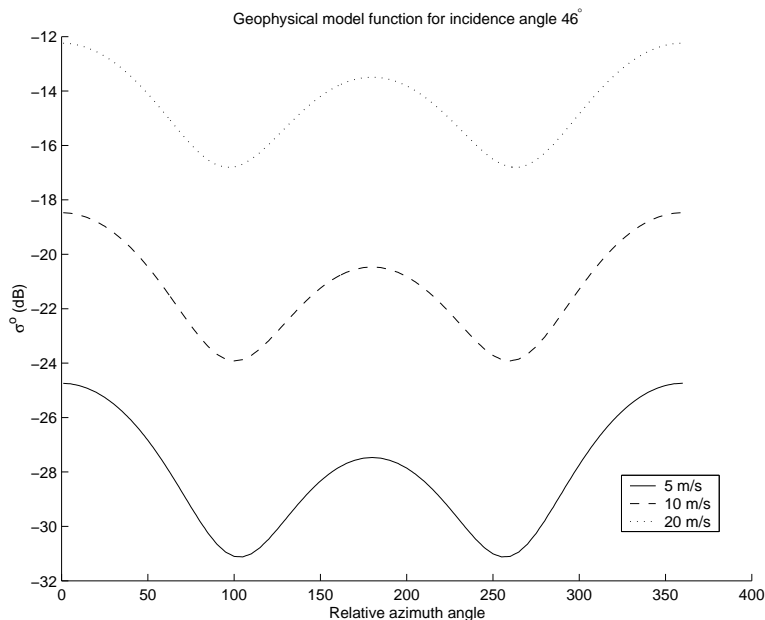


Figure 2.2: Geophysical model function relating relative azimuth angle to σ^0 . Wind speeds of 5 m/s, 10 m/s, and 20 m/s with an incidence angle of 46° were used to generate this plot from the “Wentz” model function.

wind directions giving two possible solutions that are 180° apart. It can also be seen that this asymmetry in the upwind and downwind directions, as well as the amplitude of the modulation in σ^0 due to relative azimuth angle, decreases with increasing wind speed. The upwind-downwind asymmetry is greater for horizontal polarization than it is for vertical polarization. It also increases with increasing incidence angle.

From Figures 2.2 and 2.3 it can be seen that it is not possible to resolve the wind direction given a single σ^0 measurement. Given that the wind speed can be found from one measurement there are two to four solutions for the wind speed. These possible solutions are referred to as ambiguities. To limit the number of ambiguities it is necessary to make measurements of σ^0 from several different azimuth angle and/or different polarizations. This concept is illustrated in Figure 2.4.

Figure 2.4(a) shows a plot of all possible wind speed and wind direction solutions for a given σ^0 measurement taken from an azimuth angle of 350° and an incidence angle of 54° using a vertically polarized beam. This plot shows that it is

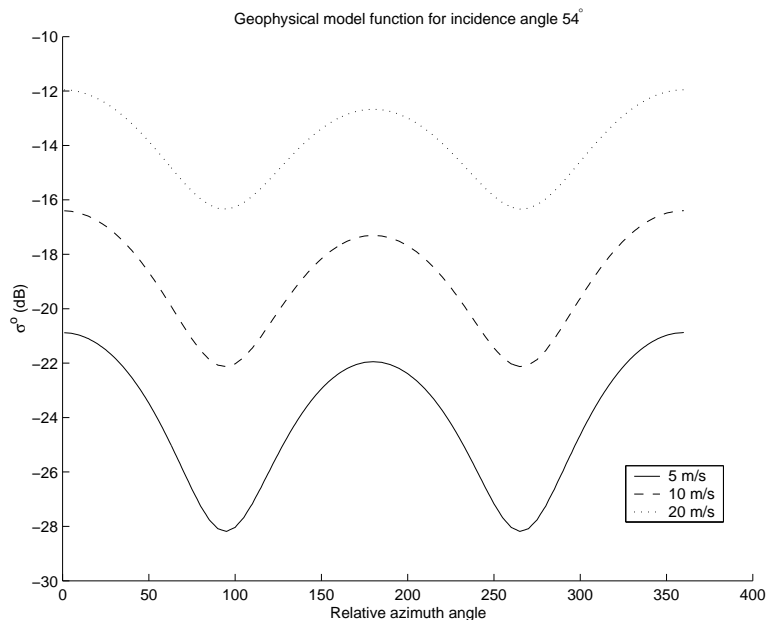


Figure 2.3: Geophysical model function relating relative azimuth angle to σ^0 . Wind speeds of 5 m/s, 10 m/s, and 20 m/s with an incidence angle of 54° were used to generate this plot from the “Wentz” model function.

not possible to obtain a single wind vector solutions from one σ^0 measurement. Figure 2.4(b) contains not only the plot of solutions given by σ^0 from plot (a) but also contains a plot of the solutions for a σ^0 measurement taken from an azimuth of 190° and an incidence angle of 54° using a vertically polarized beam. There are four intersections of the two curves. These intersections correspond to wind vector solutions given the two σ^0 measurements. As explained before these solutions are referred to as ambiguities. In Figure 2.4(c) another curve is added to the plot. The dashed curve is all the wind vector solutions that are possible for a given σ^0 measurement taken from an azimuth of 345° and an incidence angle of 46° using a horizontally polarized beam. The addition of this measurement limits the number of intersections to one. Also labeled on the plot is a point of near intersection. It is possible with only three measurements to get more than one intersection. With the addition of another σ^0 measurement, shown in Figure 2.4(d), there is only one location where all four curve intersect yielding a unique wind vector solution.

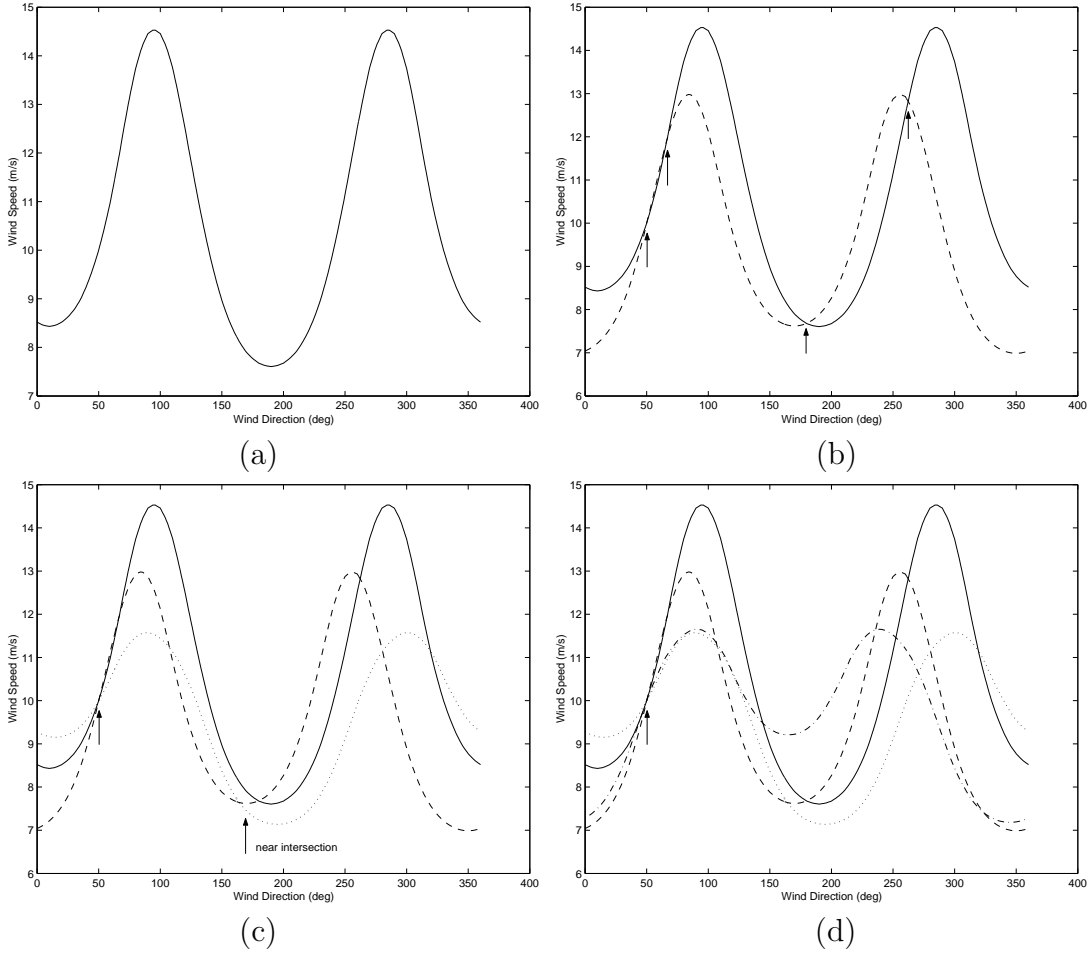


Figure 2.4: Geophysical model function relating values of σ^0 to possible wind speed and direction solutions. The solid line in plots (a) through (d) represents possible solutions from one σ^0 measurement taken at 350° azimuth and 54° incidence (V-pol). The dashed line in plots (b) through (d) represents solutions from one σ^0 measurement taken at 190° azimuth and 54° incidence (V-pol). The dotted line in plots (c) and (d) represents solutions for one σ^0 measurement taken at 345° azimuth and 46° incidence (H-pol). The dash-dot line in plot (d) represents solutions for one σ^0 measurement taken at 195° azimuth and 46° incidence (H-pol).

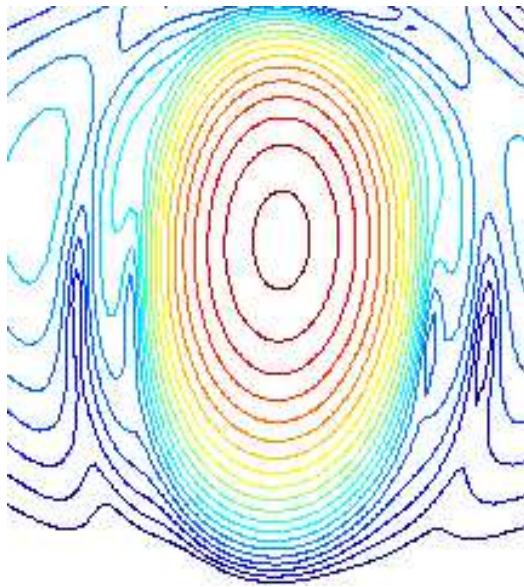
In practice instrumental noise, geophysical noise and the small upwind-downwind asymmetry of the geophysical model function cause the inversion of the model function to yield multiple solutions. These multiple solutions are a result of the near intersections of all four curves being mistaken for one true intersection due to the noise. There are several methods to choose a unique ambiguity. One of which is addressed in this thesis.

2.2 Seawinds Scatterometer

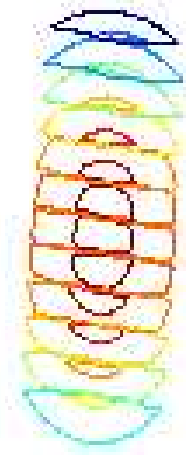
The Seawinds Scatterometer instrument flown on the QuikSCAT satellite was launched on June 19, 1999 into a sun-synchronous, circular orbit at an altitude of 803 kilometers. The Seawinds instrument departs from the fan beam-type antennas used on previous scatterometer missions. Seawinds uses a rotating one meter parabolic antenna with two spot beams that sweep in a circular pattern. The antenna rotates at a rate of 18 RPM. The two spot beams are offset providing two pencil-beam footprints at incidence angles of 46° and 54° for H-pol and V-pol respectively. The frequency of the microwave energy radiated from the antenna is 13.4 GHz. The pulse repetition frequency is nominally 187.5 Hz. The antenna rotation rate, the pulse repetition frequency and the velocity of the spacecraft are exploited in the high resolution wind retrieval. These factors allow for oversampling of the Earth's surface.

The antenna footprint on the ground is an ellipse with principal axes of 37 kilometers corresponding to the look direction and 25 kilometers corresponding to the azimuth direction. To provide higher range resolution the transmit pulse is modulated using a linear FM chirp. Signal processing then provides a sub-footprint range resolution of nominally 6 kilometers. These sub-footprint range resolved measurements are referred to as "slices". The entire footprint is referred to as an "egg".

The σ^0 measurement responses are shown in Fig. 2.5. The area of the "egg" footprint on the ground corresponds to the area contained within the second contour of Figure 2.5(a). This contour is the 6 dB contour. The individual "slice" footprints are shown in Figure 2.5(b). The area of each slice is the area within the 6 dB contour of each slice.



(a)



(b)

Figure 2.5: Contour plot of the σ^0 measurement response for (a) eggs and (b) slices. The contour interval is 3dB. Shown in (b) are twelve slices however data received from JPL contains information on the inner eight slices. Image courtesy of Dr. David Long

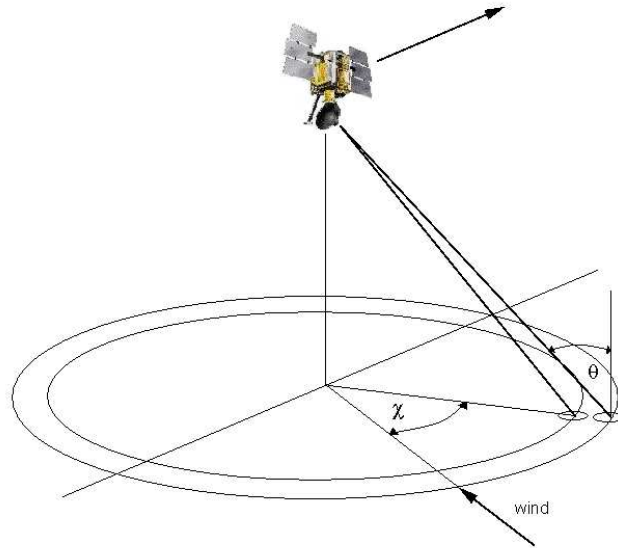


Figure 2.6: QuikSCAT satellite

SeaWiFS has a swath that is 1,800 kilometers wide for the outer beam and 1,400 kilometers wide for the inner beam, allowing it to cover 90% of the Earth's surface everyday.

The geometry of the SeaWiFS scatterometer is highly effective for wind retrieval. As explained in the previous section several measurements from unique look angles and/or polarizations are needed to uniquely solve the inverse geophysical model function. For most of the swath SeaWiFS is able to make four unique measurements: one forward looking, horizontally polarized, one forward looking, vertically polarized, one aft looking, horizontally polarized, and one aft looking vertically polarized. There are parts of the swath where this geometry breaks down. For example, in the far swath there are only outer beam (V-pol) measurements at fairly close azimuth angles, and at the center swath only two unique azimuth angles are available. The poor sampling geometry at these locations is evident in images of the wind fields. Figure 5.3(b)

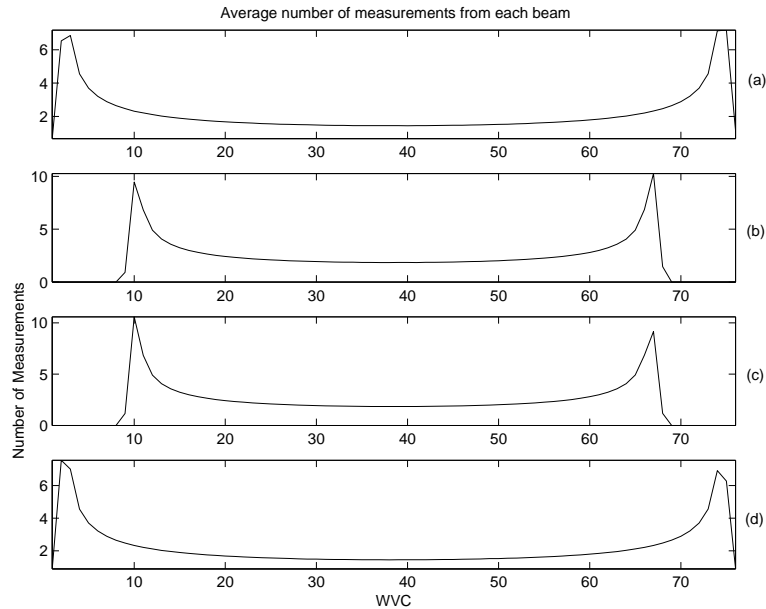


Figure 2.7: The average number of σ^0 measurements in each wind vector cell. (a) Forward looking outer beam, (b) forward looking inner beam, (c) aft looking inner beam, and (d) aft looking outer beam.

illustrates a high resolution wind field. In the nadir section of the swath the wind direction measurements are noisy. This is also the case for the low resolution wind field at this location in the swath.

The wind resolution cell using the egg measurements is a 25 km by 25 km square. This allows the swath of one revolution to be divided up into 76 cells, referred to as wind vector cells (WVC), in the cross track direction and 1,624 wind vector cells in the along track direction. The σ^0 measurements from the footprints that have centers which fall in the WVC are then used in the wind retrieval process.

Generally several footprint centers fall into one WVC. This number is dependent on cross track position of the WVC. Figure 2.7 shows the average number of σ^0 measurements in each cell for each beam. The beams are numbered as follows: beam (1) is the outer beam looking in the forward direction, beam (2) is the inner beam looking forward, beam (3) is the inner beam looking in the aft direction, and beam (4) is the outer beam looking in the aft direction. The total number of measurements

used to retrieve the wind in each wind vector cell is the sum of the number of each beam.

Recall that the size of the footprint is approximately 25 kilometers by 37 kilometers. In the range dimension the footprint size is larger than the WVC. It should be noted that, even though the center location of the footprint falls in the WVC, the radar cross-section σ^0 is estimated from power reflected by area outside and inside the WVC. Thus the effective resolution is actually coarser than the WVC size. When any WVC has a σ^0 measurement from a footprint that includes land or ice the WVC is not used to retrieve winds.

Due to the size of the footprint, the rotation rate and the pulse repetition frequency there is overlap in consecutive measurements. This fact makes the SeaWinds instrument a prime candidate for resolution enhancement algorithms.

2.2.1 SeaWinds Data Files

Three processing levels of the SeaWinds data are used in this thesis. The first two, L1B and L2A, contain the σ^0 measurement data while the third, L2B, contains the wind vector measurements estimated from the σ^0 measurements.

The L1B product contains the σ^0 values for both the slice and egg measurements. These measurements are time ordered, i.e. are listed in the order the measurements were made. They are arranged in telemetry frames of 100 pulses. The L1B product also contains information about the location of the measurement (latitude and longitude coordinates), geometry from which the measurement was taken (incidence and azimuth angles), measurement quality information, and uncertainty parameters.

The L2A product contains information about the egg measurements only. This level groups the σ^0 measurement into rows and columns of wind vector cells (WVC). As mentioned, each WVC is a 25 kilometer square. The entire revolution can be divided up into 1624 WVC in the along track direction and 76 WVC in the cross track direction. The L2A file also includes 39 WVC rows from the previous rev at the beginning of the file and 39 rows from the following rev at the end of the file. The

total number of WVC rows contained in the L2A product is thus 1702. In the cross track direction the swath width is 1,800 km. Therefore 36 wind vector cell on each side of the for a total of 72 WVCs should be enough to include all σ^0 measurements. However variations in the attitude of the QuikSCAT satellite and the shape of the Earth, some σ^0 measurement fall outside of the boundary. Two extra WVCs on each side of the swath are included to accommodate these occasional outliers.

The L2B product is spatially ordered the same way as is the L2A product. This product, however, contains only wind vectors for each WVC. The number of wind vectors ranges from 1 to 4, corresponding to the number of ambiguities. The JPL selected ambiguity is also contained in this product for each WVC.

2.3 High Resolution Wind Retrieval

The JPL SeaWinds L2B wind product contains wind vectors for wind vector cells with resolution of 25 km. These wind vector estimates were retrieved using the “egg” measurement. Increased resolution in the wind vector cells can be done by exploiting the measurement geometry of the SeaWinds instrument.

As explained in the previous section, the antenna beam-limited footprint can be resolved into smaller elements by using range and Doppler filtering. The SeaWinds instrument is capable of resolving the footprint into twelve individual elements called “slices”. The best 8 of these “slices” are reported in the L1B data product. The slices are approximately 6 by 25 km.

The antenna rotation rate, pulse repetition frequency, and spacecraft velocity coupled together provide dense overlap in the spatial sampling of the surface by the slices. Using reconstruction and resolution enhancement algorithms, this over sampling is exploited to produce higher resolution images of σ^0 . The resolution enhancement algorithm used to produce the higher resolution σ^0 fields is the AVE algorithm [6], [7].

The AVE algorithm, developed by Long et al. [8], overlays a higher resolution grid on the σ^0 field. The width of each pixel in this higher resolution grid is 2.5 km. This pixel width correspond to the width of the high resolution wind vector

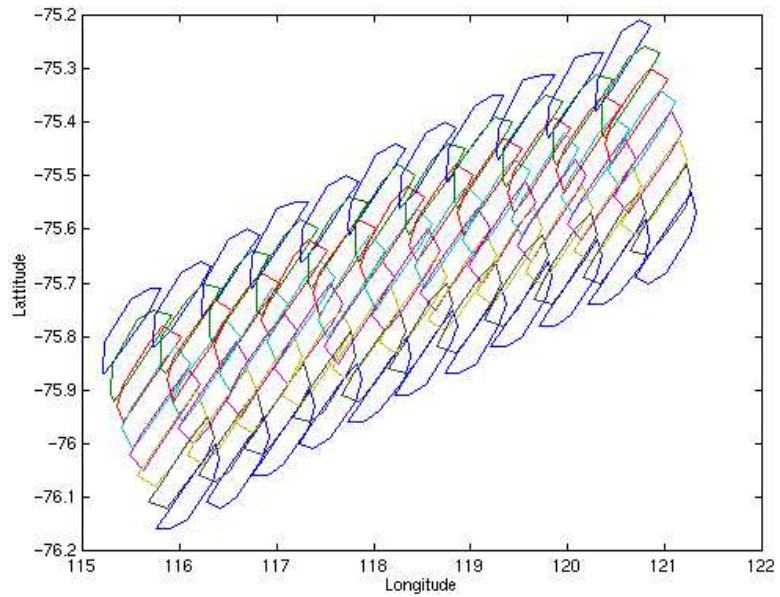


Figure 2.8: Illustration showing overlap in slice measurements due to the pulse repetition frequency of the SeaWinds instrument and size slice footprint. Image courtesy of Dr. David Long

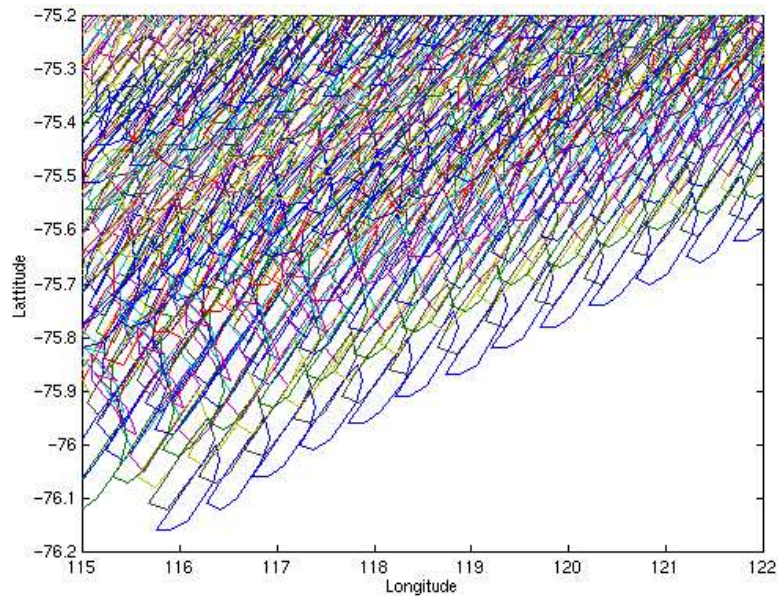


Figure 2.9: Illustration showing overlap in slice measurements due to the pulse repetition frequency and antenna spin rate. Image courtesy of Dr. David Long

cell. As mentioned previously, the geometry of the SeaWinds instrument allows most of the swath to be viewed 4 times: once by both the outer and inner beam looking forward as the satellite approaches and then again by the each beam looking in the aft direction as the satellite is leaving. The four different viewing geometries are used separately to construct four σ^0 fields. The dense oversampling of the Earth’s surface by the slices is then exploited to compute the weighted average value of σ^0 for each pixel. The AVE algorithms requires the spatial response function of each individual slice to compute the value of each pixel.

The four high resolution σ^0 fields are then passed to the wind retrieval algorithm. Each low resolution WVC (width 25km) is now subdivided into 100 high resolution WVCs. This increased resolution substantially increases the processing time. A product that looks at a small region of the Seawinds swath to produce high resolution wind data is now under development.

The σ^0 measurements for the higher resolution grid are noisier than are the σ^0 measurements for the lower resolution “egg” grid. This is due to the fact that the egg σ^0 measurements are formed from the sum of the reflected power in each of the slices in the antenna beam footprint. This summation averages out some of the noise.

As mentioned previously, other parameters are also required to retrieve the wind over the ocean. Therefore it is necessary to find these parameters for the higher resolution σ^0 measurements. These parameters include the azimuth angle and incidence angle of each σ^0 measurement. Also important are the variables reported in the L1B data product known as the K_p coefficients. These variables are used in the wind retrieval process. In this thesis methods for compositing σ^0 and these other parameters are derived.

As with the low resolution wind retrieval one to four wind vector solutions or ambiguities are produced for each high resolution wind cell or pixel. The first ambiguity selection method used is to chose the ambiguity whose direction is closest to the nearest L2B selected ambiguity. In pixels where less than the maximum of four σ^0 measurements are available the wind speed can be estimated (see Fig. 2.1) but the wind direction estimate accuracy is poor. More accurate ambiguity techniques are

thus required to increase the accuracy of the high resolution wind fields. The median filter approach to ambiguity selection is thus examined in this thesis.

Chapter 3

Compositing Slice Kp Coefficients

3.1 Introduction

The Seawinds instrument is capable of making two types of measurements. The first type, referred to as an egg, is made from the total power returned from the area of the footprint. The second type, referred to as a slice, is formed by using range and Doppler discrimination to get the power returned from a smaller section or slice of the footprint. These slices are used in the process of retrieving wind at high resolution.

The Seawinds data reports the predicted variances of both the egg measurement and the slice measurements. For composite wind retrieval, slices are averaged together to form a composite measurement which is then used in the wind retrieval process. The variance of these composite measurements is needed to accurately retrieve the wind estimate. It is therefore of interest to derive a method to calculate the variance of the composite measurements from the slice measurement variance. To do this we derive a method to compute the egg measurement variance from the slice measurement variances.

3.2 K_p

The accuracy of wind measurement made using a scatterometer depends greatly on the accuracy of the σ^0 measurements taken by the scatterometer. A commonly used metric for measuring the accuracy of the σ^0 measurement is K_p , sometimes referred to as K_{pc} . K_p is defined to be the normalized standard deviation of the σ^0

measurement given by

$$K_p = \frac{\sqrt{\text{VAR}[\sigma^0]}}{E[\sigma^0]}, \quad (3.1)$$

where $\text{VAR}[\sigma^0]$ is the variance of the σ^0 measurements and $E[\sigma^0]$ is the mean of the σ^0 measurements. For the Seawinds instrument aboard the QuikSCAT satellite, K_p for egg measurements is given by

$$K_p^2 = A^e + \frac{B^e}{\text{SNR}} + \frac{C^e}{\text{SNR}^2} \quad (3.2)$$

where SNR is the signal to noise ratio (P_s^e/P_n), A^e , B^e , and C^e are given (approximately) by

$$A^e = \frac{1}{B_{3dB}T_p} \quad (3.3)$$

$$B^e = \frac{2}{B_{egg}T_g} \quad (3.4)$$

$$C^e = \frac{1}{B_{egg}T_g} \left(1 + \frac{B_{egg}}{B_n}\right), \quad (3.5)$$

B_{egg} is the total egg bandwidth, T_p is the pulse length, T_g is the range gate length, B_{3dB} is the 3dB bandwidth of the total dechirped echo return, and B_n is the noise channel bandwidth.

3.3 K_p for Slices

K_p reported for slices in the QSCAT L1B data product has the same form as the egg K_p (Eq. 3.2). For slices A^s , B^s , and C^s are given by,

$$A_i^s = \frac{1}{B_s T_p} \quad (3.6)$$

$$B_i^s = \frac{2}{B_s T_g} \quad (3.7)$$

$$C_i^s = \frac{1}{B_s T_g} \left(1 + \frac{B_s}{B_n}\right) \quad (3.8)$$

where, as with the egg K_p coefficients, T_p is the pulse length, T_g is the range gate length, B_n is the noise bandwidth and B_s is the slice bandwidth. However, the approximation represented by these equations is not as good as for the egg.

Comparison of the egg and slice K_p coefficients reveals that they are essentially equal with the exception of the bandwidth of the measurement. In the egg K_p case B_{egg} and B_{3dB} are used. In [9] the total egg bandwidth, B_{egg} , is defined to be the sum of the bandwidths of the slices which are contained in the egg. B_{3dB} is a function of scan azimuth angle and orbit position. Therefore A^e becomes a function of azimuth angle and orbit position while A^s is treated as a constant for each pulse. A precise formulation is beyond the scope of this thesis, but we will seek a good approximation.

3.4 Compositing Slice K_p

To derive a method to composite K_p , an understanding of the normalized radar cross-section σ^0 is given. σ , the unnormalized radar cross-section is a function of the effective area of the scatterer, the amount of energy absorbed by the scatterer and the gain of the scatterer in the direction of the receiver. This is given by [3]

$$\sigma = A_{rs}(1 - f_a)G_{ts}. \quad (3.9)$$

Here f_a is the fraction of power absorbed by the scatter, A_{rs} is effective area of the scatter, G_{ts} is the gain of the scatterer in the direction of the receiver. The normalized radar scattering cross-section is given by

$$\sigma^0 = \frac{\sigma}{A_{rs}}. \quad (3.10)$$

The total power measured at the receive antenna is then given by

$$P_r = \frac{P_t G^2 \lambda^2 \sigma^0 A_{rs}}{(4\pi)^3 R^4} \quad (3.11)$$

where P_t is the transmitted power, G is the gain of the antenna, λ is the wave length of the transmitted power, and R is the slant range from the antenna to the scatterer. This equation is known as the radar equation [3]. It can be written simply as

$$P_r = X\sigma^0 \quad (3.12)$$

where X is the lumped elements of the radar equation. X is known as the X_{factor} in the L1B data.

3.4.1 Compositing σ^0

One of the first considerations before deriving a method for compositing K_p , is to derive the compositing method for σ^0 . The total power measured at the antenna is the sum of the power from each slice, i.e.

$$P_e = \sum_i P_{s,i}. \quad (3.13)$$

The total power is the power in the egg measurement (P_e). Substitution of Eq. 3.12 into Eq. 3.13 gives

$$\sigma_e^0 X_e = \sum_i \sigma_{s,i}^0 X_{s,i}. \quad (3.14)$$

The X_{factor} for the egg, X_e , is also the sum of each slice X_{factor} for a given pulse,

$$X_e = \sum_i X_{s,i}. \quad (3.15)$$

Therefore σ_e^0 can be expressed as the weighted average of $\sigma_{s,i}^0$ for each slice i in the given composite,

$$\sigma_e^0 = \frac{\sum_{i=1}^n \sigma_{s,i}^0 X_{s,i}}{\sum_{i=1}^n X_{s,i}}. \quad (3.16)$$

An analysis of compositing K_p using this method compared to a linear average composite σ^0 is presented in Appendix B.

3.4.2 Compositing K_p

To composite the slice K_p recall that K_p is defined to be the normalized standard deviation of the σ^0 measurement,

$$K_p = \frac{\sqrt{Var[\sigma^0]}}{E[\sigma^0]}. \quad (3.17)$$

To derive a compositing method for K_p the variance and mean of σ^0 must be examined. The variance of σ_e^0 is given by

$$Var[\sigma_e^0] = E[(\sigma_e^0)^2] - E[\sigma_e^0]^2$$

$$\begin{aligned}
&= E \left[\left(\frac{P_e}{X_e} \right)^2 \right] - E^2 \left[\frac{P_e}{X_e} \right] \\
&= E \left[\left(\frac{\sum_i P_{s,i}}{\sum_i X_{s,i}} \right)^2 \right] - E^2 \left[\frac{\sum_i P_{s,i}}{\sum_i X_{s,i}} \right] \\
&= \frac{\sum_i \sum_j E [P_{s,i} P_{s,j}]}{\left(\sum_i X_{s,i} \right)^2} - \left(\frac{\sum_i E [P_{s,i}]}{\sum_i X_{s,i}} \right)^2.
\end{aligned} \tag{3.18}$$

A simple noise model is [10]

$$\sigma_{s,i}^0 = \sigma_s^0 (1 + \nu_i K_{p,i}) \tag{3.19}$$

where ν_i is a unit variance, zero mean random variable which is uncorrelated from slice to slice. σ_s^0 is assumed to be a constant. Substituting Eq. 3.12 into Eq. 3.19 yields

$$\begin{aligned}
\frac{P_{s,i}}{X_{s,i}} &= \sigma_s^0 (1 + \nu_i K_{p,i}) \\
P_{s,i} &= \sigma_s^0 X_{s,i} (1 + \nu_i K_{p,i}).
\end{aligned} \tag{3.20}$$

With this noise model the cross correlation of the power in each slice is given by

$$\begin{aligned}
E [P_{s,i} P_{s,j}] &= E [(\sigma_s^0)^2 X_{s,i} X_{s,j} (1 + \nu_i K_{p,i}) (1 + \nu_j K_{p,j})] \\
&= (\sigma_s^0)^2 X_{s,i} X_{s,j} (1 + K_{p,i} K_{p,j} \delta_{i,j}).
\end{aligned} \tag{3.21}$$

The expected value of the power in the i^{th} slice can be written as

$$\begin{aligned}
E [P_{s,i}] &= \sigma_s^0 X_{s,i} (1 + K_{p,i} E[\nu_i]) \\
&= \sigma_s^0 X_{s,i}.
\end{aligned} \tag{3.22}$$

The variance and mean can now be written as

$$\begin{aligned}
Var[\sigma_e^0] &= \frac{\sum_i \sum_j (\sigma_s^0)^2 X_{s,i} X_{s,j} (1 + K_{p,i} K_{p,j} \delta_{i,j})}{\left(\sum_i X_{s,i} \right)^2} - \left(\frac{\sum_i \sigma_s^0 X_{s,i}}{\sum_i X_{s,i}} \right)^2 \\
&= (\sigma_s^0)^2 \frac{\sum_i \sum_j X_{s,i} X_{s,j}}{\left(\sum_i X_{s,i} \right)^2} + (\sigma_s^0)^2 \frac{\sum_i \sum_j X_{s,i} X_{s,j} K_{p,i} K_{p,j} \delta_{i,j}}{\left(\sum_i X_{s,i} \right)^2} - (\sigma_s^0)^2 \frac{\sum_i \sum_j X_{s,i} X_{s,j}}{\left(\sum_i X_{s,i} \right)^2}
\end{aligned}$$

$$= (\sigma_s^0)^2 \frac{\sum_i X_{s,i}^2 K_{p,i}^2}{\left(\sum_i X_{s,i}\right)^2} \quad (3.23)$$

$$E[\sigma_e^0] = \frac{\sum_i \sigma_s^0 X_{s,i}}{\sum_i X_{s,i}} = \sigma_s^0. \quad (3.24)$$

With the variance and the mean we obtain a compositing equation for the slice K_p ,

$$K_p^2 = \frac{Var[\sigma_e^0]}{(E[\sigma_e^0])^2} = \frac{(\sigma_s^0)^2 \frac{\sum_i X_{s,i}^2 K_{p,i}^2}{\left(\sum_i X_{s,i}\right)^2}}{(\sigma_s^0)^2} = \frac{\sum_i X_{s,i}^2 K_{p,i}^2}{\left(\sum_i X_{s,i}\right)^2}. \quad (3.25)$$

3.4.3 Compositing K_p equation coefficients

Definitions of the K_p equation coefficients A , B , and C are given in Sections 3.2 and 3.3 for egg and slice measurements respectively. Here, methods to equate the slice K_p equation coefficients are derived.

A coefficient

The A coefficient for the slice measurement differs from the egg A coefficient by the bandwidth used (see Eqs. 3.3 and 3.6). For the egg A coefficient the bandwidth used is the 3dB egg bandwidth. This bandwidth is dependent on which beam, inner or outer, and azimuth angle. The slice A coefficient uses the bandwidth of a slice. This value is constant and therefore so is the A coefficient.

Using the compositing method derived for K_p the A^e coefficients can be approximately found from the A^s coefficients,

$$A^e = \frac{\sum_i X_{s,i}^2 A_i^s}{\left(\sum_i X_{s,i}\right)^2}. \quad (3.26)$$

From Figure 3.1 it can be seen that the composited A^s (all slices approximately equals egg) correctly follows the shape of the A^e coefficient with a small bias. The mean value of this bias is 0.0015.

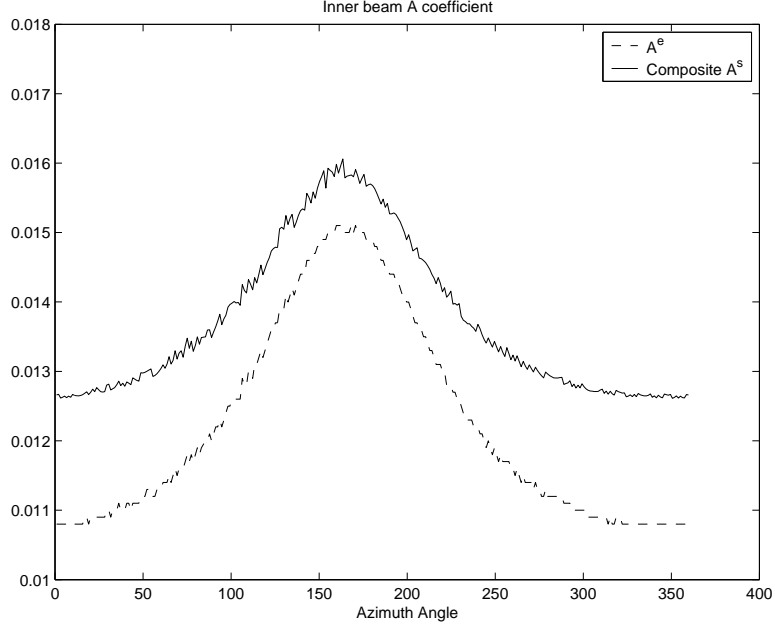


Figure 3.1: Egg A coefficient and composited slice A coefficient.

B and C coefficients

The B and C coefficients for the egg and the slice differ by only a constant. This is due to the fact that, for the egg, the bandwidth used to compute these coefficients is B_e , and for the slice the bandwidth used is B_s . B_e is the sum of the bandwidths of the slices used in the egg measurement, i.e.

$$B_{egg} = N \cdot B_s. \quad (3.27)$$

Nominally the center 10 slices are used in the egg calculation, $N=10$. Using Eqs. 3.4, 3.5, 3.7, and 3.8 we now have a compositing method for the B and C coefficients.

$$B^e = \frac{2}{B_{egg}T_g} = \frac{2}{N \cdot B_sT_g} = \frac{1}{N}B^s \quad (3.28)$$

$$\begin{aligned} C^e &= \frac{1}{B_{egg}T_g} \left(1 + \frac{B_{egg}}{B_n}\right) = \frac{1}{N \cdot B_sT_g} \left(1 + \frac{N \cdot B_s}{B_n}\right) \\ &\approx \frac{1}{N}C^s \end{aligned} \quad (3.29)$$

where N is the number of slices summed.

Compositing slice SNR

The method for compositing the SNR is the same as the method use to composite the slice σ^0 ,

$$SNR^e = \frac{\sum_i SNR_i^s X_{s,i}}{\sum_i X_{s,i}}. \quad (3.30)$$

This method introduces a small bias between the egg SNR and the composite slice SNR.

3.5 Comparison With Empirically Calculated K_p

To verify the methods derived in the previous sections we look at the observed normalized standard deviation of σ^0 . This is done by finding regions of semi-homogeneous backscatter, then calculating the standard deviation of the σ^0 measurements and normalizing by the mean (see Eq. 3.1).

The regions chosen here are shown in Fig. 3.2. Region 1 is over the Amazon rain forest. This region has a high value of σ^0 . Region 2, was chosen for its lower value of σ^0 . Note that due to spatial variation in the region the empirical K_p is expected to be larger than the predicted K_p

From Figure 3.3 it can be seen that Region 1 has a lower empirical K_p than does Region 2. Examination of Fig. 3.2(b) shows that Region 1 is more homogeneous than is Region 2, therefore explaining the difference in the empirical K_p . The mean value of predicted K_p reported for the eggs in both regions is approximately the same. This is due to the fact that the SNR is relatively high in both regions and therefore the value of the predicted K_p is mainly dependent on the A coefficient. The difference in the empirical K_p and the predicted K_p comes from the surface inhomogeneity. The empirical K_p is not only a function of the communication K_p but also a function of the surface K_p .

In Figure 3.3 the results of the two compositing methods outlined in this report are also shown. Method 1 refers to first calculating the K_p value for every slice using the method outlined in section 3.3, then compositing each of the K_p values for the

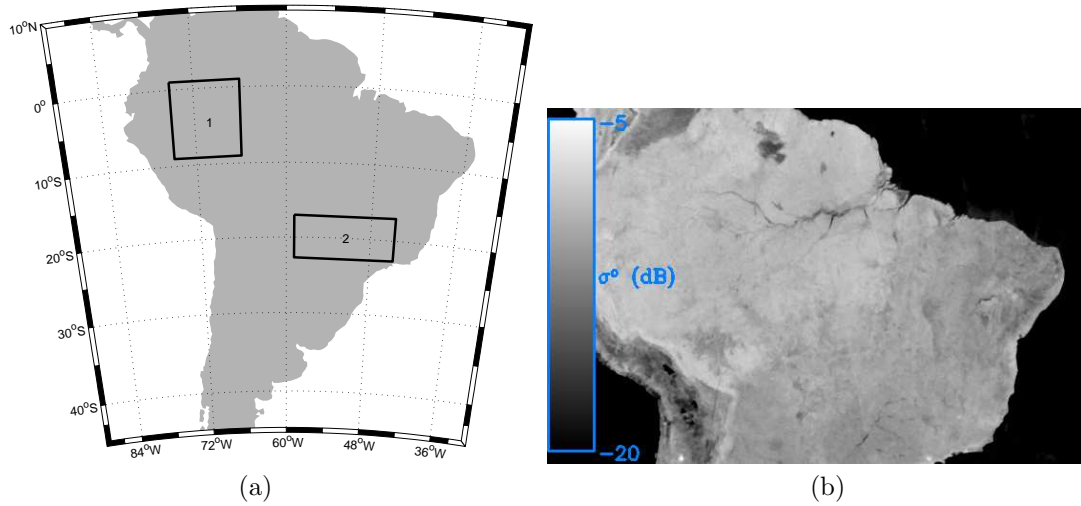


Figure 3.2: (a) Regions of homogeneous backscatter used in study. (b) SIR images showing backscatter. (quev-a-Ama01-257-260.sir)

slice in a given pulse using Eq. 3.25. This method shows very good results when compared to the predicted egg K_p .

Method 2 uses the method outlined in Section 3.4.3. Here each of the coefficients are composited separately. This method is comparable to method 1, with only slightly better results for the added computation.

3.6 Conclusion

A method for computing K_p for composited slices from the K_p coefficients in QuikSCAT data is derived and tested. The method to accurately composite σ^0 is also derived and tested. These two methods are very important steps to increasing the accuracy of the high resolution winds. The compositing methods derived in this section were developed for compositing slices from the same pulse. These methods can be applied to the high resolution σ^0 fields discussed in Chapter 2 to accurately average slice measurements from different pulses along with the parameters associated with the σ^0 measurements which are used in the wind retrieval processing.

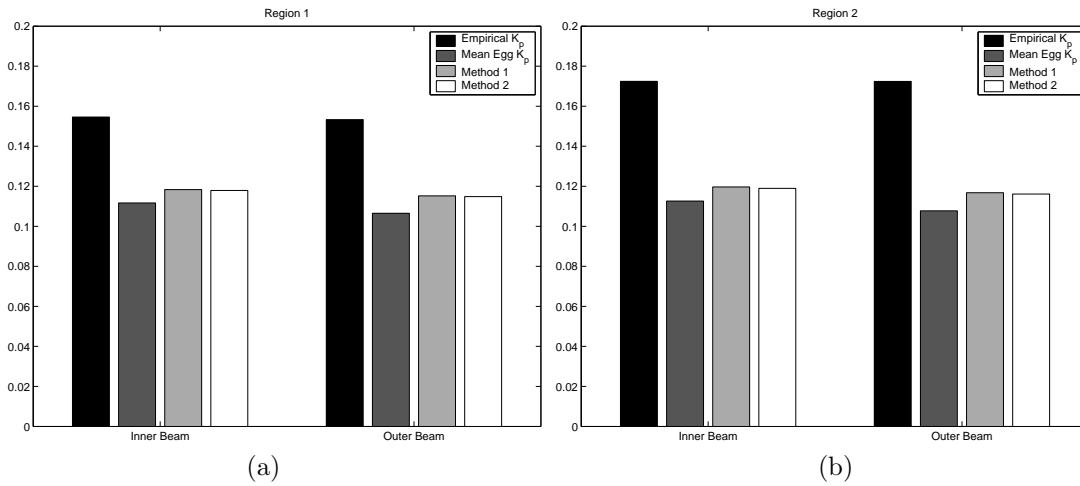


Figure 3.3: K_p values for both regions in Figure 3.2. The empirical K_p is found using Eq. 3.1. The Mean Egg K_p value is the mean value of the egg measurement predicted K_p calculated using the method outlined in section 3.2. Method 1 refers to the mean value of K_p calculated from the slice K_p using Eq. 3.25. Method 2 refers to the mean value of K_p calculated from the slice K_p using method outline in section 3.4.3. The number of measurements for each region and beam are: Region 1 inner beam 25,024, outer beam 23,166, Region 2 inner beam 12,320, and outer beam 12,765

Compositing method for σ^0

$$\sigma_e^0 = \frac{\sum_{i=1}^n \sigma_{s,i}^0 X_{s,i}}{\sum_{i=1}^n X_{s,i}}$$

Method 1 for compositing K_p

$$K_p^2 = \frac{\sum_i X_{s,i}^2 K_{p,i}^2}{\left(\sum_i X_{s,i}\right)^2}$$

Method 2 for compositing K_p

$$K_p^2 = A_{comp} + \frac{B_{comp}}{SNR_{comp}} + \frac{C_{comp}}{SNR_{comp}^2}$$

Where

$$A_{comp} = \frac{\sum_i X_{s,i}^2 A_i^s}{\left(\sum_i X_{s,i}\right)^2}$$

$$B_{comp} = \frac{B^s}{N}$$

$$C_{comp} = \frac{C^s}{N}$$

$$SNR_{comp} = \frac{\sum_i SNR_i^s X_{s,i}}{\sum_i X_{s,i}}$$

Figure 3.4: Summary of K_p compositing methods

Chapter 4

Increased Accuracy in Retrieved High Resolution Winds Through Bias Correction

4.1 Introduction

The process of accurately estimating the near surface wind speed and direction over the ocean from the measured radar cross section requires the knowledge of several factors. As mentioned in section 2.1, these factors range from how the wind interacts with the ocean surface to how microwave energy reflects from roughened sea surfaces. While several of these factors are known, some are not. It is for this reason that an empirically-derived model function is used to relate the near surface winds to the radar cross section of the ocean surface.

Simulations, testing the accuracy of wind retrieval, have revealed a small bias in both wind speed and direction which increases with increasing wind speed. The bias as a function of wind direction has approximately two to four peaks across the range of possible wind directions. The location of these peaks is dependent on the location across the swath. This dependence is related to the measurement sampling geometry of the SeaWinds instrument.

To increase the accuracy of the retrieved wind vectors the retrieved wind vector is adjusted by this bias. A 3-dimensional table is compiled containing the predicted bias for a given wind vector cell, wind speed and wind direction. This table is then included in the wind retrieval processing in a post-estimation step.

The methods used to compute the bias and the results of the bias corrections for simulated data are examined in this chapter. The bias is examined first for the

low resolution wind. The high resolution wind bias is then examined and compared to the low resolution bias.

4.2 Low Resolution Bias

The Geophysical Model Function relates the radar cross section σ^0 to the near surface wind over the ocean. As previously explained, the geophysical model function can be written as

$$\sigma_0 = f(|U|, \chi, \theta, f, pol) \quad (4.1)$$

where $|U|$ is the wind speed, χ is the azimuth angle between the wind vector and the incident radiation (see Fig. 2.6), θ is the incidence angle (see Fig. 2.6), f is the frequency of the incident radiation, and pol is the polarization of the incident radiation.

Estimation of the wind vector involves inverting the model function i.e., given a measured radar cross section σ^0 , measured at a given frequency, polarization, incidence angle, and relative azimuth angle, what is the wind speed and direction? The accuracy of the inversion can truly be found only if the true wind speed and direction are known. An approximation of the accuracy can be found through simulations. These simulations involve acquiring simulated σ^0 values from the forward model function given a wind speed, wind direction, incidence angle, azimuth angle, frequency and polarization. The known sampling geometry of the SeaWinds instrument can be used to acquire sufficient simulated σ^0 measurements to then use the inverted model function to get a simulated retrieved wind vector. The error between the simulated true wind vector and the simulated retrieved wind can then be calculated for both wind speed and direction.

The SeaWinds sampling geometry is dependent on the location across the swath i.e., the distribution of azimuth and incidence angles is dependent on the wind vector cell. To aid in the illustration of this concept a brief description of the low resolution wind data product follows. The JPL produced SeaWinds L2B data product

contains wind vectors solutions obtained using the “egg” measurements. The resolution of the wind vectors reported is a 25 km x 25 km cell known as a wind vector cell (WVC). The SeaWinds instrument has a swath width of 1800 km. The swath is divided into 72 wind vector cells. Two extra wind vector cells are included on each side of the swath for occasional outliers. Thus the swath is 76 wind vector cells wide. In this study only the inner 72 wind vector cells are considered. It is assumed that the sampling geometry is independent of the along track row.

To test the effectiveness of the simulation method for estimating the accuracy of the wind retrieval a range of true wind speeds and directions is used. The simulated true wind speed is chosen to range from 3 to 30 m/s while the wind direction is chosen to range from 0° to 359°. As mentioned previously, other parameters are also needed to obtain a simulated σ^0 measurement from the model function. These include the incidence angle, relative azimuth angle, frequency and polarization of the incident radiation. These parameters are extracted from the SeaWinds data for WVC 20. Simulated σ^0 are then obtained for the parameters in WVC 20. These simulated σ^0 measurements are noise free. To estimate the bias as accurately as possible two sources of noise must be accounted for. The first type of noise is communication noise. This noise is caused by the effects of fading and thermal noise. We model this noise as white Gaussian noise and modify the noise free σ^0 measurement using,

$$z_i = \sigma_i^0 (1 + K_p \cdot \nu_i) \quad (4.2)$$

where σ_i^0 is the i^{th} measurement of the given WVC in linear space, ν_i is a white Gaussian random variable, K_p is the normalized standard deviation of σ^0 ,

$$K_p = \sqrt{\frac{variance}{(\sigma^0)^2}} \quad (4.3)$$

where

$$variance = \left((\alpha (1 + K_{pm}^2) - 1) \sigma^0 + \beta \right) \sigma^0 + \gamma \quad (4.4)$$

with α , β , and γ known as the variables of the variance equation. For this study these variables are extracted from the SeaWinds data file for row 456 WVC 20 of rev 12950.

These parameters, unlike the measurement geometry parameters are, independent of location in the swath. They are functions of the signal to noise ratio, the bandwidth of the received power measurement and the range gate length.

The second type of noise is caused by uncertainties in the model function. This noise is also modeled as white Gaussian noise with variance K_{pm}^2 . The value of K_{pm} is tabulated with the model function. The simulated noisy σ^0 measurement is then given by,

$$\sigma_{\eta,i}^0 = \sigma_i^0 (1 + K_p \cdot \nu_i) (1 + K_{pm} \cdot \nu'_i). \quad (4.5)$$

For each true wind speed and direction pair 100 realizations of the random variable $\sigma_{\eta,i}^0$ are obtained for each σ^0 in the WVC. This provides 100 samples of the simulated retrieved wind for each true wind speed and direction pair. The error in the simulated retrieved wind is found by subtracting the simulated retrieved wind from the true wind. This is a straight forward process for the wind speed but finding the error in the wind direction requires extra measures to take into account the circular nature of the directions.

Two methods for binning the errors are tested in this study. The first is to bin the error by the true wind speed and direction. This method is not possible in practice since the true wind is not known. It is included in this study for verification only. The second method is to bin the data by the retrieved wind speed and direction. These two methods are examined in Sections 4.2.1 and 4.2.2.

4.2.1 Wind bias binned by true wind speed and direction

The speed and direction errors between each simulated retrieved wind vector and the corresponding true wind vector are binned into a two dimensional histogram. The two dimensions in this case correspond to the true wind speed and the true wind direction. The errors in each bin are statistically evaluated to find the mean and RMS of the errors. These quantities are given by

$$\bar{E}_{s(i,j)} = \frac{1}{N} \sum_{n=1}^N (Ut_{(i,j)n} - Um_{(i,j)n}) \quad (4.6)$$

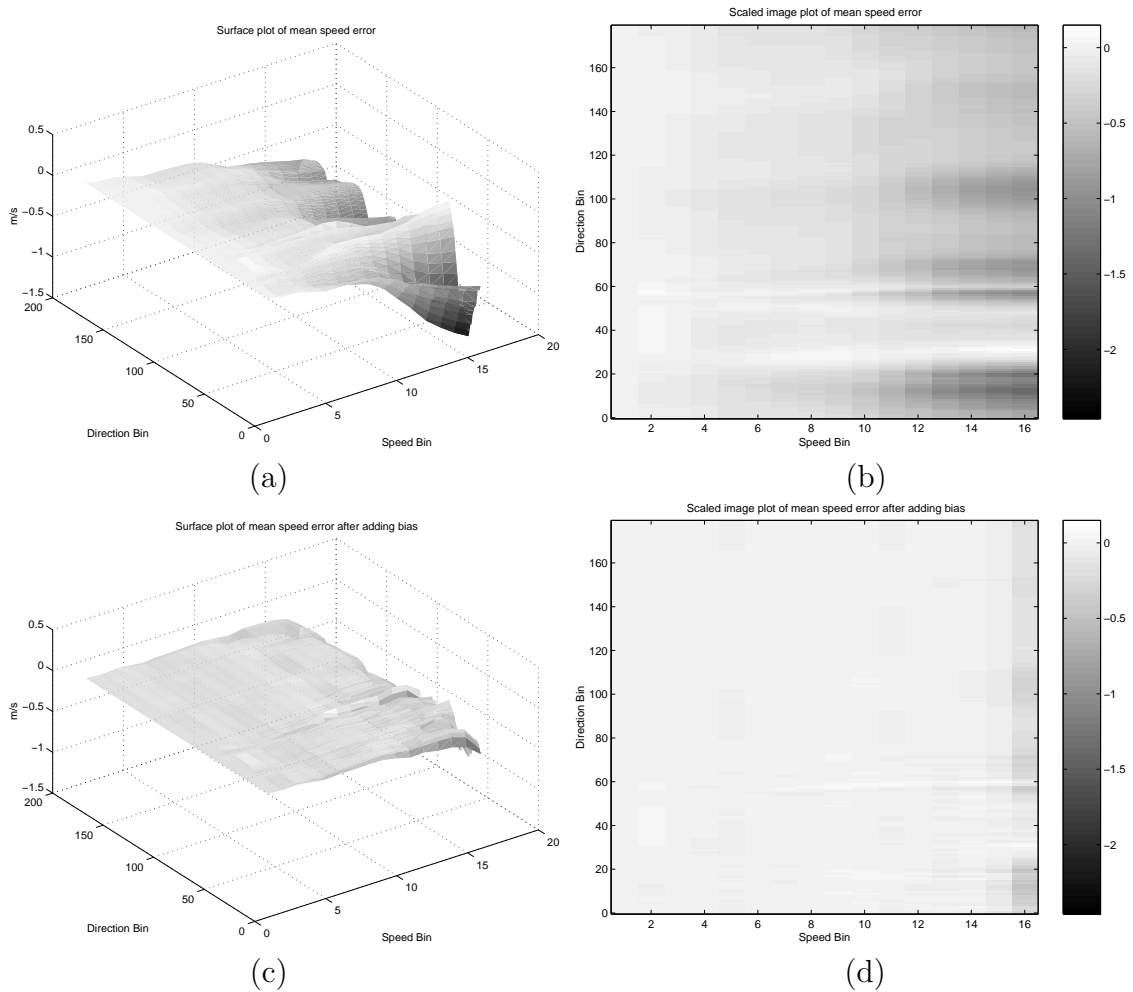


Figure 4.1: Mean wind speed error binned by true wind speed and direction, Figures (a) and (b) are plots of the mean speed error in each bin. Figures (c) and (d) are plots of the mean speed error after bias correction.

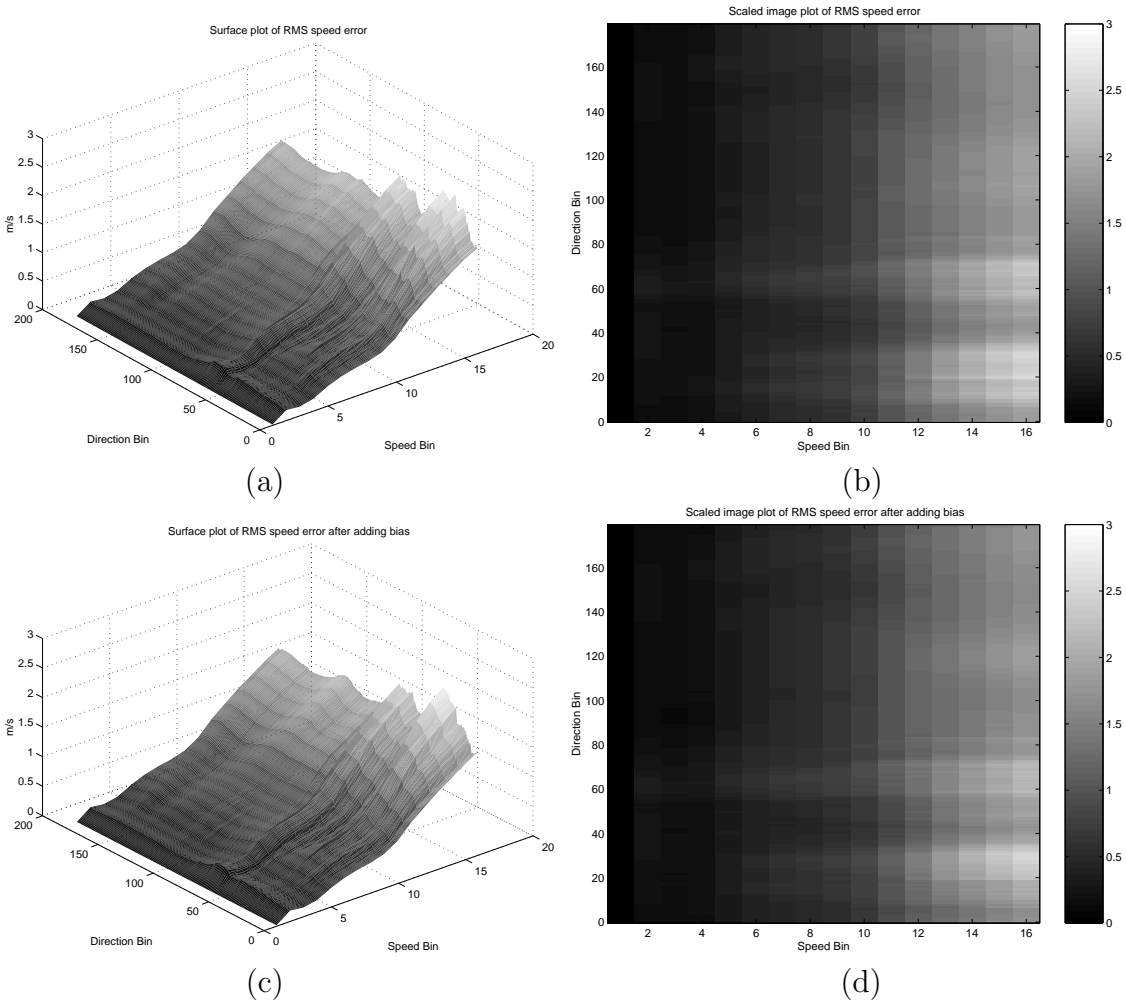


Figure 4.2: RMS wind speed error binned by true wind speed and direction. Figures (a) and (b) are plots of the RMS speed error in each bin. Figures (c) and (d) are plots of the RMS speed error after bias correction.

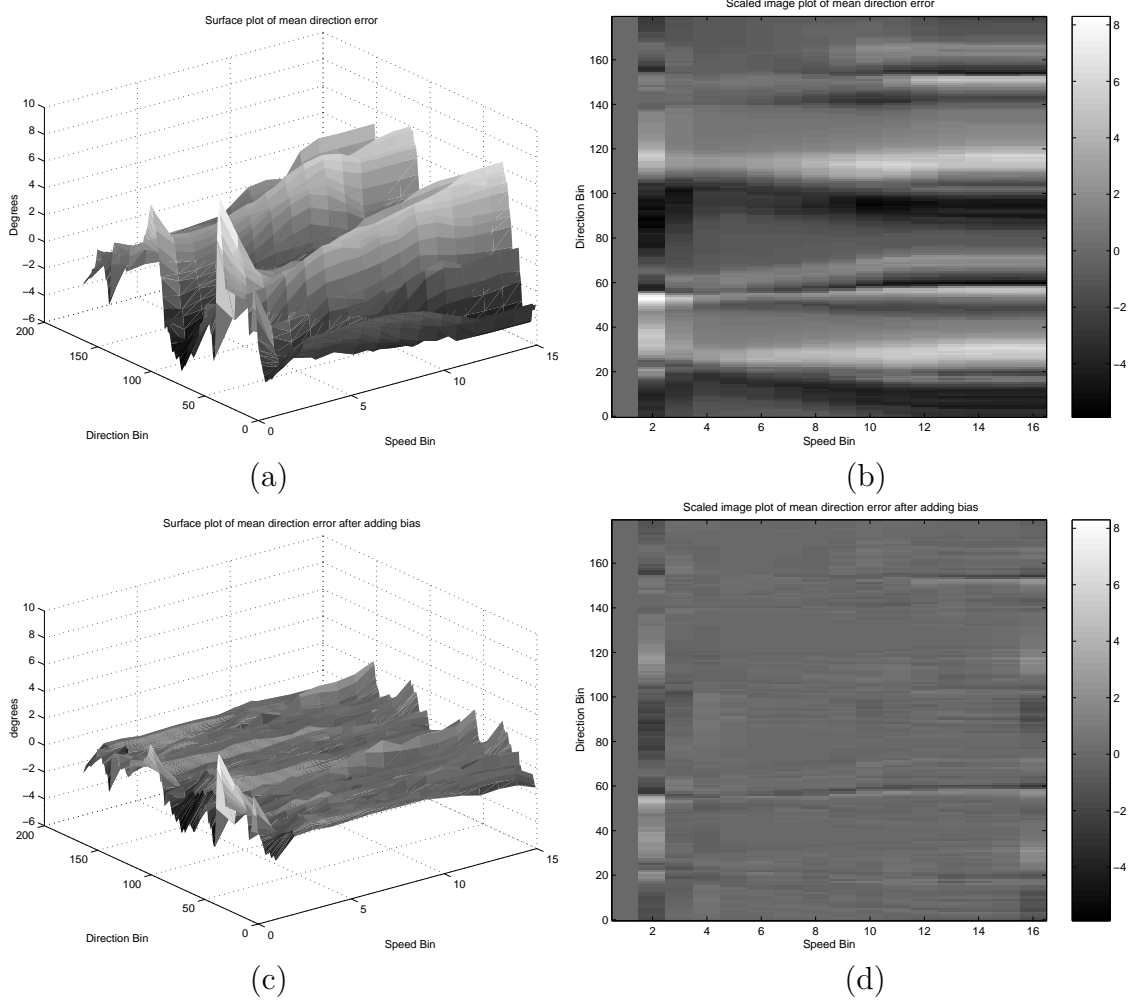


Figure 4.3: Mean wind direction error binned by true wind speed and direction. Figures (a) and (b) are plots of the mean wind direction error in each bin. Figures (c) and (d) are plots of the mean wind direction error in each bin after bias correction.

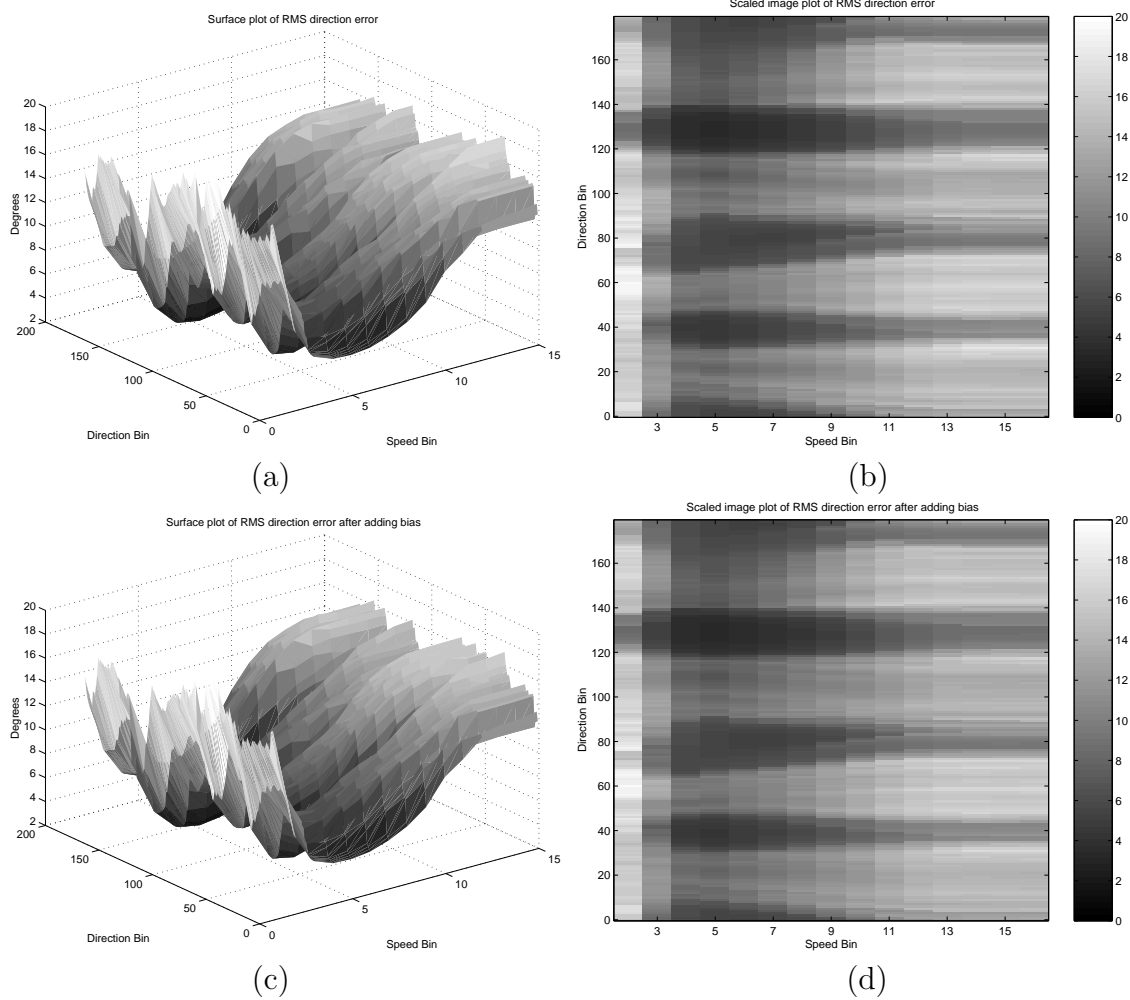


Figure 4.4: RMS wind direction error binned by true wind speed and direction. Figures (a) and (b) are plots of the RMS wind direction error in each bin. Figures (c) and (d) are plots of the RMS wind direction error in each bin after bias correction.

$$RMS_{s(i,j)} = \sqrt{\frac{1}{N} \sum_{n=1}^N (Ut_{(i,j)n} - Um_{(i,j)n})^2} \quad (4.7)$$

where $\bar{E}_{s(i,j)}$ is the mean wind speed error of the i, j^{th} bin, $RMS_{s(i,j)}$ is the RMS wind speed error of the i, j^{th} bin, $Ut_{(i,j)}$ is the true wind speed and $Um_{(i,j)}$ is the simulated or measured wind speed. A similar method is used to find the statistics of the wind direction error taking into account the wrap around in degrees.

This produces two 2-dimensional look-up tables for the bias, one for the wind speed and one for the wind direction. The RMS error tables are also included for visualization of the error. To test the bias removal method the simulation is run again, this time updating the retrieved wind with the previously computed bias from the look up tables. The results of this process are illustrated in Figures 4.1 through 4.4. Figure 4.1 shows substantial improvement in the wind speed error when the bias is subtracted from each retrieved wind speed measurement. As expected, the mean speed error is close to zero. The RMS speed error, however, only shows a small improvement, see Fig. 4.2. The mean error in the wind direction also shows substantial improvement when the retrieved wind direction is adjusted by subtracting the corresponding bias, see Fig. 4.3. Again the RMS direction error only shows a slight improvement using the bias correction, Fig 4.4.

4.2.2 Wind bias binned by retrieved wind speed and direction

A substantial improvement is seen in the mean speed and direction error in each bin when a bias correction based on the true wind is applied to the retrieved wind. The method used however is not practical to implement because the true wind is not known for real measurements. The second method, binning the errors by the retrieved wind speed and direction, is a more practical method but is less accurate. This method is analyzed in this section.

As in the previous section the errors in speed and direction are found for a range of true wind speed and directions. This time, however, the errors are binned by the simulated retrieved wind speeds and directions. The ambiguity selected for the binning is the ambiguity closest to the true wind. Again two, 2-dimensional tables

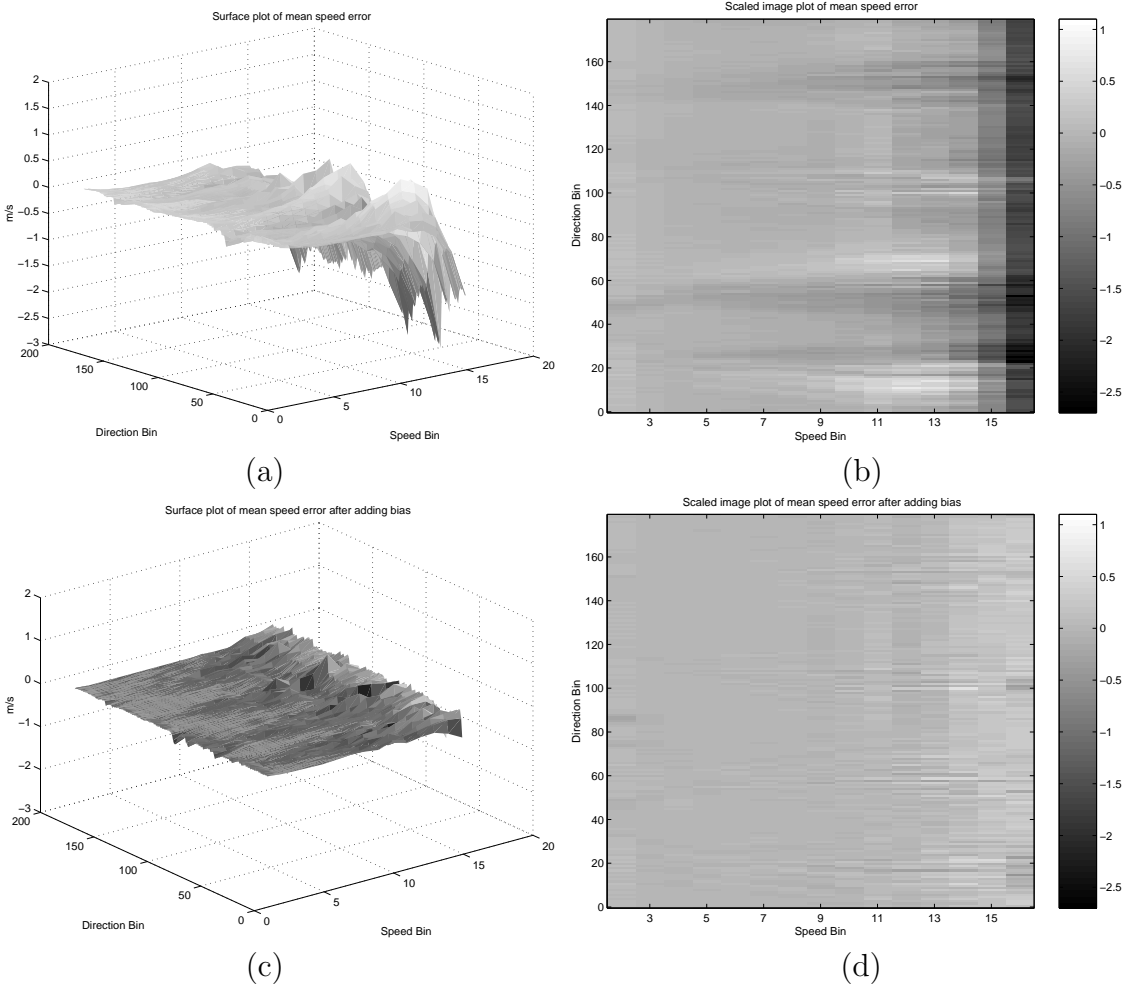


Figure 4.5: Mean wind speed error binned by simulated wind speed and direction, Figures (a) and (b) are plots of the mean speed error in each bin. Figures (c) and (d) are plots of the mean speed error after bias correction.

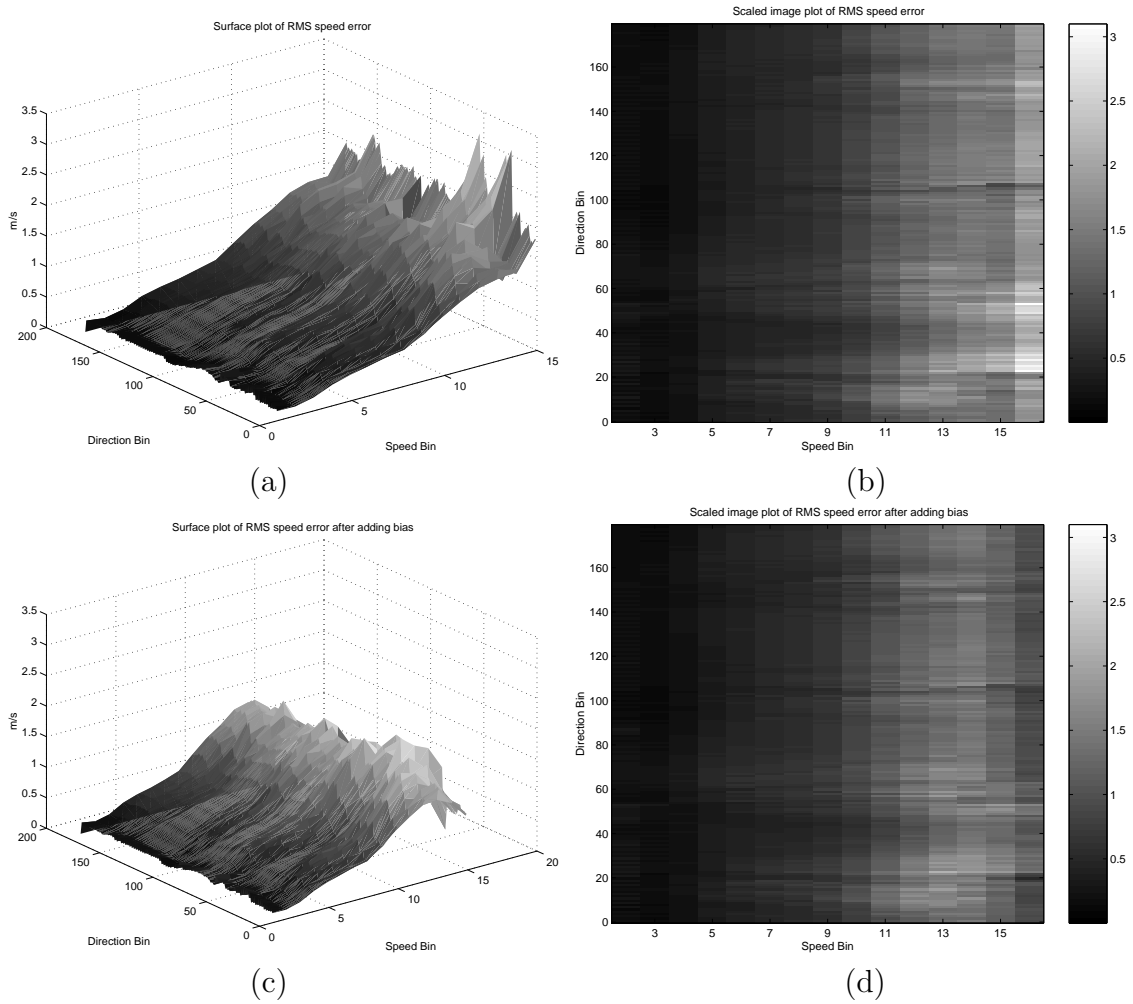


Figure 4.6: RMS wind speed error binned by simulated wind speed and direction. Figures (a) and (b) are plots of the RMS speed error in each bin. Figures (c) and (d) are plots of the RMS speed error after bias correction.

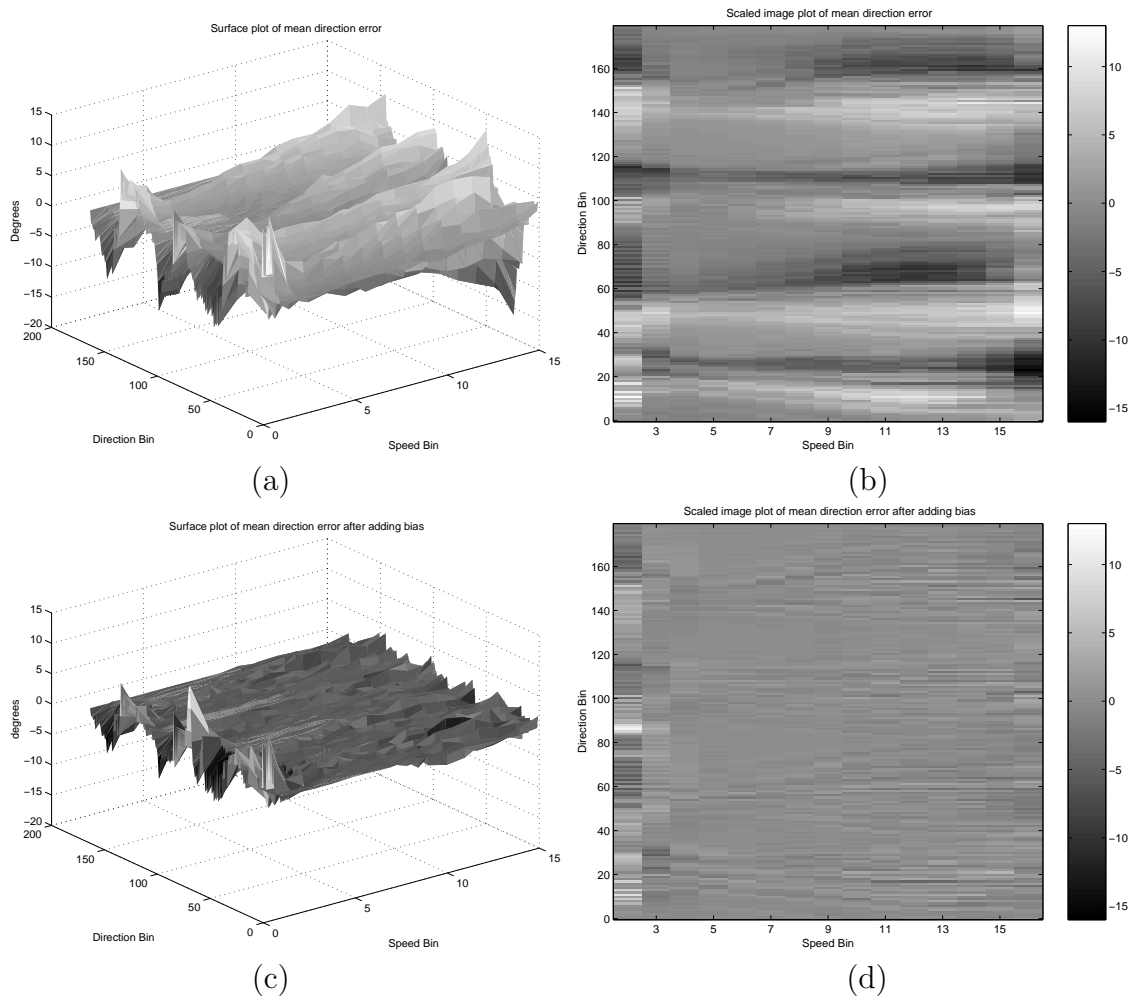


Figure 4.7: Mean wind direction error binned by simulated wind speed and direction. Figures (a) and (b) are plots of the mean wind direction error in each bin. Figures (c) and (d) are plots of the mean wind direction error in each bin after bias correction.

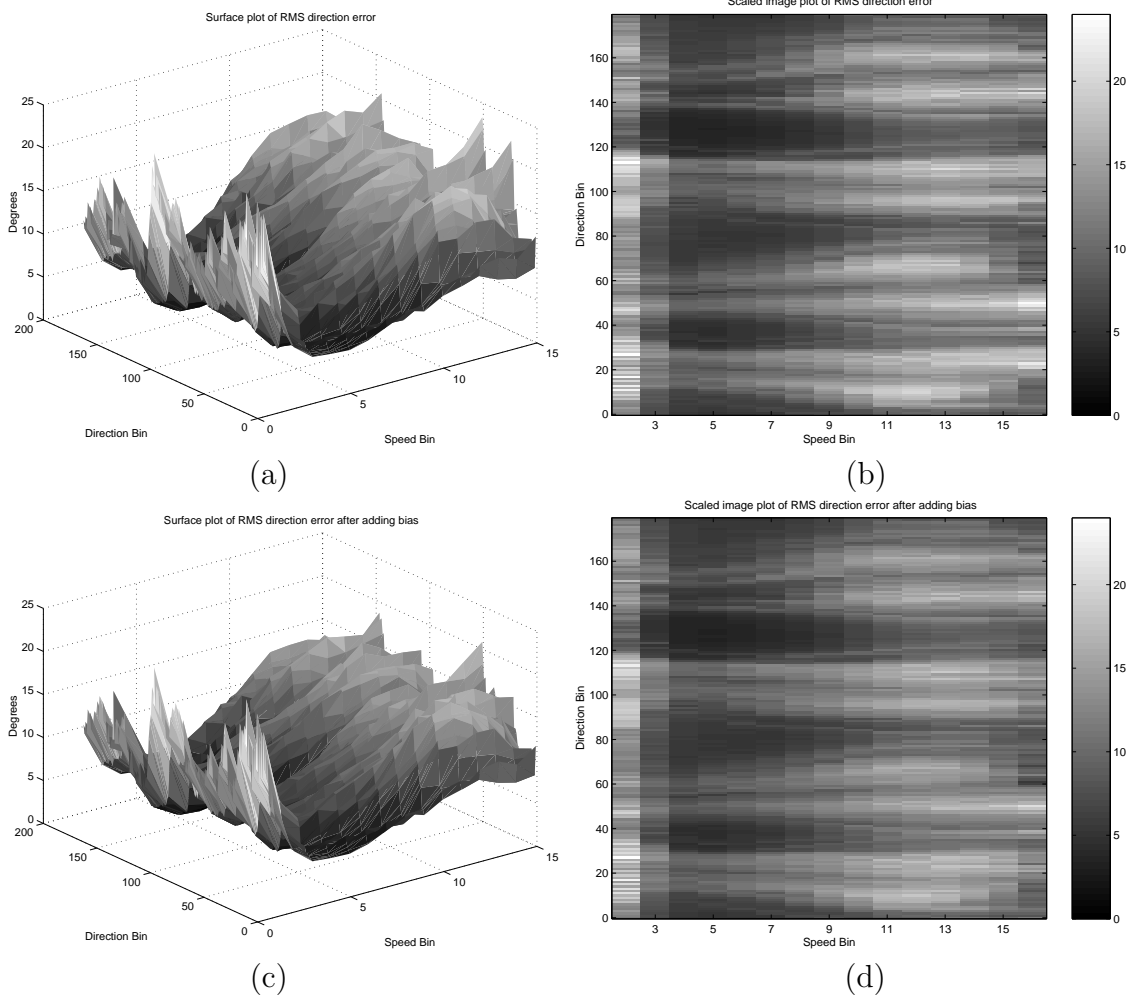


Figure 4.8: RMS wind direction error binned by simulated wind speed and direction. Figures (a) and (b) are plots of the RMS wind direction error in each bin. Figures (c) and (d) are plots of the RMS wind direction error in each bin after bias correction.

are produced containing the errors in speed and the errors in direction at each wind speed and direction combination. The method of bias removal is again tested by repeating the test and adjusting the retrieved wind speeds and directions with the corresponding bias. The results of this method are illustrated in Fig 4.5 through 4.8. In Fig. 4.5 the mean speed error in each bin is shown along with the bias corrected mean speed error. Again a substantial improvement is seen in the mean speed error. The RMS speed error, shown in Fig 4.6 for both the unadjusted and bias adjusted cases. The RMS speed error, showing only a small improvement at low wind speeds, is better at high wind speeds when the retrieved wind speed is adjusted by the bias. The mean direction error also shows improvement. The bias is removed in most cases, but at low wind speeds the lack of sufficient samples to compute the bias accurately doesn't allow the bias to be removed successfully. The RMS direction error shows only a small improvement, see Figs. 4.7 and 4.8.

4.3 High Resolution Bias

High resolution bias refers to the bias in wind direction and speed when the modified sampling geometry of the high resolution wind retrieval algorithm is used. As explained in the previous section, the low resolution wind retrieval algorithm uses the “egg” σ^0 measurements with the sampling geometry parameters, such as azimuth angle and incidence angle that correspond to each σ^0 measurement in the wind vector cell. In the high resolution case the “slice” measurements are used. These slice measurements are not used directly to retrieve the wind. As mentioned in Chapter 2 an averaging algorithm is used. The low resolution wind retrieval algorithm uses a WVC grid of 25 km x 25 km cell. All of the “egg” measurements whose *centers* fall in a given WVC are used to estimate a wind vector for that WVC. In the high resolution case a more dense grid is laid on top of the low resolution grid. This higher density grid has wind vector cells that are 2.5 km x 2.5 km. The slices that *cover* each high resolution cell from a particular beam (inner, outer, forward-looking, and aft-looking) are averaged together as are their corresponding sampling geometry parameters. This provides between 2 and 4 σ^0 measurements per high resolution WVC.

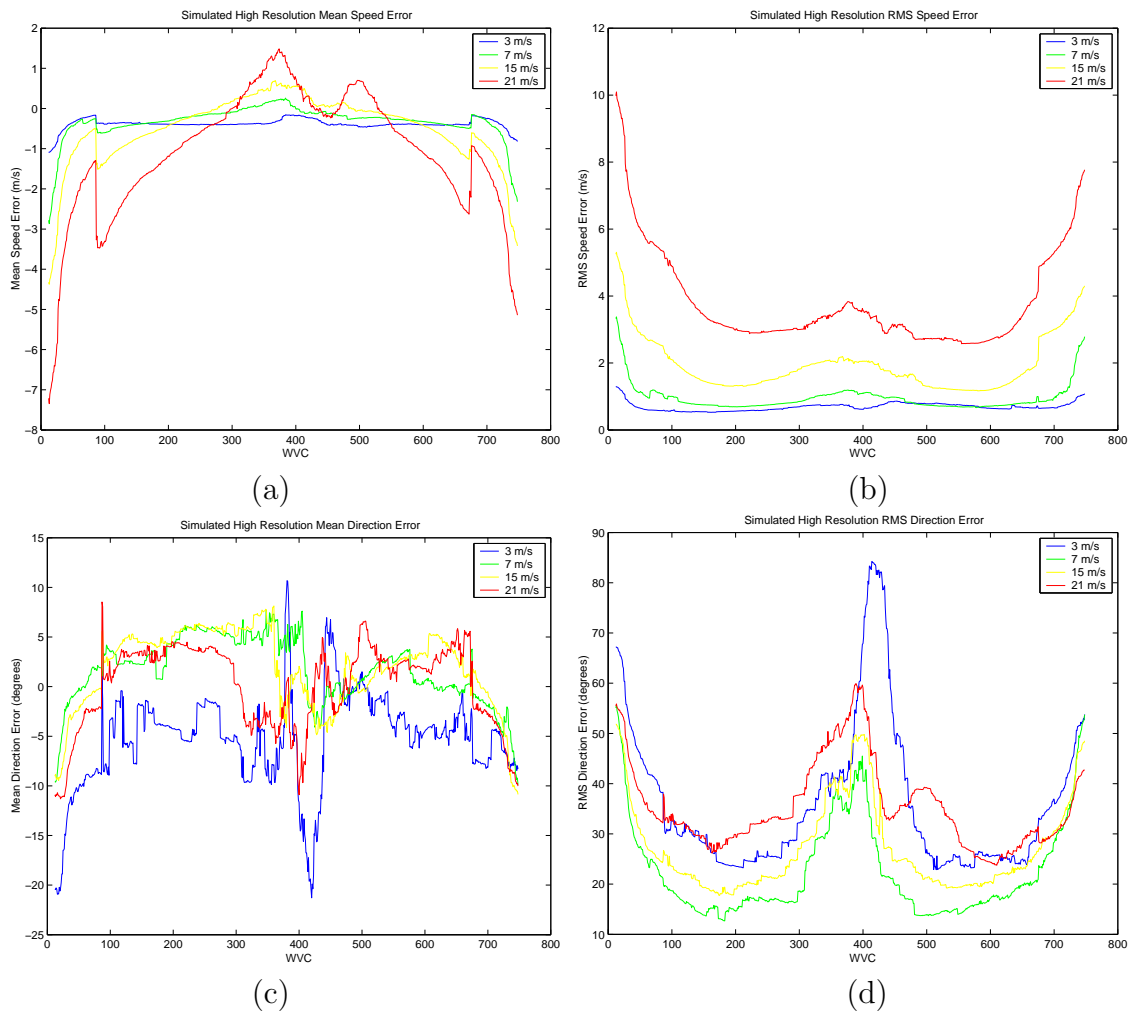


Figure 4.9: Mean and RMS errors in wind speed and direction verses high resolution wind vector cell. Data was obtained using true wind speeds shown and true wind direction of 273° .

The slice measurements are inherently more noisy than are the corresponding egg measurements. This increased noise also increases the bias seen in the retrieved winds. In the simulations this noise is quantified in the α , β , and γ coefficients explained in section 4.2.

Figure 4.9 shows the mean and RMS errors between the simulated true wind and the retrieved wind vectors for true wind speeds of 3, 7, 12, and 21 m/s and true wind direction of 273° . The errors are plotted verses the cross track wind vector cell.

The largest error in wind speed occurs at the swath edges and at the center track location. The largest error in the wind direction occurs at the center track location. This large error at the center track location is due to symmetry of the model function. With azimuth angles that are approximately 180° apart it is possible to retrieve a wind direction that is 180° off of the true wind direction. In the far swath regions error is caused by poor sampling geometry. Here only the outer beam is able to make measurements. This geometry only provides at most two measurements to use in the wind retrieval process.

To test the bias removal method, simulations are performed for a range of wind speeds and directions. The errors in the wind speeds and direction are binned by the retrieved wind speed and direction. The mean of the error in each bin is computed and tabulated. The wind speed error table is shown in Fig. 4.10(a). The wind direction error table is shown in Fig. 4.10(c). The sample mean is used for the estimate of the mean wind errors. A measurement of how good this estimate is can be found by measuring the standard error of the mean. The standard error of the mean is the standard deviation of the sampling distribution of the mean. It is given by

$$\sigma_M = \frac{\sigma}{\sqrt{N}} \quad (4.8)$$

where σ is the standard deviation of the original distribution and N is the number of samples used in the computation of the mean. The standard error of the mean was computed for each bin. Figure 4.11 shows the value of the standard error of the mean for wind vector cell 200. Figure 4.11(a) illustrates that the sample mean is a good estimate for the mean when computing the wind speed bias. In Figure 4.11(b) it can be seen that at low wind speed the standard error of the mean is quite large, however for most of the wind speed and direction range the sample mean is a good estimate for the mean wind direction error.

The wind retrieval simulation is repeated again this time adjusting each measurement by the corresponding bias in wind speed and direction. The measurements are then binned by the retrieved wind speed and direction. The mean of the error in

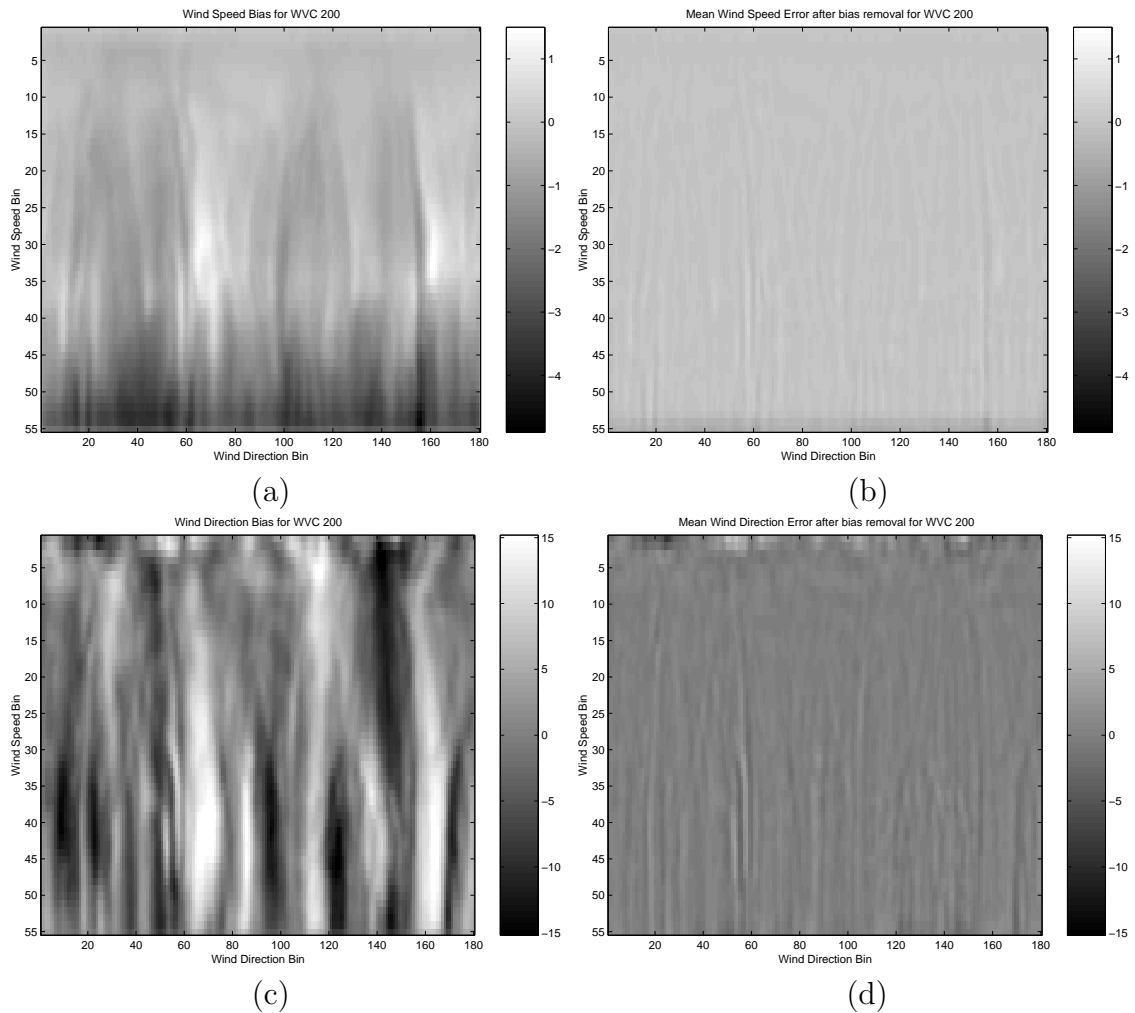


Figure 4.10: (a) Mean wind speed error binned by wind speed and wind direction. (b) Mean wind speed error after bias adjustment binned by wind speed and direction. (c) Mean wind direction error binned by wind speed and direction. (d) Mean wind direction error after bias adjustment binned by wind speed and direction. Wind speed bins are 0.5 m/s wide. Wind direction bins are 2° wide.

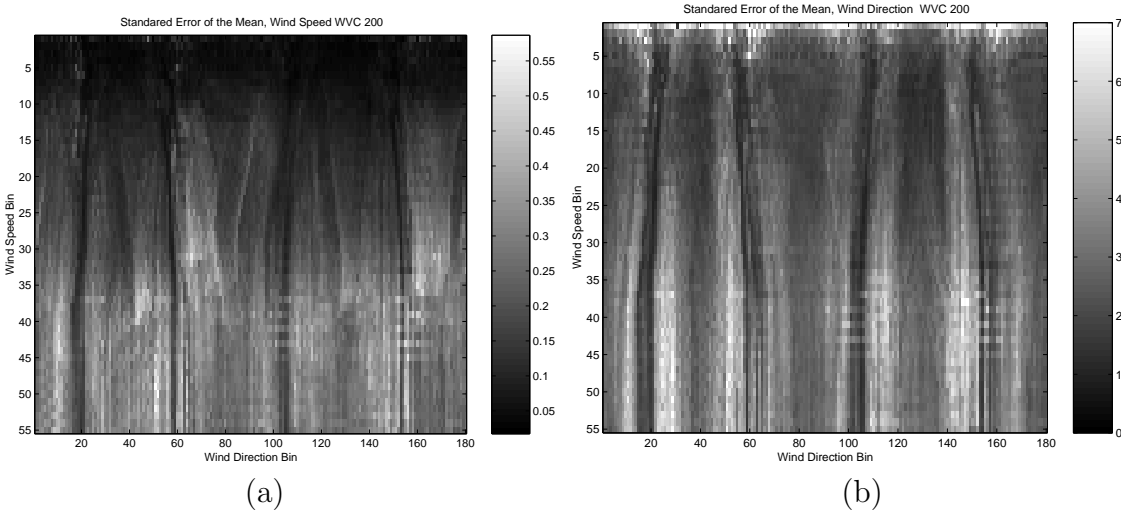


Figure 4.11: (a) Standard error of the mean for each bin in the wind speed bias table (WVC 200). (b) Standard error of the mean for each bin in the wind direction bias table (WVC 200).

each bin is computed and tabulated. The results are shown in Fig. 4.10(b) and (d) for wind speed and wind direction respectively. Examination of these figures reveals substantial improvement in the error.

4.4 Wind Bias Table

Application of this bias adjustment method is most efficiently done concurrently with the wind retrieval processing. This requires that the bias corrections be tabulated into a 3 dimensional table. The three dimensions are cross track location known as wind vector cell (WVC), retrieved wind speed, and retrieved wind direction. The spacing in the WVC dimension is one element for each high resolution wind vector cell (1-760). The spacing in the retrieved wind speed dimension is 0.5 m/s ranging from 3 to 30 m/s, requiring 55 elements. The spacing in the retrieved wind direction dimension is 2° ranging from 0° to 359° , requiring 180 elements. Thus the size of the table is 760x55x180.

To construct this table, two dimensional tables such as those shown in Fig. 4.10 (a) and (c) are made for every 50^{th} wind vector cell. This spacing is subjectively

chosen to give sufficient sampling. Interpolation must be performed for each element in the 2-D wind speed and direction tables to estimate the bias for a particular wind vector cell. The choices for this interpolation include a linear interpolator, a cubic spline interpolator and a polynomial interpolator. The method chosen for this interpolation is the cubic spline interpolator due to its good fit to the data.

A cubic spline is a 3^{rd} order piecewise polynomial which has end points that are equal to the data points it is interpolating. The function and its first and second derivatives are also equal, at the data point, to the next piecewise function at the corresponding data point.

To use cubic spline interpolation we assume that the speed error and direction error can be defined by a discrete function of the wind vector cell number, $f(wvc)$. We want an estimate of the function on the interval $[a, b]$, $\hat{f}(wvc)$. Assuming that sampling the error at every 50th WVC is sufficient to accurately estimate $f(wvc)$ then we know the values of $f(wvc)$ at $wvc = 50, 100, 150, \dots, 750$. Thus the subintervals are given by

$$a = wvc_0 < wvc_1 < wvc_2 < \dots < wvc_{m-1} < wvc_m = b. \quad (4.9)$$

Cubic spline interpolation makes the assumption that $\hat{f}(n)$ is represented by third-order polynomial on the interval between known data points i.e.

$$f_i(n) = a_i + b_i x + c_i x^2 + d_i x^3 \quad 1 \leq i \leq m. \quad (4.10)$$

Given m subintervals, $m + 1$ data points, there are $4m$ unknowns. The $4m$ unknown coefficients are found by applying the definition of the cubic spline. Since $f(wvc)$ must be equal to $f_i(wvc)$ at the end points of the interval we have

$$\hat{f}(a) = f_1(a) = f(a) \quad (4.11)$$

$$\hat{f}(b) = f_m(b) = f(b) \quad (4.12)$$

yielding two conditions. Because $\hat{f}(wvc)$ is continuous at each data point in the interval $[a, b]$, we have

$$\hat{f}(wvc_i) = f_i(wvc_i) = f_{i+1}(wvc_i) = f(wvc_i) \quad (4.13)$$

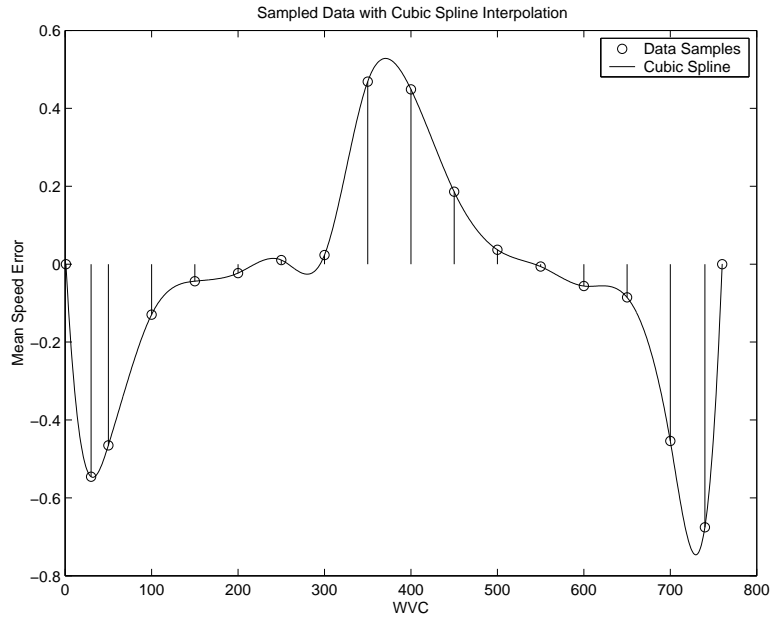


Figure 4.12: Sampled data fitted with cubic spline.

yielding $2m - 2$ conditions. The next $2m - 2$ conditions are due to the fact that the first and second derivatives of $\hat{f}(wvc)$ must exist at each data point on the interior of the interval $[a, b]$, i.e.

$$f'_i(wvc_i) = f'_{i+1}(wvc_i) \quad 1 \leq i \leq m \quad (4.14)$$

$$f''_i(wvc_i) = f''_{i+1}(wvc_i) \quad 1 \leq i \leq m. \quad (4.15)$$

Yielding $4m - 2$ conditions. The final 2 conditions needed to solve for the coefficients can be found by setting the second derivative of $\hat{f}(wvc)$ at end points a and b equal to zero. Cubic spline interpolation is illustrated in Fig 4.12.

4.5 Conclusion

It has been shown in simulations that the bias adjustment method developed in this chapter significantly improves high resolution wind retrieval. In the low resolution wind simulations the method of bias removal was tested by binning the errors in the retrieved wind by the true wind and then again by binning the errors in the

retrieved wind by the retrieved wind vectors. Both methods removed the mean error successfully; however, in practice only the second method of binning the errors by the retrieved wind vector is realizable.

The high resolution winds were then simulated and the method of bias removal was repeated, binning the errors by the retrieved wind vector. This method successfully minimized the bias seen in the simulated wind retrieval. In Figure 4.10 it is clear that the mean error is not exactly zero after bias removal has been performed. This residual bias is a factor of at least two things. The first is computational limitation. Only one hundred realizations of each true wind speed and direction are used. This limits how good the sample mean is at estimating the bias. The second cause of this residual error is the fact that the errors are binned by retrieved wind speed rather than true wind speed. A three dimensional table containing this bias is now being used in the high resolution wind retrieval algorithm to correct the bias.

Chapter 5

High Resolution Ambiguity Removal

5.1 Introduction

One of the problems inherent in wind retrieval using scatterometers is multiple possible solutions, known as ambiguities, are produced for each wind vector cell. This requires a post-estimation step known as ambiguity selection or removal, wherein a single ambiguity is selected at each point. The wind retrieval program used for the research done in this thesis produces at most four ambiguities. Each of the ambiguities are a possible wind vector solution given the σ^0 measurements. It is therefore desirable to develop an efficient method to select the correct ambiguity. Several methods have been developed for the low resolution wind retrieval. Among these is a median filter-based technique. Due to its effectiveness and ease of implementation it is considered in this thesis.

5.2 Initialization of the Ambiguity Selection Algorithm

Median filter based ambiguity selection algorithms require that the wind field be initialized prior to applying the algorithm. Initialization refers to picking one of the ambiguities at each wind vector cell. The method of initialization is critical. If the initial guess is incorrect then no self-contained ambiguity removal algorithm is able to correctly choose the ambiguity closest to the true wind. The high resolution winds have the disadvantage of being much noisier than the corresponding low resolution winds. Therefore methods used to initialize the low resolution wind fields are not useful in the high resolution wind field initialization. Instead initialization of the

high resolution wind field is done using the low resolution wind field. For this reason a description of this method is contained in the next section.

When initializing high resolution ambiguity selection each pixel or wind vector cell in the low resolution wind field maps to 100 pixels or wind vector cells in the high resolution wind field. For each of these 100 wind vector cells in the high resolution wind field the ambiguity closest to the low resolution wind vector is chosen as the initial guess. The method is generally effective since the low resolution wind fields have already had ambiguity selection algorithms applied to them. One problem with this method is that the one pixel or wind vector cell in the low resolution wind covers a area of 25x25 km, if there is a wind front or substantial change in the wind over this area, then many of the high resolution pixels will be initialized with the incorrect ambiguity. Another problem is that when the low resolution wind vector is wrong, it results in 100 wrong wind vectors in the high resolution winds. These problems can be ameliorated to some degree by using a median filter based technique to correct the initial field. The size of the window used in the median filter is important. Larger sizes will clean up errors, such as those caused by the low resolution wind pixel being incorrect, better but the amount of computation time make their use undesirable. The following sections analyze which type of median filter is best for the high resolution winds.

5.3 Ambiguity Selection Method Used in Low Resolution Winds

The low resolution winds reported in the L2B file use a modified median filter technique to select from among the ambiguities in each wind vector cell. The median filter-based technique is described in more detail in later sections. As mentioned previously the wind field must be initialized, i.e. a single initial wind vector chosen at each wind vector cell, in order for the median filter operation to be performed. This initialization process is performed by using the likelihood value reported with each ambiguity from the wind retrieval algorithm. How this likelihood value is computed is explained later. The wind vector ambiguity with the highest likelihood value is chosen as the initialization for each wind vector cell. For instruments with good instrument

skill this initialization is usually the correct choice. The Seawinds instrument has good instrument skill in most sections of the swath. Seawinds instrument skill results in about 60% of the most likely ambiguities being closest to the true wind and around 30% of the second most likely ambiguities being the closest to the true wind. This method of initialization and median filtering in the low resolution winds results in the chosen ambiguity being closest to the true wind 96% of the time [11].

The likelihood estimate of the ambiguity comes from the objective function. The objective function is found from the probability density function of the measured σ^0 . To analyze this value, recall that σ^0 is related to the near surface winds through the geophysical model function,

$$\sigma^0 = \mathcal{M}(U, \chi, \theta, f, pol), \quad (5.1)$$

where U is the wind speed, χ is the relative wind direction, θ is the incidence angle of the radiation, f and pol are the frequency and polarization of the radiation respectively. Estimating the wind from σ^0 involves inverting the model function \mathcal{M} . One problem with this estimation is that noise is introduced in two places. The first type of noise is modeling noise. This noise results from the geophysical model function not being a perfect model for the relationship between the near surface winds and the normalized radar cross section of the ocean, σ^0 . There are several factors that are not accounted for in the model function. These include such things as rain contamination and salinity of the ocean water. These unmodeled factors cause the observed σ^0 to vary from what the model function predicts for given a wind vector. The observed σ^0 can be modeled as

$$\sigma^0 = (1 + K_{pm}\nu)\mathcal{M}(\mathbf{w}) \quad (5.2)$$

where K_{pm}^2 is the variance due to modeling error, ν is a zero mean, unit variance Gaussian random variable, and $\mathcal{M}(\mathbf{w})$ is the geophysical model function evaluated at wind vector \mathbf{w} .

The second type of noise is introduced by the scatterometer instrument when it makes the measurement of σ^0 . This process can be modeled as [12]

$$z = (1 + K_{pc}\nu')\sigma^0 \quad (5.3)$$

where again ν' is a zero mean unit variance Gaussian random variable, K_{pc} is the normalized standard deviation of the measured σ^0 as discussed Chapter 3,

$$K_{pc} = \sqrt{\alpha + \frac{\beta}{\sigma^0} + \frac{\gamma}{(\sigma^0)^2}} \quad (5.4)$$

where α , β , and γ are functions of the A , B , and C coefficients discussed in Chapter 3 given by

$$\alpha = (1 + A)(1 + K_{pr}^2) \quad (5.5)$$

$$\beta = B(1 + K_{pr}^2) \frac{\sigma^0}{SNR} \quad (5.6)$$

$$\gamma = C(1 + K_{pr}^2) \left(\frac{\sigma^0}{SNR} \right)^2. \quad (5.7)$$

In these equation K_{pr} is not well understood and is often set to zero. The random variable z can now be written, combining both types of noise, as

$$z = (1 + K_{pc}\nu)(1 + K_{pm}\nu')\mathcal{M}(\mathbf{w}). \quad (5.8)$$

K_{pm} is not well understood and in most studies is set to zero. However in the wind retrieval algorithm an estimated value is tabulated with the geophysical model function.

The measured σ^0 is modeled as this random variable z . With this noise model the probability density function of z given the wind vector \mathbf{w} can be written as

$$p(z|\mathbf{w}) = \frac{1}{\sqrt{2\pi\zeta}} \exp\left(-\frac{(z - \mathcal{M}(\mathbf{w}))^2}{2\zeta}\right) \quad (5.9)$$

where ζ is the variance and is given by

$$\zeta = \alpha(\sigma^0)^2 + \beta\sigma^0 + \gamma. \quad (5.10)$$

The variance, ζ , is related to K_{pc} by

$$K_{pc}^2 = \frac{\zeta}{(\sigma^0)^2}. \quad (5.11)$$

Estimating the wind vector from the σ^0 of the ocean requires that σ^0 be observed from more than one direction. Generally several σ^0 measurements are used

in the wind estimation process to get a single wind vector. We can determine the joint distribution of these measurements, assuming each measurement is independent, by

$$p(\mathbf{z}|\mathbf{w}) = \prod_{k=1}^K \frac{1}{\sqrt{2\pi\hat{\zeta}_k}} \exp\left(-\frac{(z_k - \mathcal{M}_k(\mathbf{w}))^2}{2\hat{\zeta}_k}\right). \quad (5.12)$$

The maximum likelihood estimate of the wind vector is computed by finding the maximum of the conditional probability density function (pdf), i.e.

$$\hat{\mathbf{w}} = \arg \max_{\mathbf{w}} p(\mathbf{z}|\mathbf{w}). \quad (5.13)$$

From estimation theory we know that this *argmax* operation is that same as minimizing the negative log-likelihood function given by

$$\begin{aligned} \hat{\mathbf{w}} &= \arg \min_{\mathbf{w}} (-\ln(p(\mathbf{z}|\mathbf{w}))) \\ &= \arg \min_{\mathbf{w}} \sum_{k=1}^K \left(\frac{1}{2} \ln(2\pi\hat{\zeta}_k) + \frac{(z_k - \mathcal{M}_k(\mathbf{w}))^2}{2\hat{\zeta}_k} \right). \end{aligned} \quad (5.14)$$

This equation is known as the objective function. The local minima of the objective function correspond to possible solutions to the inverse model function. The likelihood value associate with each ambiguity is calculated from this objective function.

5.4 Median filter ambiguity selection for high resolution winds

5.4.1 Median Filter

A median filter performs a spatial operation on a signal. Median filters are used in image processing to clean up binary noise. They have several benefits over other spatial averaging operations. Among these are edge preservation and resolution preservation [13]. A median filter replaces the input pixel with the median of the pixels surrounding it. The pixels surrounding the input pixel used are determined by the size of the window used to perform the median filter. There are several possibilities for not only the size but also the shape of the window. The simplest of these is a square whose center pixel is the input pixel. In this case the median of all pixels in the window is used as the new value of the center pixel. Figure 5.1 shows several possible sizes of median filters. In the high resolution wind ambiguity removal study, median filters of sizes 3x3, 5x5, 7x7, and 11x11 are analyzed.

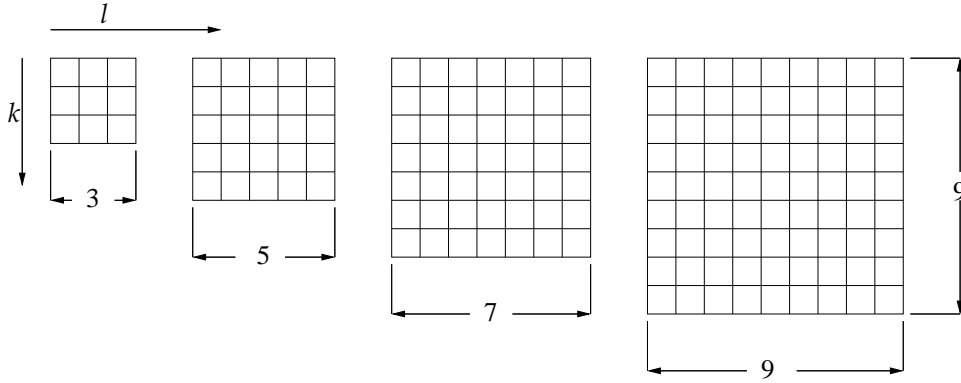


Figure 5.1: Illustration showing the sizes of windows used in testing median filter for use in ambiguity selection

5.4.2 Application of median filter to ambiguity selection

The median filter, as used in image processing, cannot be applied directly to the wind field ambiguity removal since winds are vector quantities. Unlike the image processing median filter, the input pixel is not replaced by the median of the surrounding pixels. Rather, the ambiguity closest to the median is used. Recall that for the high resolution winds there are at most 4 possible choices for the wind vector at each pixel. The median filter is thus used to choose the best of these four possible choices. This is done by calculating the error between each of these ambiguities and the median of the surrounding wind vectors, then setting the input pixel to the ambiguity with the smallest error. Finding the error is not a simple scalar operation. There are two choices for this error metric. The first is to find the wind vector whose direction is closest to that of the median direction. In this case special consideration must be taken to account for the circular nature of the direction. The second choice is to find the wind vector ambiguity that minimizes the norm of the vector difference between the ambiguity and the median of the surrounding wind vectors, i.e.

$$\hat{\mathbf{w}}_{i,j} = \arg \min_k \|\mathbf{w}_{i,j}^k - \mathbf{v}_{i,j}\| \quad (5.15)$$

where $\mathbf{w}_{i,j}^k$ is the k^{th} wind vector ambiguity at wind vector cell (i, j) and $\mathbf{v}_{i,j}$ is the median of the surrounding wind vectors at wind vector cell (i, j) . Another approach

is to choose the ambiguity that minimizes the error with the surrounding wind field. In this case the ambiguity selected at cell (i, j) is given by

$$\hat{\mathbf{w}}_{i,j} = \arg \min_k \sum_{m=i-L}^{i+L} \sum_{n=j-L}^{j+L} \|\mathbf{w}_{i,j}^k - \mathbf{v}_{m,n}\| \quad (5.16)$$

where again $\mathbf{w}_{i,j}^k$ is the k^{th} wind vector ambiguity at wind vector cell (i, j) and $\mathbf{v}_{m,n}$ is the wind vector at cell (m, n) , and L specifies the size of the filter. This filter is analyzed in the following sections.

5.5 Results of median filter

The results of the various median filter sizes used in the high resolution ambiguity selection algorithm are illustrated in Figs. 5.5-5.9. In Fig. 5.5 a 3x3 median filter is used. Several small spots where the L2B initialization selected an ambiguity not spatially consistent are still present. The wind front on the center left side of the image (seen best in the wind direction image) still has the stair step feature caused by the initialization with the low resolution wind. This can be seen by relating Fig. 5.5(b) with Fig. 5.2(b). Thus the 3x3 median filter is too small to correct for the problems caused by the initialization. As previously mentioned one low resolution wind vector cell or pixel in the image maps to one hundred high resolution pixels i.e. a 10x10 high high resolution wind vector cell equals a low resolution cell. With the 3x3 size median filter the edge preserving characteristic of the median filter limits its effectiveness in cleaning up the images. The processing time for the 3x3 median filter is very small compared to the larger size median filter.

In the 5x5 median filter improvements are seen on the wind front. However, the wind directions along the edge of the wind front are still grainy. As in the case of the 3x3 median filter, the 5x5 median filter is not large enough to correct the problems with the initialization.

Increasing the median filter to a 7x7 size window improves the results substantially from the 3x3 median filter. The stair step feature mentioned in the previous paragraph is smoothed and looks much more reasonable. The processing time is increased a small bit from the 3x3 case. The results of the 7x7 median filter are shown

in Fig. 5.6. It should be noted that the median filter size chosen for the low resolution winds processing is a 7x7 median filter [11].

The 11x11 size median filter (results shown in Fig. 5.7) gives the best results; however, they are not substantially better than the 7x7 median filter for the added computation time. It is therefore recommended that the 7x7 size median filter be used as the method for ambiguity removal in the high resolution winds. This choice of median filter size is a subjective choice based on computation time and analysis of the resulting wind field.

In order to take a closer look at what is happening as the size of the median filter is changed, a small region with relatively high wind speed is selected. The region selected for this investigation is shown in Fig. 5.8(a). The low and high resolution winds are shown in Figs. 5.8 (b) and (c) respectively. Since the region selected spans parts of three low resolution wind cells in the cross track direction the wind vectors for each of these cells is shown. In the high resolution wind field (shown in Fig. 5.8(c)) the edges of the low resolution cells are apparent.

Application of the high resolution ambiguity selection algorithm to the region with the four sizes of median filters is illustrated in Fig. 5.9. The 3x3 and 5x5 median filters fix some of the wind vectors but in both wind fields there is an obvious line of wind divergence. Increasing the median filter to a 7x7 median filter removes the area in the middle of the region that is apparently incorrect. There is no apparent change in the wind field when the median filter is increased to an 11x11 size median filter. Therefore due to this and the added computation time there is no advantage to using the 11x11 median filter.

After median filtering there still exists some features that may not represent the true wind flow. Figure 5.10 highlights one such feature. All of the ambiguities in this region are examined. In Fig. 5.11 the wind vectors are overlaid on a background whose color represents the wind speed (a) and wind direction (b). We can see that the wind field in the region around this area has an easterly flow, which flows against the selected ambiguities in this small area. To examine if this is a problem with the ambiguity selection algorithm or if this is indeed the best choice given the ambiguities

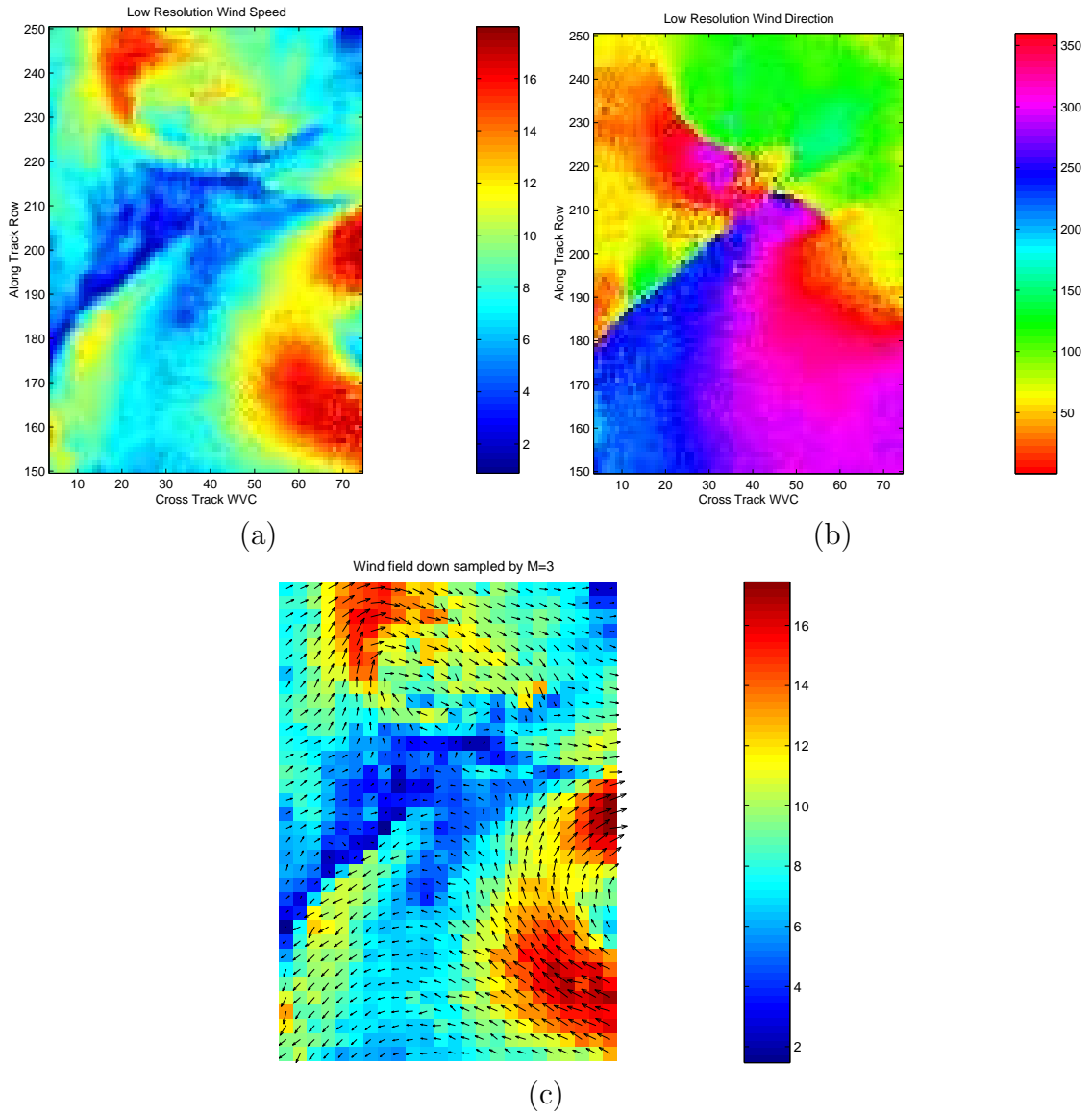


Figure 5.2: Low resolution (a) wind speed and (b) direction in study area.(c) Down-sampled low resolution wind field to show wind flow with arrows, background color represents the wind speed.

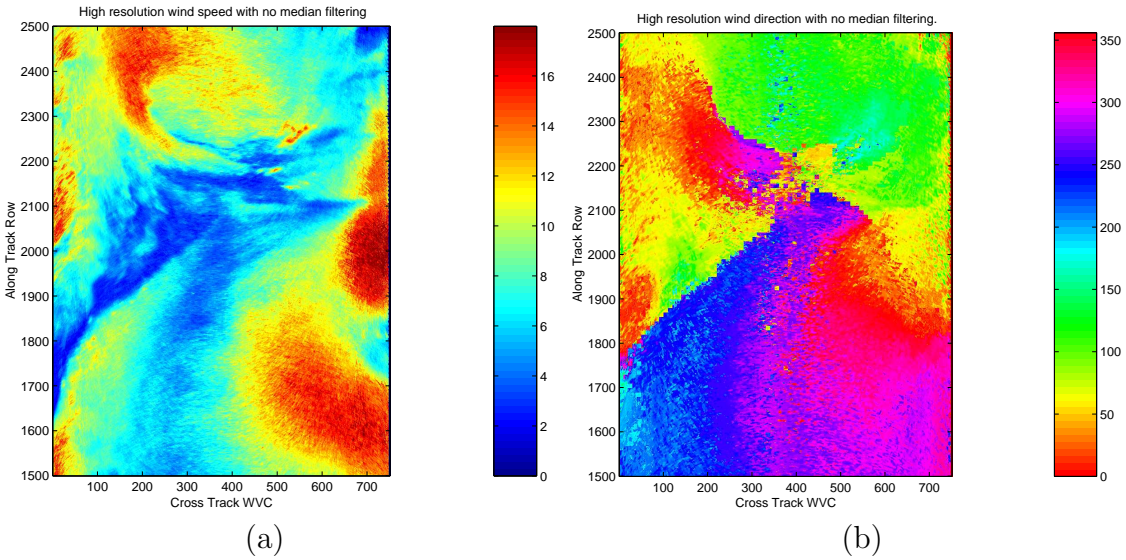


Figure 5.3: High resolution (a) wind speed and (b) wind direction in study area. Wind ambiguity selection is performed by choosing the ambiguity closest to the low resolution wind vector in Figure 5.2

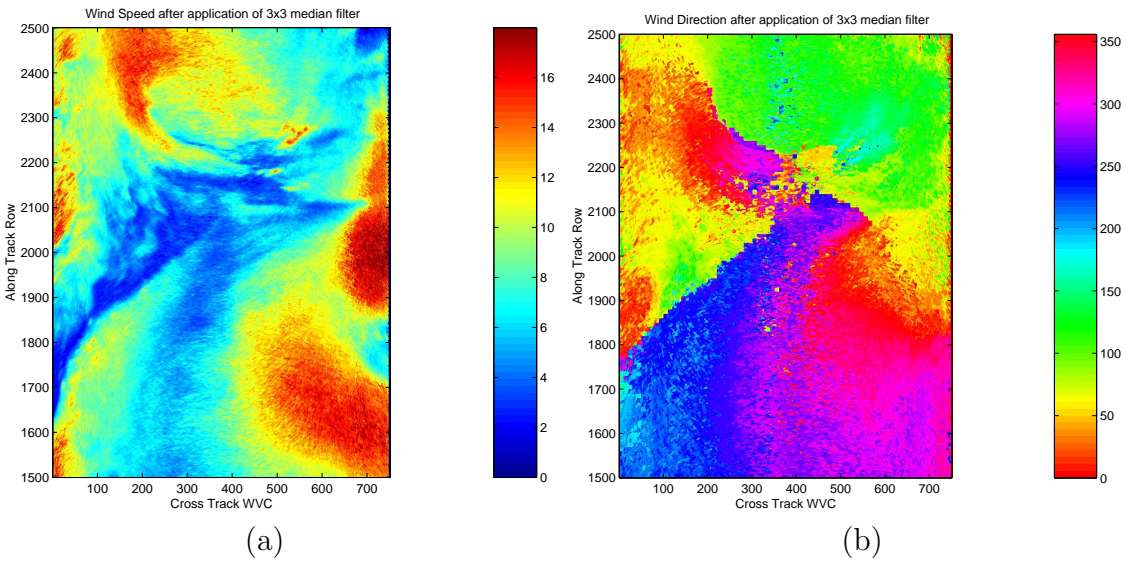


Figure 5.4: High resolution (a) wind speed and (b) wind direction after ambiguity selection with 3x3 median filter is performed

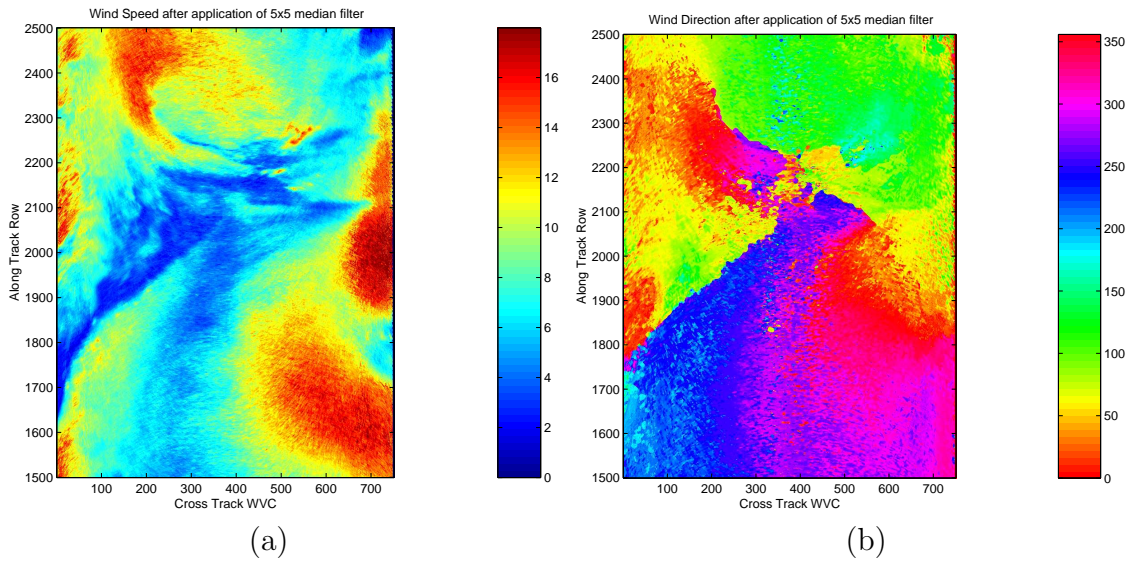


Figure 5.5: High resolution (a) wind speed and (b) wind direction after ambiguity selection with 5x5 median filter is performed

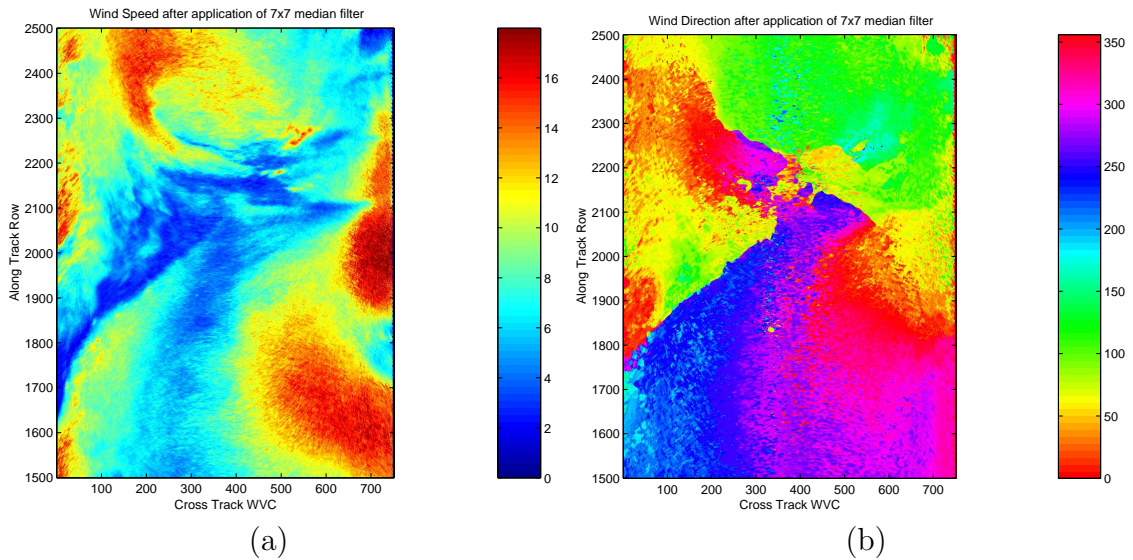


Figure 5.6: High resolution (a) wind speed and (b) wind direction after ambiguity selection with 7x7 median filter is performed

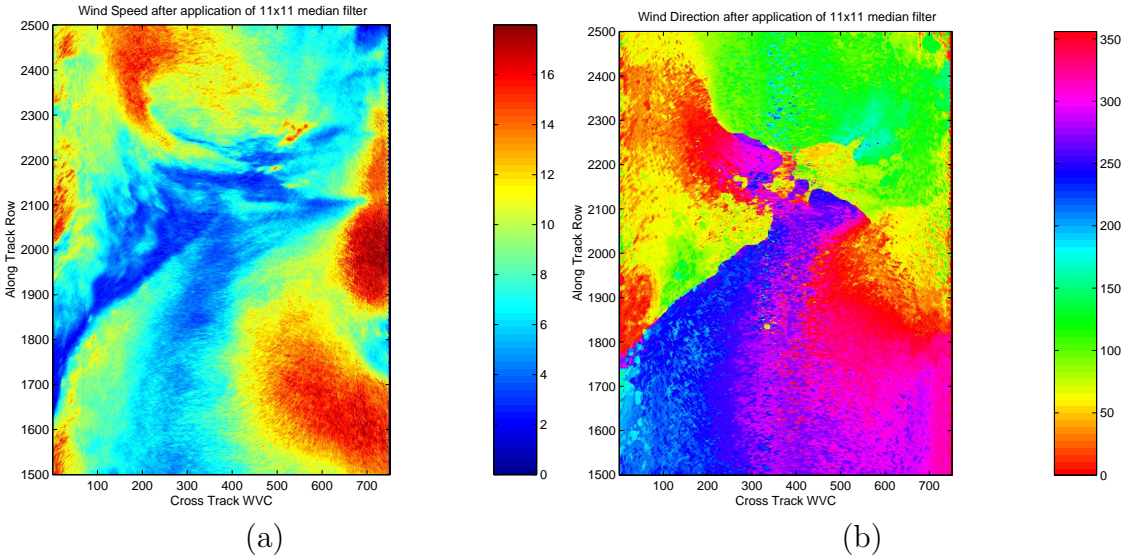


Figure 5.7: High resolution (a) wind speed and (b) wind direction after ambiguity selection with 11x11 median filter is performed.

at each pixel we look at each of the four ambiguities for this small region. These ambiguities are illustrated in Fig. 5.12. Examination of Fig. 5.12(a) shows that on the left edge of this area there exists cells with only one ambiguity. This causes ambiguity selection errors seen in the area since the ambiguity at these cells has an inconsistent direction, thus causing inconsistent wind directions in the surrounding cells. It should be noted that this feature occurs in the nadir part of the swath. Wind estimates in this region of the swath are noisier than are wind estimates at other locations across the swath.

5.6 Comparison of Low Resolution and High Resolution Wind Distribution

To examine the overall accuracy of the high resolution winds, the distribution of the wind vectors contained in the high resolution wind field is compared to the distribution of wind vectors contained in the low resolution wind field. To do this the low resolution winds are upsampled to yield the same sampling as the corresponding high resolution winds. This comparison is illustrated in Fig. 5.13.

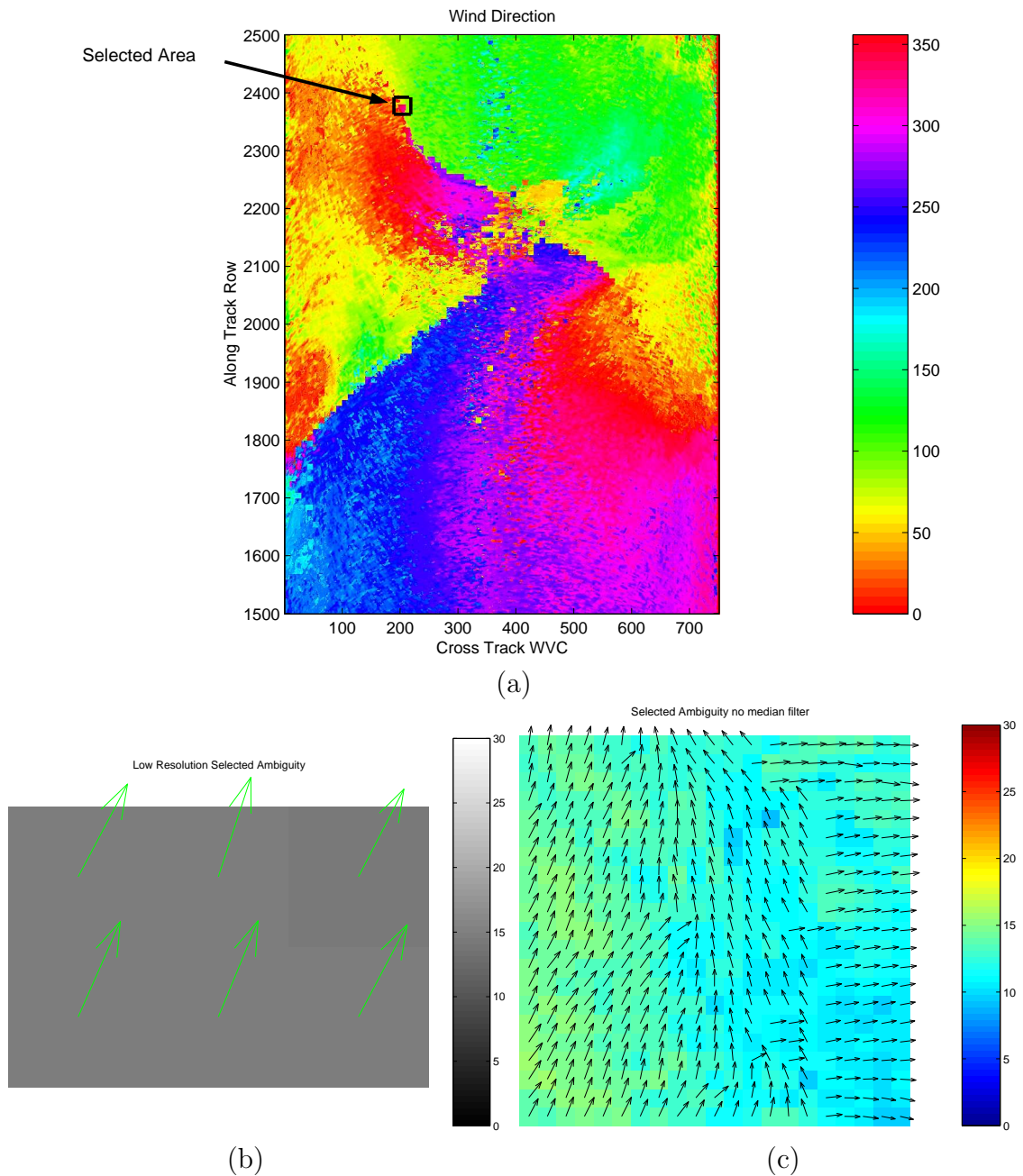


Figure 5.8: (a) Illustration of small region selected to show results of median filter. (b) Low resolution winds in selected region. The region selected includes half of the left low resolution wind cell and half of the right low resolution wind cell, both wind cells are therefore included in the plot. (c) High resolution wind before median filtering is done. The ambiguities selected here are the closest in direction to the low resolution wind vectors shown in (b).

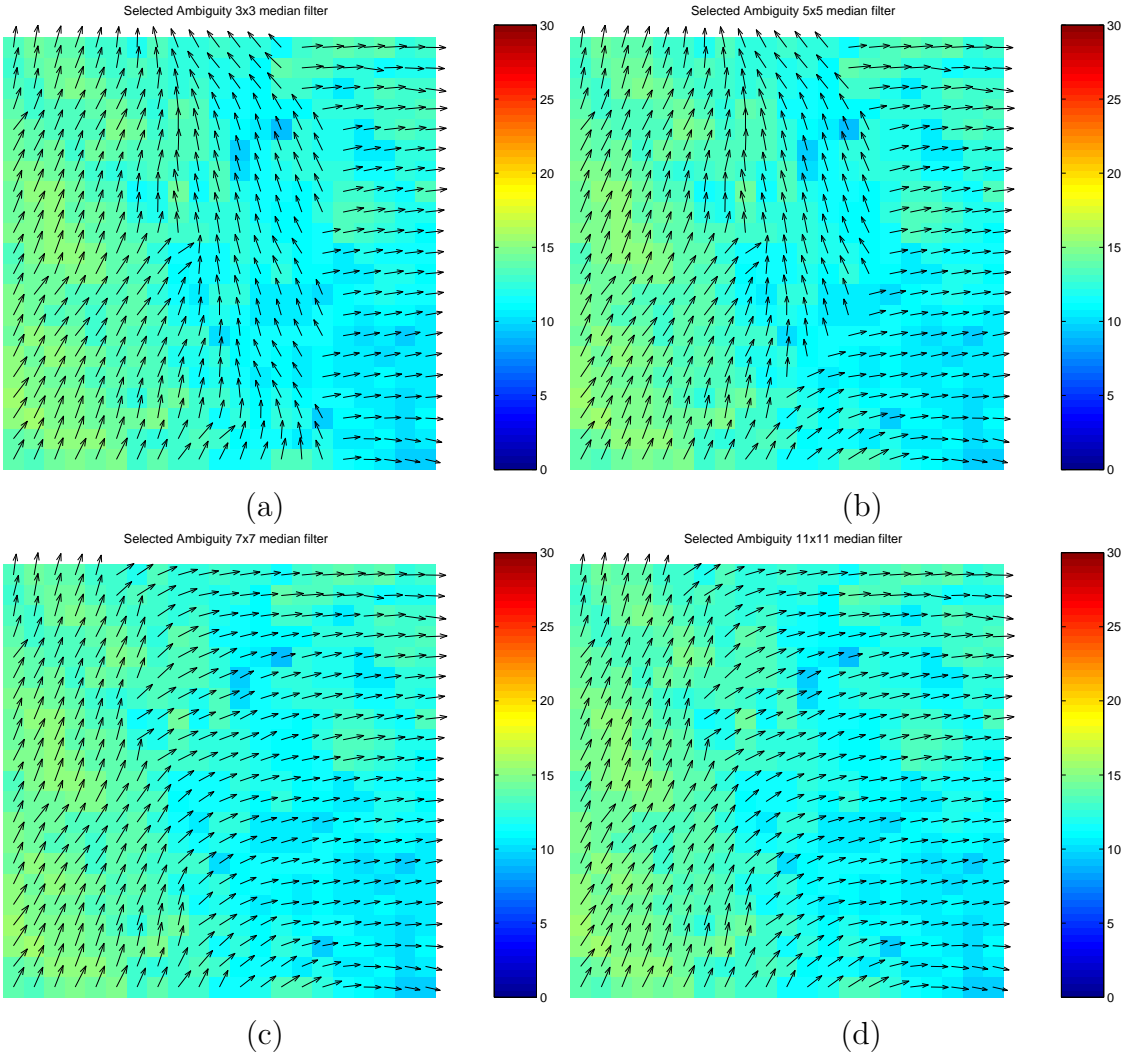


Figure 5.9: Results of 4 sizes of median filter in high resolution ambiguity removal algorithm. (a) 3x3 (b) 5x5 (c) 7x7 (d) 11x11

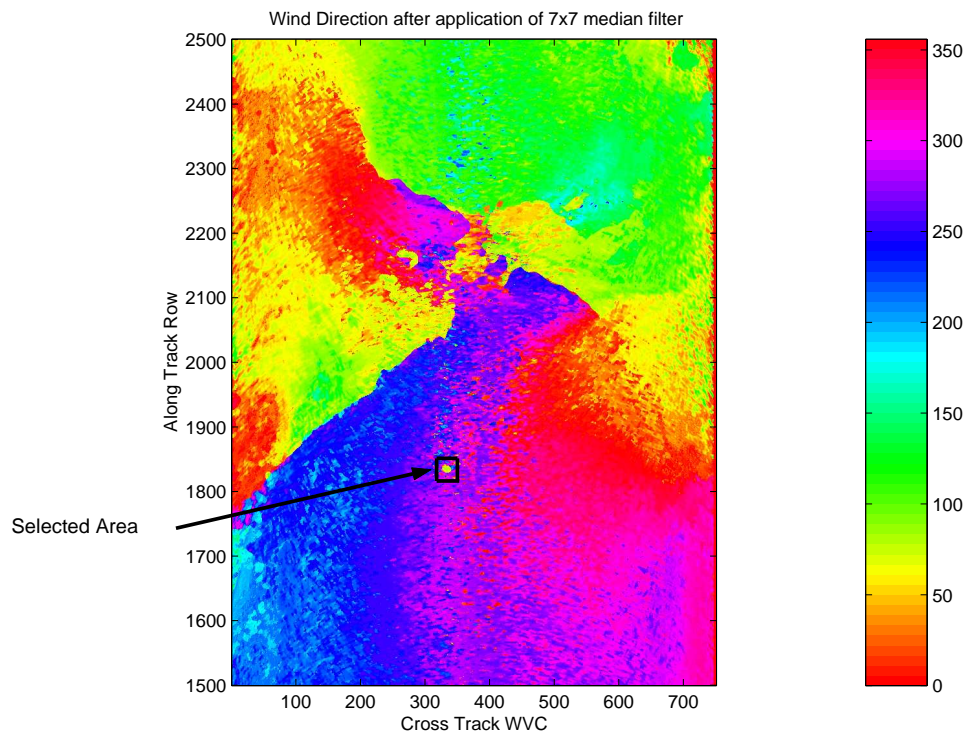


Figure 5.10: Illustration Showing region selected.

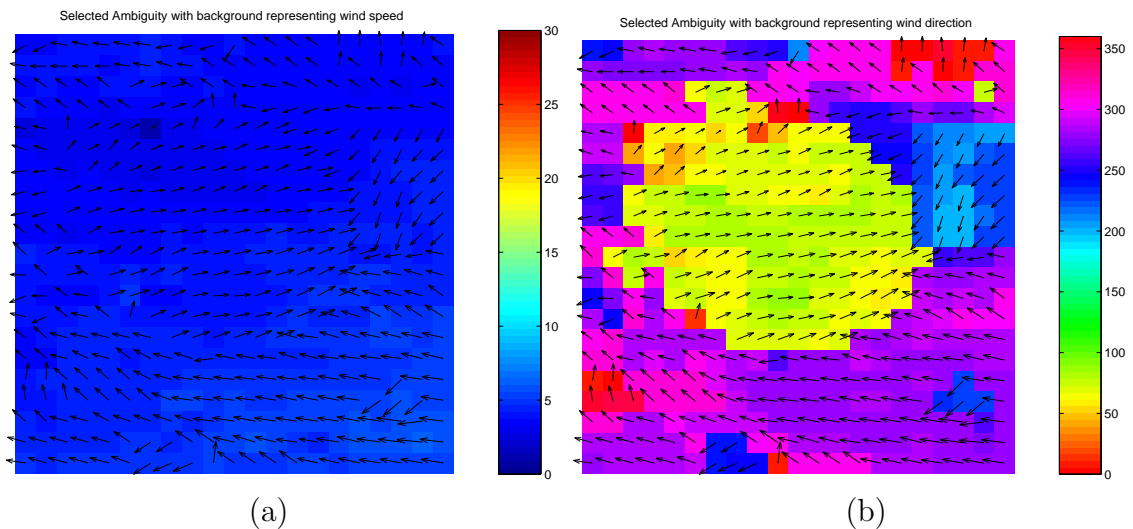


Figure 5.11: Illustration showing high resolution selected ambiguity in region. (a) Selected ambiguities shown with background color representing the wind speed. (b) Selected ambiguities shown with background color representing wind direction.

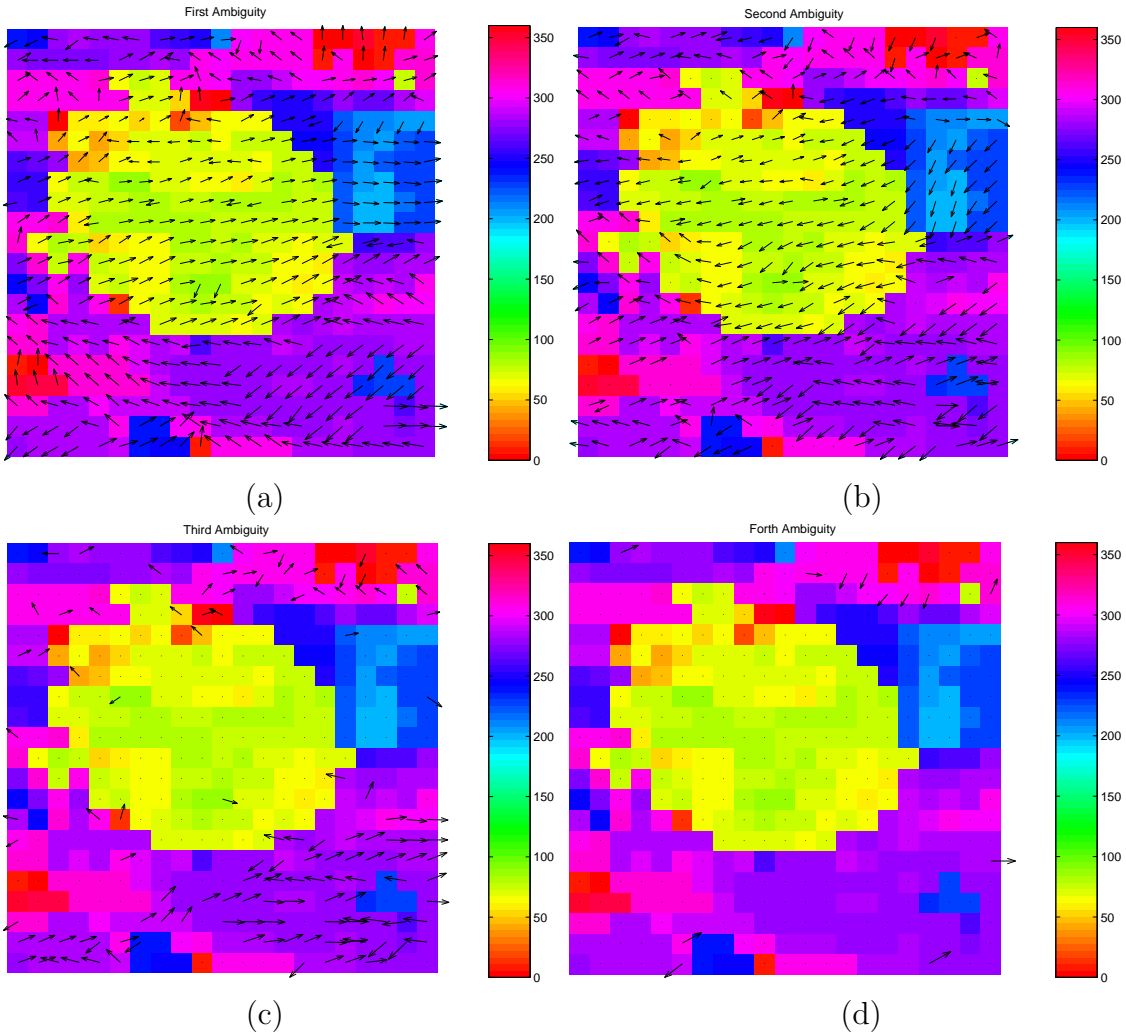


Figure 5.12: Illustration of the four ambiguities at each pixel in the selected region. The background color in each image corresponds to the wind direction. (a) The first ambiguities for each pixel. (b) The second ambiguities for each pixel. (c) The third ambiguities for each pixel. (d) The fourth ambiguities for each pixel.

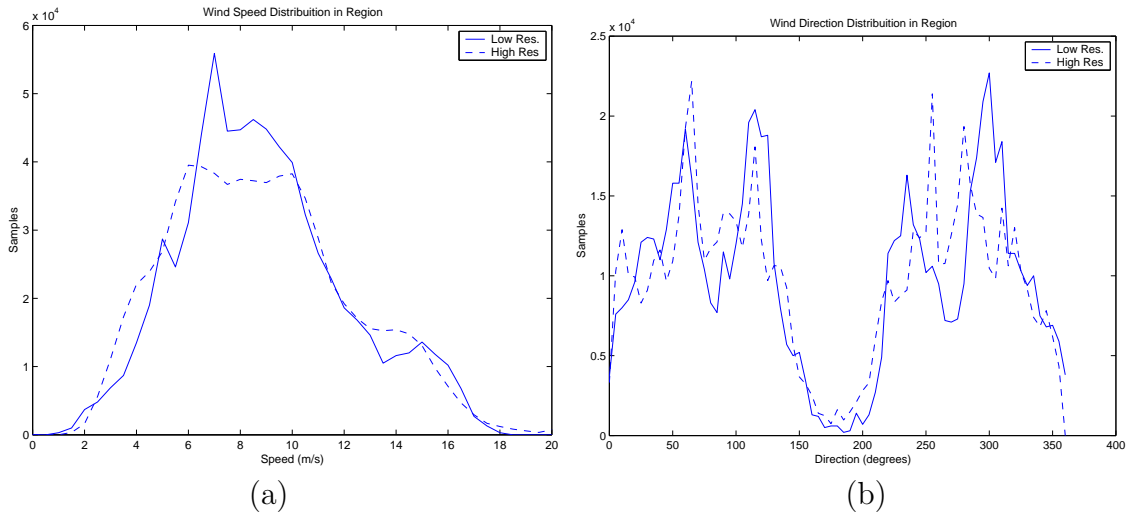


Figure 5.13: Distribution of (a) wind speeds and (b) wind directions in region illustrated in Fig. 5.6.

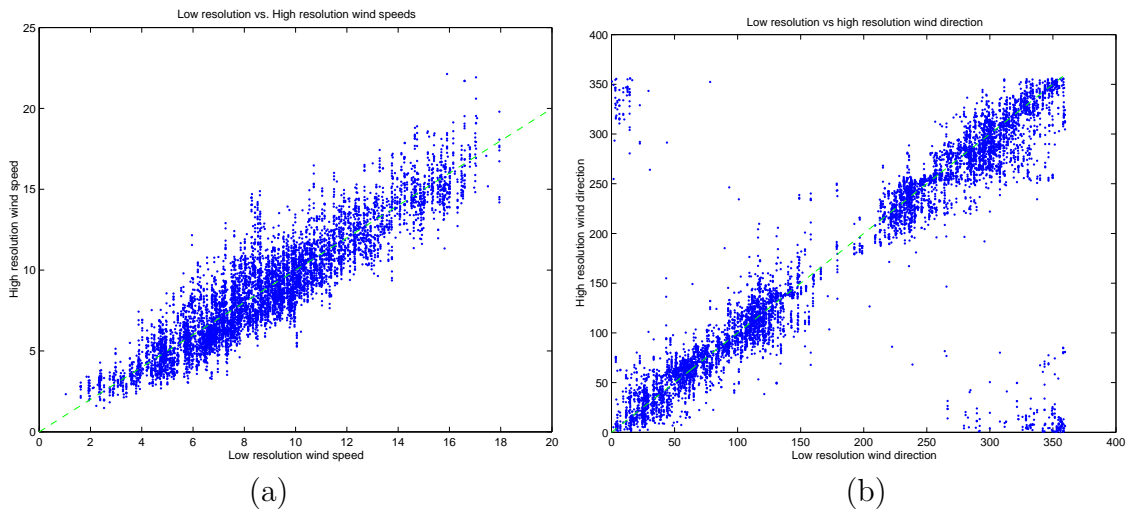


Figure 5.14: Low resolution wind vs high resolution wind in wind field.

The distribution of the high resolution wind speed follows that of the low resolution wind speed nicely for most of the range of wind speeds. The distribution of the wind direction shows that in both the high resolution and low resolution cases there exist peaks in the distribution: one centered at about 90° and one centered at about 270° . The high resolution winds are noisier than the corresponding low resolution winds. This is especially evident in the nadir track (center of the swath) where the four measurements (two forward and two aft) are taken at azimuth angles 180 degrees apart.

Scatter plots of the high resolution wind speed and direction vs the low resolution wind speed and direction are also provided to illustrate the relationship between the two, see Fig. 5.14. For every low resolution wind vector cell there are one hundred high resolution wind vector cells. In Figure 5.14(a) the wind speed relationship between the low and high resolution winds is shown. The low resolution wind cell is in effect an average of the high resolution winds in that 25x25 km cell. The scatter-plots shown in Figure 5.14 are generated without performing bias correction on the wind data.

5.7 Conclusion

Although other ambiguity removal algorithms may be more accurate, the limiting factor in high resolution wind ambiguity removal is the amount of data contained in each revolution of the QuikSCAT satellite. In the low resolution case an entire revolution worth of wind data can be stored in memory at one time. The high resolution wind algorithm increases that data by a factor of 100. It is therefore imperative that an efficient algorithm be used. Choosing the best ambiguity selection method is subjective since we do not know what the true wind speed and direction are at each WVC, which would allow us to calculate the error and chose the method that minimizes the error. We therefore must base our choice of ambiguity selection on a subjective analysis of the resulting wind field. The wind field analyzed in this chapter had the best results, excluding the nadir region of the swath, with the 7x7 median filter. For this size the graininess of the initialization was removed with out

substantially increasing the processing time. Based on this subjective analysis the recommended size of the median filter for the ambiguity selection algorithm is the 7x7 square filter.

Chapter 6

Conclusion

The high resolution wind retrieval algorithm presented in this thesis has the potential of becoming a widely used tool in the scientific community. Several applications for the high resolution wind fields have been suggested. One such application is hurricane monitoring [14],[7]. The high resolution winds allow significant small-scale wind features to be resolved therefore making it a useful tool. The methods presented in this thesis increase the usefulness of the high resolution wind fields by improving the accuracy of the estimated winds.

6.1 Summary of Contributions

This thesis presents the development and results of three portions of a high resolution wind retrieval algorithm. The high resolution wind retrieval algorithm will increase the usefulness of the SeaWinds data being produced by JPL. The algorithms and methods developed in this thesis are being applied to data from the SeaWinds instrument on the QuikSCAT satellite but may also be used on data from the SeaWinds instrument recently placed in orbit aboard the ADEOSII satellite.

The contributions of this thesis span each area of the wind retrieval processing. The first contribution deals with the pre-processing of data used in the wind retrieval algorithm. The second contribution is applied during the processing of the wind data. The third contribution addresses the issue of ambiguity removal done in post-processing. Each of these contributions is summarized in greater detail in the following sections.

6.1.1 Kp Compositing Methods

One of the key factors in increasing the resolution of the wind fields produced using SeaWinds data is accurately compositing the parameters used in the wind retrieval algorithm. The parameters addressed in this thesis are σ^0 and K_p . Two methods for compositing slice K_p values are derived. The first method uses the actual value of K_p for slices to compute the composite K_p . The second method does the compositing first on the variables used to compute K_p then uses these values to compute the composite K_p . A summary of these methods is given at the end of Chapter 3.

One step in the derivation of the method for compositing K_p required that a method for compositing σ_0 be used. The method used to composite σ_0 in the K_p compositing is shown in Chapter 3. One other method for the σ^0 compositing and a comparison of the two σ^0 compositing methods is discussed in Appendix B. These compositing methods are used in a pre-processing step prior to the processing the high resolution wind fields.

6.1.2 Bias Removal Tables

The second contribution of this thesis is the development and compilation of the wind bias tables. These tables are three dimensional tables where the dimensions of the tables correspond to retrieved wind speed, retrieved wind direction, and across track location (WVC). Two tables are created, one for wind speed bias and one for wind direction bias, to be used in the high resolution wind processing. The bias adjustments are made after estimating the wind and applied at the time of processing to each wind vector. The bias removal method was tested in simulations and showed substantial improvements in the errors observed.

6.1.3 Ambiguity Selection

The third contribution made by this thesis is the application of a median filter based ambiguity selection algorithm to the high resolution wind fields. The σ^0 data used to process the high resolution wind fields is substantially more noisy than is

the σ^0 data used in the low resolution wind processing. The high resolution wind fields are therefore more noisy than the corresponding low resolution wind fields. The median filter based ambiguity selection algorithm was found to work reasonable well for the high resolution wind field. Several sizes of this median filter based technique are examined. The 7x7 median filter proved to give the best results with minimum processing time.

6.1.4 Future Research

Ambiguity removal for scatterometer data has been the topic of several studies. The huge amount of data produced by the high resolution wind retrieval algorithm complicates ambiguity removal. Other factors introduced by the high resolution wind fields that limit the ambiguity selection algorithms which can be used are first the increased noise and second the loss of instrument skill. Developing improved ambiguity removal algorithms that ameliorate these limitations would be a substantial contribution to the high resolution wind retrieval algorithm.

Another key contribution would be the development of a ambiguity selection algorithm that did not require the use of the low resolution wind file (L2B) to initialize the wind field. This could possibly be done by applying a field-wise wind retrieval algorithm to the high resolution winds.

Appendix A

Code Performance Comparisons

A.1 Introduction

While investigating the results of retrieving wind from SeaWinds egg measurements and composite slice measurements we found we could not obtain the same wind measurements reported in the L2B data product, even using the JPL code. Several attempts were made using σ_0 and other relevant data from both the L1B data product and the L2A data product. These attempts included using both the MGDR wind retrieval program and the Science wind retrieval program. The data in the L1B and L2A data products are organized differently, therefore cross referencing files known as “Key files” are used to extract the same pulses from both files which fall into the wind vector cell of interest.

A wind vector cell (WVC) is a 25 kilometer square. The SeaWinds data is organized into a grid of WVCs. SeaWinds has a swath width of about 1,800 kilometers and therefore has 72 WVC per row. There are two extra WVC on each end of the swath to account for occasional outliers. The σ_0 values which are located in this WVC are used in the wind retrieval program. The process of retrieving wind is outlined in the following sections. For each case mentioned above the wind estimates are calculated and then compared to what is reported by JPL in the L2B data product.

A.2 L1B Data Product

The L1B data product contains data for one revolution of the satellite. The data is time ordered i.e. sequentially listed for each scatterometer pulse, alternating

between inner and outer beam. Each frame contains 100 pulses. For each pulse of data contained in the wind vector cell (WVC) of interest, i.e. for each WVC in the L2B data product, several variables are extracted. These include σ_0 , the incidence angle, and the azimuth angle of each measurement. To retrieve the wind the variance coefficients must also be calculated. These coefficients are α , β , and γ . They are not explicitly listed in the L1B data product but they are functions of the Kpc coefficients which are listed. These coefficients are Kpc_a, Kpc_b, and Kpc_c or A, B, and C respectively. They are used in the following equations to calculate α , β , and γ ,

$$\alpha = (1 + A) \cdot (1 + K_{pr}^2) \cdot (1 + K_{pm}^2) - 1, \quad (\text{A.1})$$

$$\beta = B \cdot (1 + K_{pr}^2) \cdot \frac{\sigma_0}{SNR}, \quad (\text{A.2})$$

$$\gamma = C \cdot (1 + K_{pr}^2) \cdot \left(\frac{\sigma_0}{SNR}\right)^2, \quad (\text{A.3})$$

where K_{pm} is the variance of the σ_0 due to the model function uncertainties. REF [15] reports that these values are assumed to vary from measurement to measurement. K_{pr} is the standard deviation of σ_0 due to calibration uncertainty. K_{pr} is read from a table. Its value depends on the azimuth angle and the beam number¹ of the pulse. The SNR is also extracted from the L1B file.

Part of the reason for using the L1B data in this study is to determine if the problem is round off error introduced when the data is written to the L2A file. By computing α , β , and γ from the Kp coefficients it is hoped that this round off error, if it exists, is eliminated.

A.3 L2A Data Product

The L2A data product is spatially ordered. The scatterometer pulses are grouped into rows and columns of Wind Vector Cells (WVC). This organization is the same as in the L2B where, for each WVC, the wind estimates are listed. For this reason, when comparing the wind estimates reported in the L2B file with those we

¹The Beam number is assigned to each pulse at the time the data is extracted from the L1B or L2A data files. Beam 1 is assumed to be forward looking inner beam. Beam 2 is forward looking outer beam. Beam 3 is aft looking inner beam. Beam 4 is aft looking outer beam.

get from using the data from the L2A and L1B files, we must first look at the L2A file to determine which scatterometer measurements are found in the WVC.

It should be noted that the L2A file contains 39 rows at the beginning and ending of the rev from the previous and next revs, respectively. This offsets it's rows from the L2B file. By using the variable `wvc_row` problems with this offset can be avoided.

We can use the pulses directly if we are using the L2A data or we use the KEYS cross-referencing file to find each pulse in the L1B file. The KEYS cross-referencing file contains which frame and pulse number in the L1B file that the pulse from a given row and column of the L2A file is located. To retrieve the wind using the L2A file we need the σ_0 value, and the incidence and azimuth angles of each pulse. The L2A file also has listed for each pulse modified variance coefficients α' , β' , and γ' which are,

$$\alpha' = \frac{1 + \alpha}{1 + K_{pm}^2} = (1 + A) \cdot (1 + K_{pr}^2), \quad (\text{A.4})$$

$$\beta' = \beta, \quad (\text{A.5})$$

$$\gamma' = \gamma. \quad (\text{A.6})$$

It is unknown whether these coefficients are used modified or unmodified (α' or α) in the L2B processing. Both cases are tested in this study.

A.4 Wind Retrieval Program

The official JPL wind retrieval program requires several input parameters which are used in the evaluation of the inverse geophysical model function, to estimate the wind vectors. Two version of this program are compared in this report: MGDR and Science processing. Both programs use the same input parameters with the execption of an array containing the number each type of beam contained in the WVC which is used by the MGDR program. The following is a list of the input parameters used.

<code>wr_count</code>	number of measurements to be used
<code>wr_cell_incidence</code>	array of incidence angles for each measurement

<code>wr_cell_azimuth</code>	array of azimuth angles for each measurement
<code>wr_sigma0</code>	array of sigma0 measurements in linear space
<code>wr_kp_alpha</code>	array of alpha coeff.
<code>wr_kp_beta</code>	array of beta coeff.
<code>wr_kp_gamma</code>	array of gamma coeff.

The output variables returned from the wind retrieval code are:

<code>wr_num_ambigs</code>	number of wind vector abiguities
<code>wr_mle</code>	array of mle values
<code>wr_wind_speed</code>	array of wind speeds
<code>wr_wind_dir</code>	array of wind directions
<code>wr_wind_speed_err</code>	
<code>wr_wind_dir_err</code>	

Each of the arrays of output variables are of length `wr_num_ambigs`. The output of the two wind retrieval programs differ by 180°. This can be accounted for by using,

$$Direction_{new} = mod(Direction_{old} + 180.0, 360.0). \quad (A.7)$$

A.5 Results

For every wind vector cell there are one to six wind estimate abiguities returned from the wind retrieval program. There are at most 4 reported in the L2B data product. Each ambiguity has with associated it a MLE value computed using the σ_0 , incidence angle, azimuth angle, polariztion and model function. The ambiguities are listed in descending likelihood order. Two methods are used to compare the wind estimates we computed with those reported in the L2B data product. First, we compare all the ambiguities and average the error over all cases. This introduces a few problems because of the ordering of the ambiguities. Often ambiguities that are obviously the closest to each other are compared with others because the MLE values which we computed are not in the same order as those that the L2B data product had listed. Therefore extra error is introduced into the average. The second method

used is to take the ambiguity which is closest to the selected ambiguity in the L2B file. This method eliminates the need to check for ambiguity reordering do to the MLE value.

A.5.1 L1B data

Modified Variance Coefficients

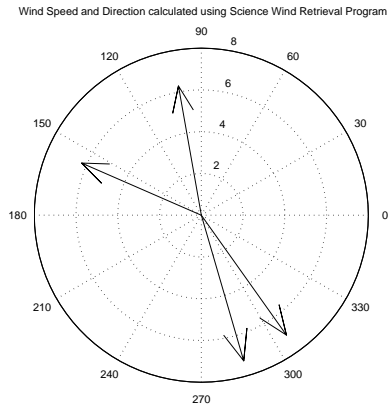


Figure A.1: Wind estimates calculated using L1B data to calculate α' , β' , and γ' in the Science wind retrieval code, for rev 12950 row 314 wvc 18. See Table A.1

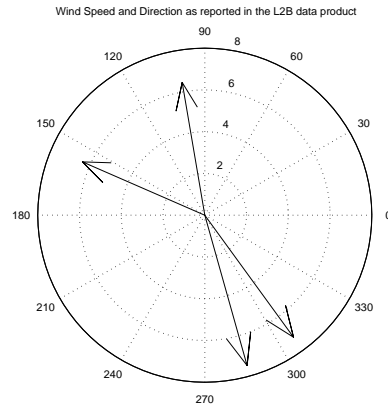


Figure A.2: Wind estimates reported in the L2B data file for rev 12950 row 314 WVC 18. See Table A.1

Table A.1: Wind Speed, Direction and MLE for rev 12950 row 314 wvc 18. L1B wind estimates calculated using α' , β' , and γ' unmodified.

L1B			L2B		
Speed	Direction	MLE	Speed	Direction	MLE
7.04	305.39	-1.380971	7.23	306.04	-0.1160
7.27	286.25	-3.081374	7.48	285.71	-0.2840
6.25	156.48	-9.316661	6.39	156.45	-0.7680
6.29	100.05	-14.93509	6.45	99.65	-1.4200

By “modified variance coefficients” we are referring to α' , β' , and γ' which are found in the L2A file. In this case we are using data from the L1B file and applying equations (4), (5), and (6) with the exception that K_{pr} is set to zero. This test was inspired by the fact that only in this case were we able to match α' , β' , and γ' found in the L2A file with the data in the L1B file using these equations.

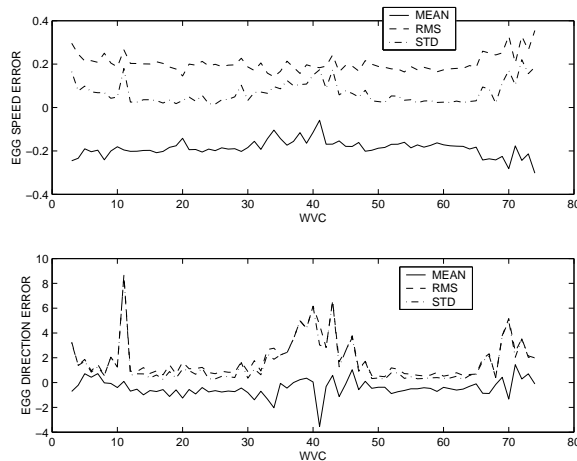


Figure A.3: Wind estimate error averaged over row 311 through 321 of rev 12950 for all wind vector cells. The wind estimates were calculated using α' , β' , and γ' from L1B data.

Table A.2 compares the α' , β' , and γ' coefficients. The data in the table corresponding to the L2A file was extracted and listed directly. The data in the table corresponding to the L1B data, α' , β' , and γ' , were computed from the L1B data as mentioned above. With the exception of some rounding differences for a few pulses the data matches exactly. The L2A data appears to have been rounded to three significant figures for α' , two significant figures for β' , and four significant figures for γ' . It is hoped that by using the L1B data to retrieve the winds, instead of L2A data, that we can more closely match the L2B data.

Table A.2: The L2A α' , β' , and γ' are extracted directly from the L2A data file. The L1B α' , β' , and γ' are calculated using data from the L1B file and equations (4), (5), and (6). The data is extracted from rev 12950 row 314 WVC 18. χ is the azimuth angle of the pulse. θ is the incidence angle of the pulse.

χ	θ	α'		β'		γ'		σ_0	
		L1B	L2A	L1B	L2A	L1B	L2A	L1B	L2A
54.1	315.48	1.0106	1.011	1.8715e-05	1.87e-05	1.0994e-08	1.0997e-08	-19.39	-19.39
46.3	304.62	1.0110	1.011	2.5774e-05	2.58e-05	2.0852e-08	2.0858e-08	-24.06	-24.06
54.1	314.30	1.0106	1.011	1.8888e-05	1.89e-05	1.1198e-08	1.1201e-08	-20.17	-20.17
54.1	202.76	1.0117	1.012	1.7708e-05	1.77e-05	9.8435e-09	9.8462e-09	-24.76	-24.76
46.3	214.69	1.0133	1.014	2.3291e-05	2.33e-05	1.7027e-08	1.7032e-08	-26.25	-26.25
46.3	302.23	1.0110	1.011	2.7238e-05	2.72e-05	2.3289e-08	2.3295e-08	-24.18	-24.18
46.3	304.55	1.0110	1.011	2.5774e-05	2.58e-05	2.0852e-08	2.0858e-08	-23.86	-23.86
46.3	215.96	1.0132	1.013	2.3237e-05	2.32e-05	1.6949e-08	1.6954e-08	-26.67	-26.67
46.3	303.42	1.0110	1.011	2.5479e-05	2.55e-05	2.0377e-08	2.0383e-08	-23.34	-23.34
46.3	213.49	1.0134	1.014	2.3237e-05	2.32e-05	1.6949e-08	1.6954e-08	-26.27	-26.27
54.1	203.97	1.0117	1.012	1.6565e-05	1.66e-05	8.6129e-09	8.6153e-09	-24.26	-24.26
46.3	302.29	1.0110	1.011	2.542e-05	2.54e-05	2.0284e-08	2.0289e-08	-23.81	-23.81

Unmodified Variance Coefficients

It is not clear if α' , β' , and γ' (Equations (4), (5), and (6)) were used for the L2B product or if α , β , and γ (Equations (1), (2), and (3)) were used. To use α , β , and γ , Kpm must be included. It is assumed that the value of Kpm is 0.7 dB. Kpm is converted to linear space before it is applied in equation (1). For this test K_{pr} is set to zero.

Comparing Tables [A.3] and [A.1] reveals a substantial improvement in the MLE value, but not much improvement in the direction and even less in the speed.

Table A.3: Wind Speed, Direction and MLE for rev 12950 row 314 wvc 18. L1B wind estimates calculated using α , β , and γ .

L1B			L2B		
Speed	Direction	MLE	Speed	Direction	MLE
7.05	305.28	-0.1316985	7.23	306.04	-0.1160
7.26	286.39	-0.3029400	7.48	285.71	-0.2840
6.28	158.08	-0.9124814	6.39	156.45	-0.7680
6.28	99.81	-1.407623	6.45	99.65	-1.4200

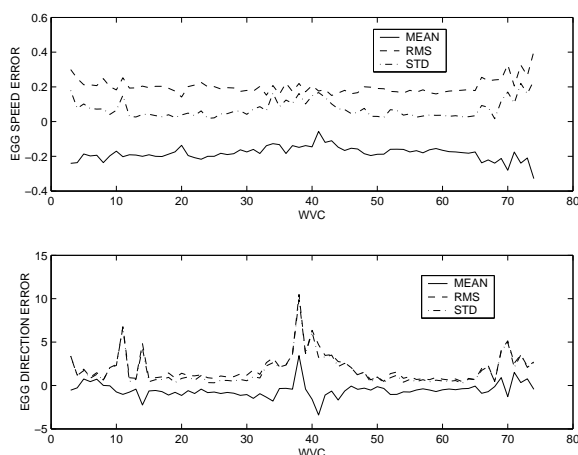


Figure A.4: Wind estimate error averaged over row 311 through 321 for all wind vector cells. The wind estimates were calculated using α , β , and γ from L1B data.

Modified Variance Coefficients With K_{pr}

K_{pr} is the standard deviation of σ_0 due to calibration uncertainty. It is not stored in either the L1B or L2A data products. The value of K_{pr} is extracted from the table QS_KPRP0001. The value of K_{pr} depends on the azimuth angle and the beam number of the pulse. For this test K_{pr} was included when α' , β' , and γ' were computed. This test shows very minimal improvement in the MLE value and almost no improvement in the direction and speed when compared to the test with K_{pr} set to zero.

Table A.4: Wind Speed, Direction and MLE for rev 12950 row 314 wvc 18. Wind estimates calculated using L1B data to calculate α' , β' , and γ' . K_{pr} is read in from a table.

L1B			L2B		
Speed	Direction	MLE	Speed	Direction	MLE
7.04	305.38	-1.232904	7.23	306.04	-0.1160
7.27	286.26	-2.760932	7.48	285.71	-0.2840
6.26	156.67	-8.359354	6.39	156.45	-0.7680
6.29	100.02	-13.32042	6.45	99.65	-1.4200

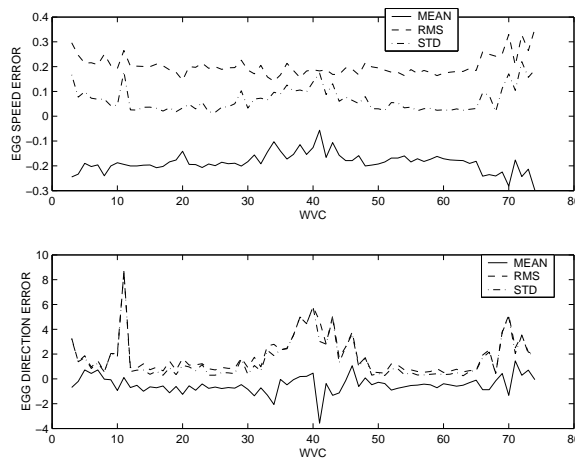


Figure A.5: Wind estimate error averaged over row 311 through 321 for all wind vector cells. The wind estimates were calculated using α' , β' , and γ' from L1B data with K_{pr} read in from table.

Unmodified Variance Coefficients With K_{pr}

Here α , β , and γ are used exactly as they are defined in equations (1), (2), and (3). Again K_{pr} is read in from table. K_{pm} is assumed to be 0.7 dB.

Table A.5: Wind Speed, Direction and MLE for rev 12950 row 314 wvc 18. Wind estimates calculated using L1B data to calculate α , β , and γ . K_{pr} is read in from a table.

L1B			L2B		
Speed	Direction	MLE	Speed	Direction	MLE
7.05	305.28	-0.1282366	7.23	306.04	-0.1160
7.26	286.39	-0.2950071	7.48	285.71	-0.2840
6.30	158.09	-0.8885471	6.39	156.45	-0.7680
6.31	99.81	-1.370577	6.45	99.65	-1.4200

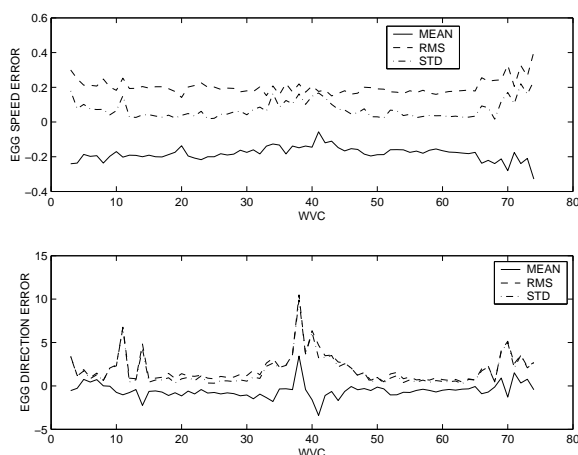


Figure A.6: Wind estimate error averaged over row 311 through 321 for all wind vector cells. The wind estimates were calculated using α , β , and γ from L1B data with K_{pr} read in from table.

A.5.2 L2A data

Modified Variance Coefficients

This is essentially the same test done with the L1B data. This time we use the data exactly as it is found in the L2A product. It is believed that this is the method used by the L2B processor at JPL. Comparison of this test with the corresponding test done with L1B data reveals a small change in the wind estimate ambiguities that is due to rounding. This small error due to rounding is not large enough to conclude that it is round off error that is not allowing us to achieve JPL L2B winds exactly.

Table A.6: Wind Speed, Direction and MLE for rev 12950 row 314 wvc 18. Wind estimates calculated using α' , β' , and γ' directly, extracted from the L2A file

L2A			L2B		
Speed	Direction	MLE	Speed	Direction	MLE
7.04	305.38	-1.374448	7.23	306.04	-0.1160
7.27	286.25	-3.067383	7.48	285.71	-0.2840
6.25	156.51	-9.251821	6.39	156.45	-0.7680
6.29	100.03	-14.85453	6.45	99.65	-1.4200

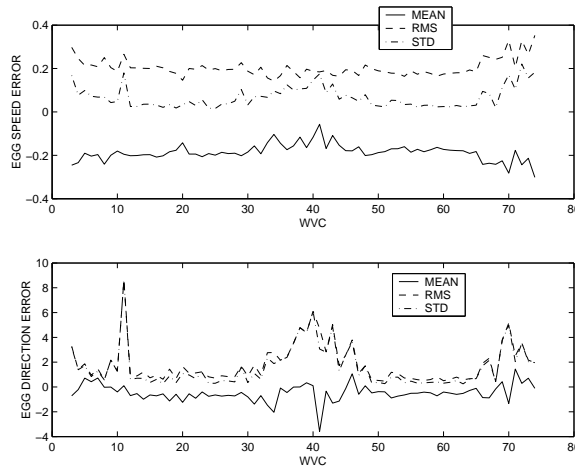


Figure A.7: Wind estimate error averaged over row 311 through 321 for all wind vector cells. The wind estimates were calculated using α' , β' , and γ' from the L2A file

Unmodified Variance Coefficients

The Variance Coefficients α' , β' , and γ' , which are extracted from the L2A file, are modified by applying,

$$\alpha = \alpha' \cdot (1 + K_{pm}^2) - 1 \quad (\text{A.8})$$

where again K_{pm} is assumed to be 0.7 dB, to get α . β , and γ are unchanged from β' and γ' (see equations (5) and (6)).

Table A.7: Wind Speed, Direction and MLE for rev 12950 row 314 wvc 18. Wind estimates calculated using α , β , and γ

L2A			L2B		
Speed	Direction	MLE	Speed	Direction	MLE
7.05	305.28	-0.1315774	7.23	306.04	-0.1160
7.26	286.39	-0.3026453	7.48	285.71	-0.2840
6.28	158.09	-0.9109951	6.39	156.45	-0.7680
6.28	99.80	-1.405940	6.45	99.65	-1.4200

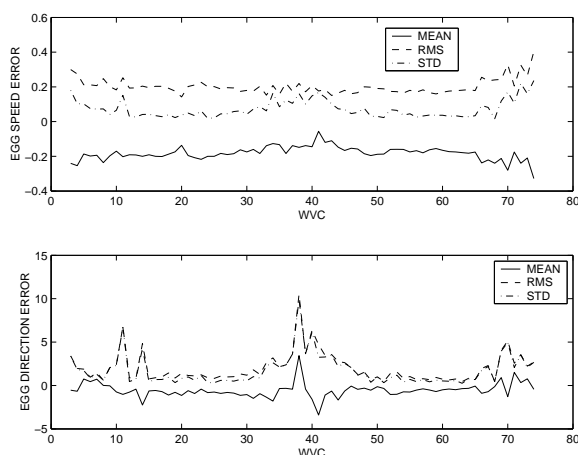


Figure A.8: Wind estimate error averaged over row 311 through 321 for all wind vector cells. The wind estimates were calculated using α , β , and γ calculated using equations (4), (5), and (6) with data from the L2A file

Modified Variance Coefficients With K_{pr}

α' , β' , and γ' are already computed in the L2A file but due to the fact that we were only able to accurately calculate these variables using equations (4), (5), and (6) when we set K_{pr} to zero raises some suspicion of whether or not JPL included K_{pr} in their calculation of α' , β' , and γ' . To test this K_{pr} was included by using,

$$\alpha'_{new} = \alpha'_{L2A} \cdot (1 + K_{pr}^2) \tag{A.9}$$

$$\beta'_{new} = \beta'_{L2A} \cdot (1 + K_{pr}^2) \tag{A.10}$$

$$\gamma'_{new} = \gamma'_{L2A} \cdot (1 + K_{pr}^2) \tag{A.11}$$

Table A.8: Wind Speed, Direction and MLE for rev 12950 row 314 wvc 18. Wind estimates calculated using α' , β' , and γ' as in equations (9), (10), and (11). K_{pr} is read in from a table.

L2A			L2B		
Speed	Direction	MLE	Speed	Direction	MLE
7.04	305.37	-1.227789	7.23	306.04	-0.1160
7.27	286.26	-2.749819	7.48	285.71	-0.2840
6.26	156.69	-8.306751	6.39	156.45	-0.7680
6.28	100.0	-13.25653	6.45	99.65	-1.4200

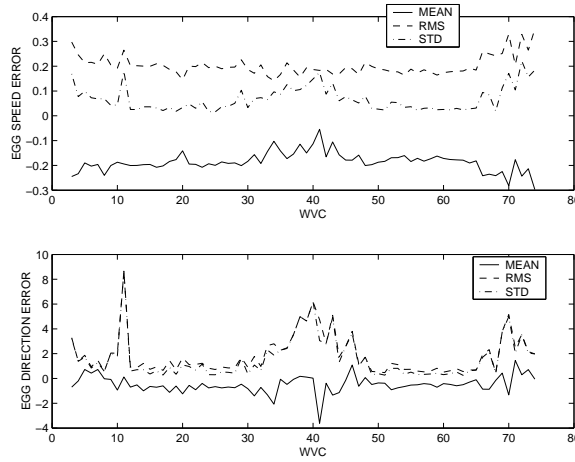


Figure A.9: Wind estimate error averaged over row 311 through 321 for all wind vector cells. The wind estimates were calculated using α' , β' , and γ' from the L2A file. K_{pr} is read in from table and included as in equations (9), (10), and (11).

Unmodified Variance Coefficients With K_{pr}

Again for this test K_{pr} is included in the variance coefficients using equations (9), (10), and (11). Again we see that the inclusion of K_{pr} has a very minimal effect on the wind retrieval.

Table A.9: Wind Speed, Direction and MLE for rev 12950 row 314 wvc 18. Wind estimates calculated using α , β , and γ which were calculated by first applying equations (9), (10), and (11) and then equations (8), (5), and (6). K_{pr} is read in from a table.

L2A			L2B		
Speed	Direction	MLE	Speed	Direction	MLE
7.05	305.28	-0.1281212	7.23	306.04	-0.1160
7.26	286.39	-0.2947268	7.48	285.71	-0.2840
6.28	158.09	-0.8871416	6.39	156.45	-0.7680
6.28	99.8	-1.368972	6.45	99.65	-1.4200

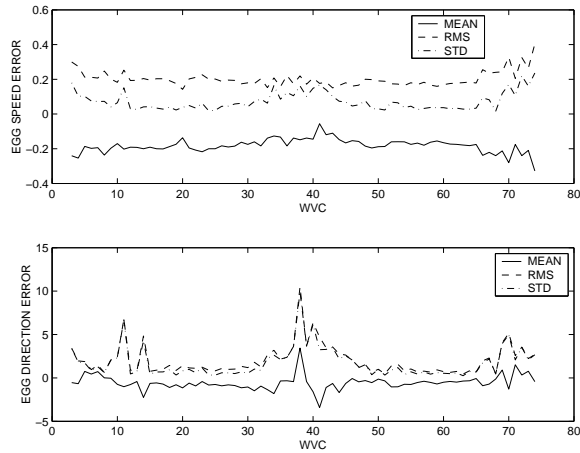


Figure A.10: Wind estimate error averaged over row 311 through 321 for all wind vector cells. The wind estimates were calculated using α , β , and γ calculated using equations (4), (5), and (6) with data from the L2A file. K_{pr} is read in from table and included as in equations (9), (10), and (11).

A.6 Conclusion

Table A.10 has listed the mean error using each method described above. The mean error was calculated from 10 rows of 72 WVCs worth of data. For each WVC the ambiguity that was closest to the chosen ambiguity in the L2B file was selected and the error in the speed and direction was taken. These errors were averaged over all WVCs and reported in Table A.10.

Table A.10: Mean error

	L1B			L2A		
Method	Speed Error	Direction Error	MLE Error	Speed Error	Direction Error	MLE Error
1	-0.1869	-0.4374	-4.3394	-0.1861	-0.4683	-4.3157
2	-0.1823	-0.5510	0.0442	-0.1826	-0.5564	0.0423
3	-0.1857	-0.4710	-3.8352	-0.1854	-0.4820	-3.8160
4	-0.1823	-0.5513	0.0544	-0.1826	-0.5567	0.0549

Appendix B

σ_0 Over Land

B.1 Introduction

There has been some concern about potential differences between QSCAT eggs and slices. Most studies have looked at this difference over the ocean. In this study the difference is examined over land, namely Northern Africa. Several homogeneous areas with a variety of mean σ_0 values have been chosen. These areas range from sections of the tropical rain forests of the Congo basin, where the backscatter is high, to the Sahara Desert, where the measured backscatter is low. Eight regions have been selected for this study as shown in Fig. B.1. The regions are numbered based on the level of the mean σ_0 value of the area. The numbers are assigned in descending order of mean σ_0 . The data for this study is obtained from the QSCAT L1B data product for revs 2927-2978 (days 011-014 of 2000).

B.2 Combining Slices, (Compositing)

The L1B data product contains data for each pulse of the Seawinds instrument. For every pulse the data for the “egg” and best 8 of 12 “slice” measurements listed. The slice measurements are produced by signal processing techniques which increase the range resolution of the pulse. To make a comparison between each egg and the corresponding slices for each pulse, we average or composite the slices together. Because we only have access to the best 8 of 12 slices it is not possible to obtain the exact egg σ_0 through compositing. However, we are interested in comparing eggs and composite slice values. Two methods have been considered. First, a linear average.

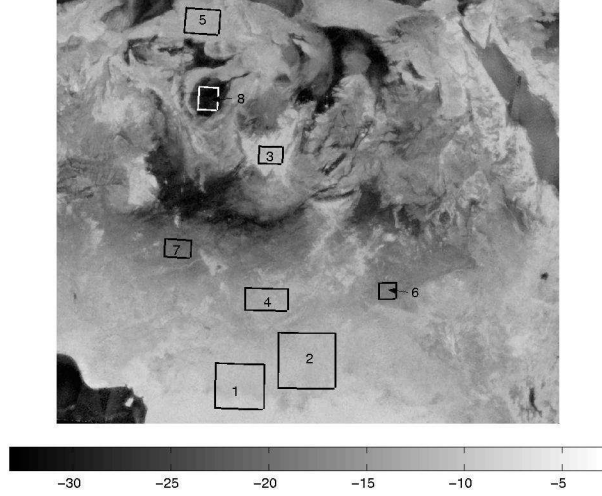


Figure B.1: Study region locations mapped over QSCAT image qusv-a-NAf00-037-040.sir. Each region is defined by latitude and longitude coordinates.

Second, a weighted average using the X_{factor} as the weight. To compute both of these averages the σ_0 value reported in the L1B file must be converted to linear space using

$$P_i = 10^{\left(\frac{\sigma_{0i}}{10}\right)}. \quad (\text{B.1})$$

The linear average composite slice is then computed using the sample mean

$$P = \frac{1}{N} \sum_{n=1}^N P_i \quad (\text{B.2})$$

where P_i is the σ_0 (linear space) and $N = 8$. For the weighted average the X_{factor} variables, which is extracted from the L1B data product, are converted to linear space.

The weighted average for each pulse is then computed using,

$$P = \frac{\sum_{n=1}^N P_i \cdot X_i}{\sum_{n=1}^N X_i} \quad (\text{B.3})$$

where P_i is σ_0 in linear space and $N = 8$. In Table B.1 these methods of compositing are illustrated using one pulse of the Seawinds instrument. The value of the X_{factor} listed in the table is in dB. When the X_{factor} is used in the weighted average it is converted to linear space.

σ_0 measurement	σ_0 (dB)	linear space	predicted Kp	X_{factor}
<i>Egg</i>	-9.55	0.1109	0.104	
slice 1	-10.14	0.0968	0.316	57.24
slice 2	-9.90	0.1023	0.314	58.66
slice 3	-9.76	0.1057	0.313	59.71
slice 4	-10.59	0.0873	0.313	60.40
slice 5	-9.06	0.1242	0.312	60.71
slice 6	-9.14	0.1219	0.312	60.64
slice 7	-9.08	0.1236	0.313	60.17
slice 8	-9.37	0.1156	0.313	59.24
Linear Ave.	-9.598	0.1097	0.3133	
Weighted Ave.	-9.5468	0.1110	0.3130	

Table B.1: Particular measured values for one random pulse

B.3 Regional Statistics

The regions in Fig. B.1 are defined by their lower left and upper right longitude and latitude coordinates. The size of each regions was chosen to get as closes to a homogeneous σ_0 value as possible. Several different regions were selected to give a variety of mean σ_0 values. As should be expected the larger regions contain more pulses of data, see Fig. B.2. The difference in the number of inner beam and outer beam pulses that fall in each regions is not surprising. This is caused by the geometry of QSCAT's swath. When the foot print of the far swath passes through a region only one or the other beam may fall in the region.

The regions are arranged in descending mean σ_0 values, see Fig. B.3. For example regions 1 and 2 is located near the tropical forests of the Congo River basin where the backscatter is high. Regions 7 and 8 are located in the desert regions where the backscatter is relatively low.

B.4 Comparing Eggs and Slices

Two methods are used to compare the egg σ_0 value and composite slice σ_0 value. The first method is to look at the difference in the mean σ_0 value for eggs compared to both the mean value of the weighted average composite and linear average

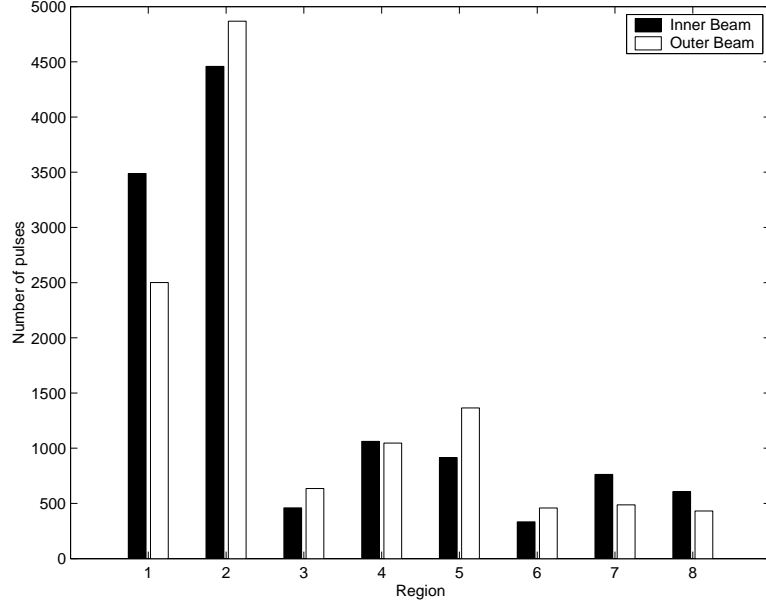


Figure B.2: Number of pulses that hit each region. Left bar is inner beam, right bar is outer beam

composite computed in linear space. The second is to look at the difference in dB. The first method simply computes the difference,

$$Error = \sigma_{0egg} - \sigma_{0slice} \quad (B.4)$$

where σ_0 is in linear space for both egg and slice. The second method is similar to the first method except σ_0 is converted to dB. This can also be done by,

$$Error_{db} = 10 \cdot \log_{10} \left(\frac{\sigma_{0egg}}{\sigma_{0slice}} \right) \quad (B.5)$$

where σ_0 is in linear space for both egg and slice.

Fig. B.4 illustrates these two methods.

B.5 Kp Prediction

Kp is defined as the normalized standard deviation of the echo return energy given by,

$$Kp = \frac{\sqrt{Variance[P_s]}}{Mean[P_s]} \quad (B.6)$$

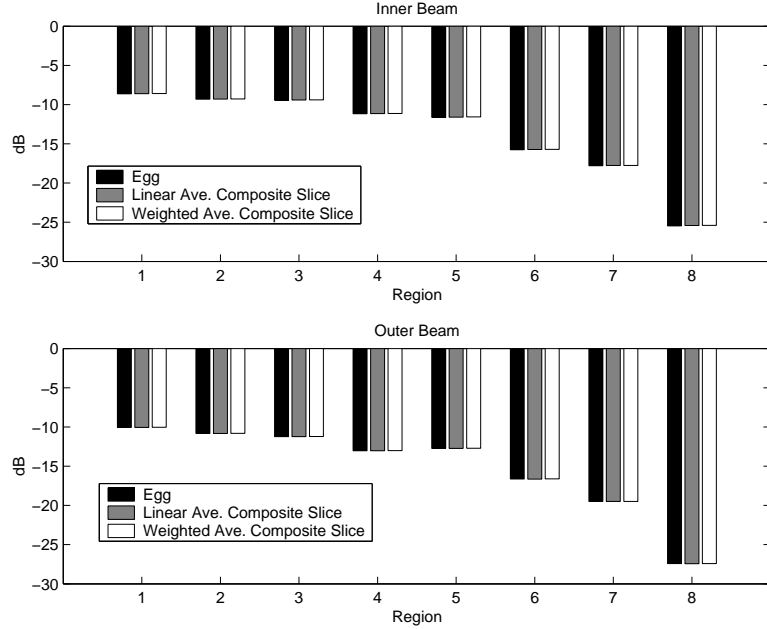


Figure B.3: Mean σ_0 value in each region

where P_s is the echo return energy. The predicted value of this parameter can be calculated using data contained in the L1B file, namely the instrument signal processing parameters: kpc_A , kpc_B , and kpc_C and the signal to noise ratio.

$$Kp^2 = kpc_A + \frac{kpc_B}{SNR} + \frac{kpc_C}{SNR^2} \quad (\text{B.7})$$

These instrument signal processing parameters are also known as the K_{pc} coefficients.

B.6 Empirical Kp calculation

The empirical Kp is calculated for each region after the mean and standard deviation of σ_0 in each region is found using

$$Kp_{egg} = \frac{(\sigma_{egg})}{\mu_{egg}} \quad (\text{B.8})$$

$$Kp_{slice} = \frac{(\sigma_{slice})}{\mu_{slice}} \quad (\text{B.9})$$

where σ_{egg} is the standard deviation and μ_{egg} is the mean of the measured egg σ_0 for each region. In the above equations we use σ_0 in place of the returned echo power P_r .

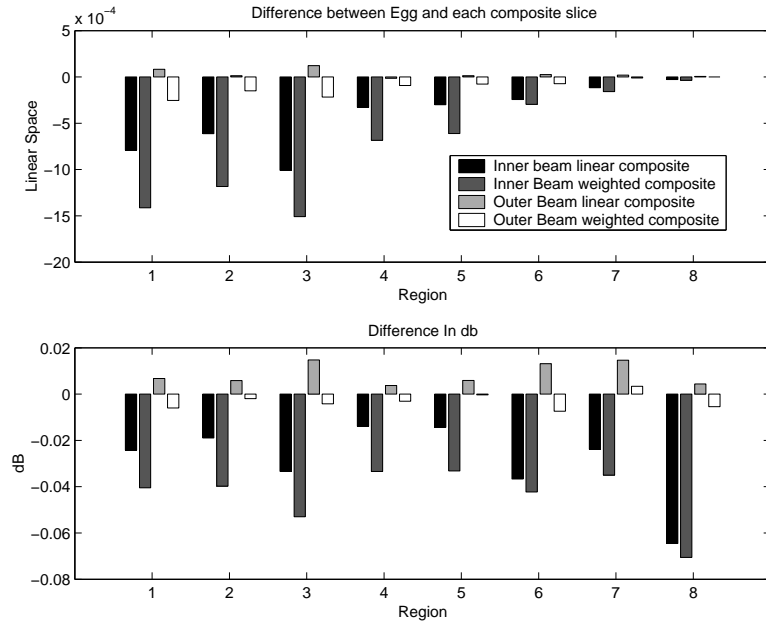


Figure B.4: Difference in mean σ_0 between linear averaged and weighted average composite slices. Top graph is difference in linear space. Bottom is difference in dB

This is legitimate because σ_0 is related to the echo power through the radar equation which can be simplified to

$$\sigma_0 = \frac{P_r}{X} \quad (\text{B.10})$$

where X includes the wave length, gains, etc in the radar equation. If X is assumed to be constant then it can be factored out of the numerator and denominator of the empirical K_p equations and canceled out. Fig B.6 compares predicted to empirical K_p values.

B.7 Conclusion

The method of compositing σ_0 can affect the accuracy of the compositing. Fig B.4 shows that for the inner beam the linear average gives better results but for the outer beam the weighted average performs better. Comparing the empirical K_p to the predicted K_p reveals that for eggs K_p is over-predicted while for composite slices this value is under-predicted.

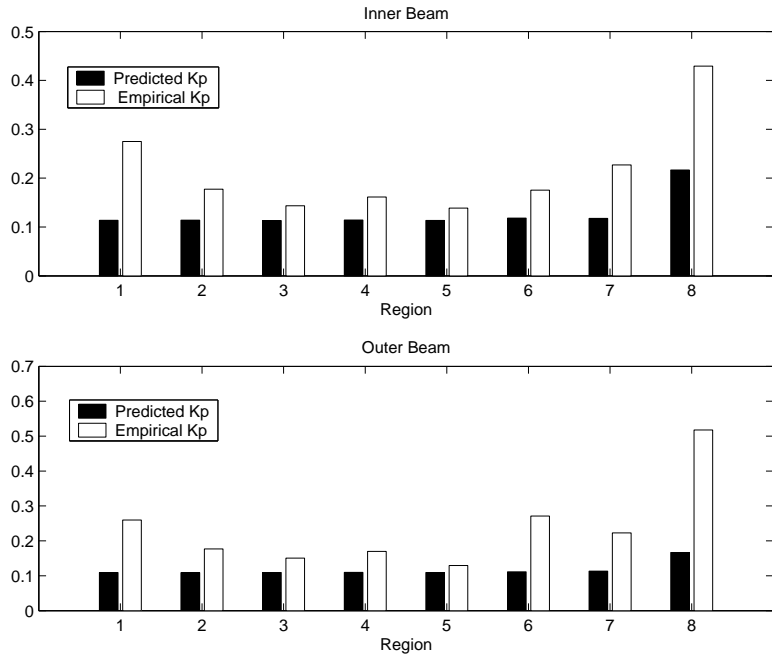


Figure B.5: Mean Kp value for eggs

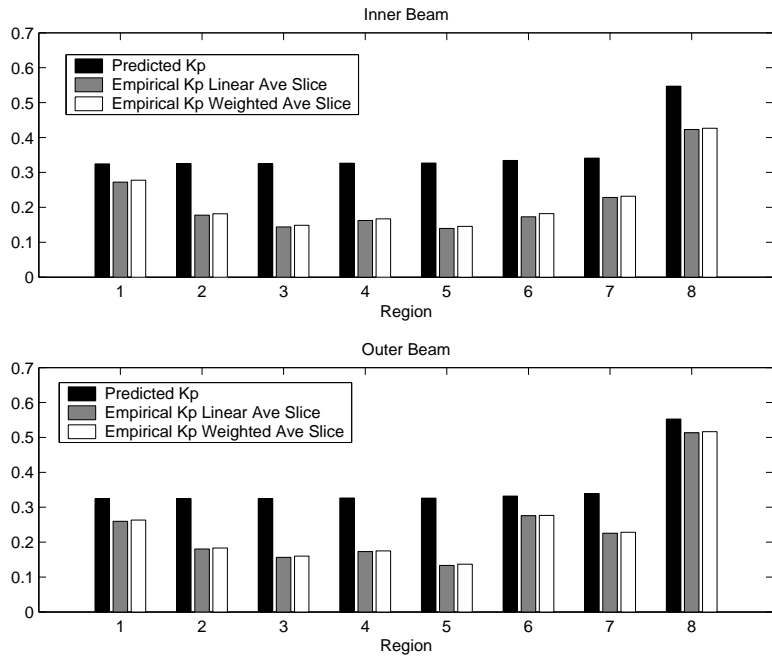


Figure B.6: Mean Kp for slices

Bibliography

- [1] W. T. Liu, “Progress in Scatterometer Application”, *Journal of Oceanography*, vol. 58, pp. 121–136, 2002.
- [2] F. Naderi, M. H. Freilich, and D. G. Long, “Spaceborne Radar Measurement of Wind Velocity Over The Ocean – An Overview of the NSCAT Scatterometer System”, *Proceedings of the IEEE*, vol. 79, pp. 850–866, June 1991.
- [3] F. T. Ulaby, *Microwave Remote Sensing Active and Passive*, vol. 2, Artech House, 1986.
- [4] F. J. Wentz, S. Peteherych, and L. A. Thomas, “A model function for ocean radar cross sections at 14.6 GHz”, *Journal of Geophysical Research*, vol. 89, pp. 3689–3704, 1984.
- [5] F. J. Wentz, L. A. Mattox, and S. Peteherych, “New Algorithms for microwave measurements of ocean winds: Applications to SEASAT and the Special Sensor microwave imager”, *Journal of Geophysical Research*, vol. 91, pp. 2289–2307, 1986.
- [6] D. S. Early and D. G. Long, “Image Reconstruction and Enhanced Resolution Imaging from Irregular Samples”, *IEEE Transactions on Geoscience and Remote Sensing*, vol. 39, no. 2, pp. 291–302, 2001.
- [7] D. G. Long, “High Resolution Wind Retrieval from SeaWinds”, *International Geoscience and Remote Sensing Symposium*, vol. 2, pp. 751–753, June 2002.
- [8] D. G. Long, P. Hardin, and P. T. Whiting, “Resolution Enhancement of Spaceborne Scatterometer Data”, *IEEE Transactions on Geoscience and Remote Sensing*, vol. 32, no. 3, pp. 700–715, 1993.

- [9] M. Spencer, S. Lou, and Y. Liu, “Algorithm Update: Kpc and Egg Formation”, *JPL internal Memo*, July 1998.
- [10] T. E. Oliphant and D. G. Long, “Accuracy of Scatterometer-Derived Winds using the Cramer-Rao Bound”, *IEEE Transactions on Geoscience and Remote Sensing*, vol. 37, no. 6, November 1999.
- [11] T. Lungu, Ed., *QuickSCAT Science Data Product User’s Manual*, Jet Propulsion Laboratory, Pasadena, CA, 2001.
- [12] A. S. Fletcher, “An Impementaion of Field-Wise Wind Retrieval for Seawinds on QuikSCAT”, Master’s thesis, Brigham Young Univerisity, 2001.
- [13] A. K. Jain, *Fundamentals of digital image processing*, Prentice-Hall, Inc, 1989.
- [14] D. G. Long, “High Resolution Wind Retrieval from SeaWinds”, *International Geoscience and Remote Sensing Symposium*, pp. 2187–2189, July 2001.
- [15] A. Zhang, “Estimate Coefficients of Sigma0 Variance”, *JPL internal Memo*, May 1999.